UNIVERSITAT DE BARCELONA

The Microtubule Nucleator γTuRC: Reconstitution and Analysis of its Assembly Mechanism

Fabian Zimmermann

UNIVERSITAT DE BARCELONA

FACULTAT DE FARMÀCIA I CIÈNCIES DE L'ALIMENTACIÓ

Programa de Doctorat en Biomedicina

The Microtubule Nucleator γTuRC: Reconstitution and Analysis of its Assembly Mechanism

Memòria presentada per Fabian Zimmermann per optar al títol de doctor per la Universitat de Barcelona

Jens Lüders	Fabian Zimmermann	Albert Tauler Girona
(Director)	(Doctorando)	(Tutor)

Fabian Zimmermann, 2021

Acknowledgment

First and foremost, I am deeply grateful to my supervisor Jens Lüders. Thank you for your continuous support throughout my PhD. Providing me with a scientific environment where I could develop my work in a curiosity-driven, explorative way, while raising awareness to not lose track of the bigger picture, and at the same time encouraging me in moments of setbacks, has been an immense privilege and an invaluable experience. Thank you for your genuine patience, criticism, generosity, as well as for helping me maintain a good command of German.

I would like to thank Thomas Surrey, Andreas Merdes, Eva Estébanez-Perpiñá, Cristina Mayor-Ruiz, and Sebastian Pons, for accepting to read and evaluate my work.

I thank the members of my thesis advisory committee, Joan Roig, Isabelle Vernos, and Xavier Salvatella, for making our meetings a place of constructive criticism, valuable advice, and encouragement.

I am grateful to our collaborators, Oscar Llorca and Marina Serna, for joining the journey to discover the molecular details of γTuRC & Co. Thank you for your hard work, resilience, and insatiable curiosity. I thank Artur Ezquerra for his previous work on MZT2, and Rafael Fernandez-Leiro for helping during cryo-EM analysis. I thank Joan Roig and Núria Gallisa for the opportunity to do collaborative work on BICD2. I thank Eva Estébanez-Perpiñá and Alba Jimenez for their collaborative work and x-ray crystallography efforts. Special thanks to Mireia Pesarrodona for helping me out with reagents and AKTA purifiers ever so often. Thank you Sara Muriel, for supervising me during the lab rotation.

I thank Carsten Janke and Jijumon A.S. for having me over in Paris to learn how to purify HeLa tubulin. I thank Antonina Roll-Mecak and the members of the Roll-Mecak lab for having me over in Bethesda, allowing me to get TIRF microscopy insights, despite the organizational challenges during the pandemic. It was a real pleasure and an invaluable experience.

I thank the ‘la Caixa’ foundation and the MSCA actions for supporting me with a PhD fellowship and extending their support due to the pandemic. I deem it a huge privilege having been provided so many opportunities through the fellowship.

A big thank you to the present and past members of the microtubule organization group for creating a nice lab atmosphere, getting through the pandemic as a caring team, and the good times outside of the lab, of which the most amazing calçotadas will always be remembered. Thank you Nina, for your genuine interest and curiosity in science, for our numerous discussions and your valuable feedback. Thank you Joel, for letting me join your project and always knowing how to take it easy. Thank you Marta; the care and initiative you have constantly taken has, and continues to be, invaluable for the whole lab. Thank you Aamir, for contributing to an international atmosphere in the lab. Thank you Ricardo, for being open to absurd jokes as my office mate, and your shared passion for coffee and delicious food. Thank you Marcos and Chithran, for being part of the next lab generation. Thank you Ilaria, for your contagious pragmatism and hands-on spirit. Thank you Cristina, for experimental support during my project, introducing me to baculovirus work, and your patience with ordering all the extra materials I needed throughout the years.

I thank the scientific service facilities at IRB, especially the protein production and mass spectrometry core facilities, for helpful discussions, fruitful suggestions, and experimental support, which have enriched and continue to enrich my scientific work. Special thanks to Nick Berrow, who took time to discuss experimental issues and design when I, often without prior notice, decided to drop by. I would like to thank the IRB administration for their support throughout the years, especially in helping me navigate through bureaucracy.

Ultimately - to my family and my friends for being a source of inspiration and believing in me more than I tend to do. For your open arms, open minds, and your continuous love. Thank you.

Abstract

The microtubule nucleator γ-tubulin ring complex (γTuRC) is essential for the function of microtubule organizing centers such as the centrosome. Since its discovery over two decades ago, γTuRC has evaded *in vitro* reconstitution and thus detailed structure-function studies. In my doctoral thesis, I reveal a previously unknown role of the RUVBL1-RUVBL2 AAA-ATPase complex (RUVBL) in mediating assembly of γTuRC. Specifically, human tissue culture cells that lack RUVBL display altered γTuRC subunit composition and localization to the centrosome. In a heterologous co-expression system, RUVBL is sufficient to assemble γTuRC from a minimal set of core subunits. Importantly, RUVBL interacts with γTuRC subcomplexes but is not part of fully assembled γTuRC. Reconstituted, purified γTuRC has moderate nucleation activity and its cryo-EM structure at ~4.0 Å resolution, which we determine through collaborative work, resembles native γTuRC. Detailed analysis of this structure identifies features that determine the intricate, higher-order γTuRC architecture. Besides γTuRC, I report the first reconstitution of human γ-tubulin small complex (γTuSC), a γTuRC subcomplex. Taking advantage of the recombinant expression system, I perform mutational analysis to dissect the roles of MZT1 and MZT2 subunits and their interactions with the N-terminal extensions (NTEs) of GCP3 and GCP2, respectively. This reveals how MZT:NTE units affect the γTuSC core structure and RUVBL-mediated γTuRC assembly. Together, this work discovers RUVBL as an assembly factor that regulates γTuRC in cells and allows production of recombinant human γ-tubulin complexes, defines the minimal set of γTuRC core subunits, and provides the first tool to allow recombinant production of γTuRC for in-depth mechanistic studies of γTuRC assembly and γTuRC-mediated microtubule nucleation.

Resumen

El complejo nucleador de microtúbulos en anillo de γ-tubulina (γTuRC) es esencial para la función de los centros organizadores de microtúbulos, como el centrosoma. Desde su descubrimiento hace más de dos décadas, γTuRC ha evitado su reconstitución *in vitro* y, por tanto, los estudios detallados de estructura-función. En mi tesis doctoral, revelo un papel hasta ahora desconocido del complejo AAA-ATPasa RUVBL1-RUVBL2 (RUVBL) en la mediación del ensamblaje de γTuRC. En concreto, las células de cultivo de tejidos humanos que carecen de RUVBL muestran una composición alterada de la subunidades de γTuRC y su localización en el centrosoma. En un sistema de coexpresión heteróloga, RUVBL es suficiente para ensamblar γTuRC a partir de un conjunto mínimo de subunidades principales. Es importante destacar que RUVBL interactúa con los subcomplejos de γTuRC pero no forma parte del γTuRC completamente ensamblado. El γTuRC reconstituida y purificada tiene una actividad de nucleación moderada y su estructura crio-EM a una resolución de ~4,0 Å, que determinamos mediante un trabajo de colaboración, se asemeja a la γTuRC nativa. El análisis detallado de esta estructura identifica características que determinan la intrincada arquitectura de orden superior de γTuRC. Además de γTuRC, informo de la primera reconstitución del complejo pequeño de γ-tubulina (γTuSC) humano, un subcomplejo de γTuRC. Aprovechando el sistema de expresión recombinante, realizo un análisis mutacional para diseccionar las funciones de las subunidades MZT1 y MZT2 y sus interacciones con las extensiones N-terminales (NTEs) de GCP3 y GCP2, respectivamente. Esto revela cómo las unidades MZT:NTE afectan a la estructura del núcleo de γTuSC y al ensamblaje de γTuRC mediado por RUVBL. En conjunto, este trabajo descubre que RUVBL es un factor de ensamblaje que regula γTuRC en las células y permite la producción de complejos de γ-tubulina humano recombinante, define el conjunto mínimo de subunidades del núcleo de γTuRC y proporciona la primera herramienta que permite la producción recombinante de γTuRC para realizar estudios mecanísticos en profundidad del ensamblaje de γTuRC y la nucleación de microtúbulos mediada por γTuRC.

List of abbrevations

AAA ATPase	ATPase associated with diverse cellular activities
ADP	Adenosine 5‘-diphosphate
ARP	Actin-related protein
ATP	Adenosine 5‘-triphosphate
ATR	Ataxia telangiectasia and Rad3-related
BSA	Bovine serum albumin
CAMSAP	Calmodulin-regulated spectrin-associated protein
CCT	Chaperonin containing TCP1
CDK5RAP2	CDK5 regulatory subunit associated protein 2
chTOG	Colonic and hepatic tumor overexpressed gene protein
CKAP5	Cytoskeleton-associated protein 5
CL-MS	Cross-linking mass-spectrometry
CM1	Centrosomin motif 1
Cryo-EM	Cryogenic electron microscopy
DAPI	4′,6-diamidino-2-phenylindole
DMEM	Dulbecco’s modified eagle medium
DSBU	Disuccinimidyl dibutyric urea
E.coli	Escherischia Coli
EB	End-binding protein
EGFP	Enhanced green fluorescent protein
EM	Electron microscopy
EtBr	Ethidium bromide
GA	Glutaraldehyde
GCP	γ-Tubulin complex protein
GDP	Guanosine 5‘-diphosphate
GEC	Gene expression cassette
GRIP	γ-Tubulin ring protein
GDP	Guanosine 5‘-diphosphate
GTP	Guanosine 5‘-triphosphate
HAUS	Human augmin-like complex
HEK293	Human embryonic kidney 293 cell line
HeLa	Human cervical cancer cell line from Henrietta Lacks
HEPES	4-(2-hydroxyethyl)-1-piperazineethanesulfonic acid
HRP	Horseradish peroxidase
Hsp70	Heat shock protein 70
Hsp90	Heat shock protein 90
IgG	Immunoglobulin G
INO80	Inositol auxotroph 80
IP	Immunoprecipitation

LC	Liquid chromatography
LGALS3BP	Galectin-3-binding protein
MAP	Microtubule associated protein
mBFP	Monomeric blue fluorescent protein
MBP	Maltose binding protein
mRNA	Messenger RNA
MTOC	Microtubule organizing center
mTOR	Mechanistic target of rapamycin
MZT	Mitotic-spindle organizing protein
NEDD1	Neural precursor cell expressed developmentally downregulated protein 1
NIN	Ninein
NINL	Ninein-like protein
NMD	Nonsense-mediated mRNA decay
NMR	Nuclear magnetic resonance
PBS	Phosphate buffered saline
PBST	Phosphate buffered saline with Tween20
PCM	Pericentriolar material
PCNT	Pericentrin
PCR	Polymerase chain reaction
PDB	Protein data bank
PGC	Poly gene expression cassette
PIH1D1	PIH1-domain containing protein 1
PIKK	Phosphatidylinositol 3-kinase-related kinase
PIPES	Piperazine-N,N'-bis(2-ethanesulfonic acid)
POLR2E	RNA polymerase II subunit E
PVDF	Polyvinylidene difluoride
RMSD	Root mean square devation
RNAi	RNA interference
RNAPII	RNA polymerase II
RPAP3	RNAse polymerase II-associated protein 3
RUVBL1	RuvB-like protein 1
RUVBL2	RuvB-like protein 2
SD	Standard deviation
SDS-PAGE	Sodium dodecyl sulfate – polyacrylamide gel electrophoresis
snoRNP	Small nucleolar ribonuclear particle
snRNP	Small nuclear ribonuclear particle
SRCAP	SNF2-Related CBP Activator Protein
SWR1	SWI2/SNF2-Related 1
TCP1	T-complex protein 1
TEV	Tabacco Etch Virus

TRiC	T-complex protein ring complex
Tris	2-Amino-2-(hydroxymethyl)propan-1,3-diol
U2OS	Human osteosarcoma epithelial cell line
URI	Unconventional prefoldin RPB5 interactor 1
WDR92	WD-40 repeat domain 92
γ-TuNA	γ-Tubulin nucleation activator
γTuRC	γ-Tubulin ring complex
γTuSC	γ-Tubulin small complex

Table of Contents

List of Figures

List of tables

1. Introduction

1.1 Microtubules

Microtubules are dynamic, filamentous protein polymers found in eukaryotic cells. Together with actin, intermediate filaments, and septins, microtubules make up the major parts of the cytoskeleton. Microtubules are versatile structures with many roles in dividing and non-dividing cells (**Figure 1**). In dividing cells, microtubules are part of the mitotic spindle, the machinery that organizes and distributes the genetic information to daughter cells (1, 2). In non-dividing cells, microtubules are tracks for intracellular transport (3, 4), they influence cell shape (5–7), enable motility (8, 9), and intercellular signalling (10).

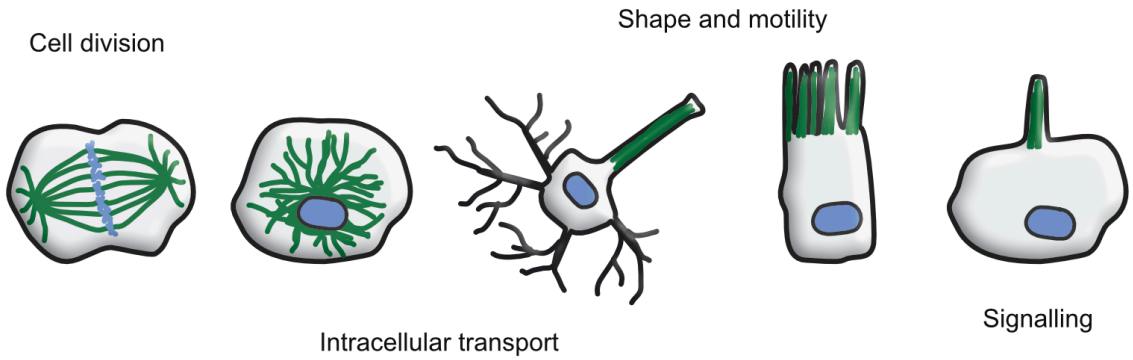

Figure 1: Microtubule-based structures. From left to right: In dividing cells, microtubules (green) form the mitotic spindle to distribute the replicated chromosomes (blue) to daughter cells. Non-dividing cells have a microtubule network for intracellular transport, which can contribute to cell shape as for example in neurons. Microtubules form motile cilia, as for example in multiciliated epithelial cells, and the primary cilium in numerous cells during vertebrate development.

Given their involvement in a variety of essential cellular processes, interfering with microtubule assembly or function can lead to various human diseases such as cancer (11), neurological (12, 13), and neurodevelopmental disorders (14–16). Microtubule-targeting agents are among the most successful chemotherapeutics to date, with new compounds being continuously discovered and approved for clinical use (17–19). Despite their widespread use, surprisingly little is understood how microtubule-targeting agents act at the organismal level and why they cure disease (19–21). While this leaves room for exciting discoveries, all microtubule-targeting agents alter the ability of microtubules to dynamically switch between growth and shrinkage. This phenomenon, called dynamic instability, is key for function of microtubules and also allows them to rapidly reorganize in response to a changing cellular environment.

1.2 Microtubule structure and dynamic instability

The building blocks of microtubules are heterodimers made of α-tubulin and β-tubulin (for simplicity hereafter referred to as tubulin). Tubulin is an obligate heterodimer and requires chaperone-mediated folding and assembly of its otherwise unstable α- and β-tubulin subunits (22, 23). The primary sequences of α-tubulin and β-tubulin have ~40% identity and their three-dimensional structures are largely identical (24). Stable tubulins can interact longitudinally in a "head to tail" fashion to form a protofilament, which in turn can interact laterally with other protofilaments to form hollow tubes. Commonly, 13 protofilaments are arranged with a slight helical offset, creating a microtubule with a diameter of ~25 nm (25, 26) (**Figure 2**). At one position the lateral contacts differ from the

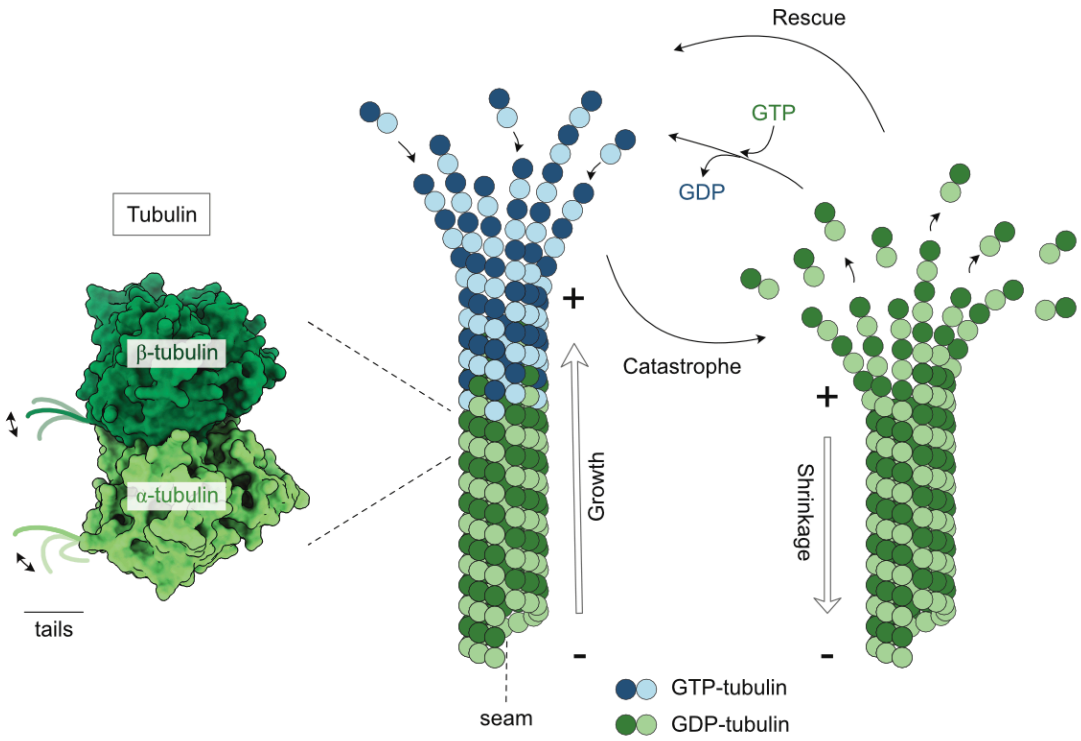

Figure 2: Structure and dynamic instability of microtubules. α/β-tubulin heterodimers ("tubulin") are building blocks of microtubules (PDB 1TUB). One GTP is bound to each α- and β-tubulin subunit (not shown) and both subunits have flexible C-terminal tails (not resolved in PDB 1TUB). Microtubule dynamic instability is the ability of tubulin to rapidly switch between polymerized and monomer state, a process that is driven by GTP-hydrolysis (Modified from Roll-Mecak, 2020).

rest of the lattice, creating a seam. Overall, this microtubule geometry is referred to as B-lattice. The "head to tail" arrangement of tubulins provides the microtubule with an intrinsic polarity. This polarity exposes β-tubulin on one end, called plus-end, and α-tubulin on the other end, called minus-end, with the lattice in between (27, 28). Notably, both

α- and β-tubulin have a GTP molecule bound. Following polymerization GTP in α-tubulin stays bound and is not exchanged, whereas GTP in β-tubulin can be hydrolysed to GDP (GDP-tubulin) and, after depolymerization, is exchanged for GTP (GTP-tubulin). GTP-tubulin binds preferentially at the plus-end. The plus-end therefore grows faster than the minus-end (29). Lattice-bound GTP-tubulin is stable and accumulates at the plus-end, forming a protective GTP-cap (30, 31). Lattice incorporation, however, causes GTP-tubulin to undergo a conformational change from "curved" in its free form to "straight" in its lattice-bound form (26, 32). GTP-Tubulin straightening causes activation of the β-tubulin GTPase activity and the formation of GDP-tubulin, which destabilizes the lattice (33). Due to the lag between GTP-tubulin incorporation and GTP-hydrolysis, constant renewal of the GTP-cap favors microtubule growth. Once GTP-tubulin incorporation stops, the GTP-cap disappears with a lag and exposes an unstable GDP-tubulin plus-end. Unstable plus-ends then depolymerize in a process often called "catastrophe". When GTP-tubulin incorporation outcompetes a catastrophe, the microtubule is "rescued". Whereas microtubule polymerization is dependent on tubulin concentration, depolymerization is not (34). Thus, key to dynamic instability is destabilization of the polymer lattice, which is encoded in the structure of tubulin and driven by the free energy released from GTP-hydrolysis (35, 36).

Dynamic instability can be fine-tuned in different ways, for example by the type of tubulins. Despite their high conservation across eukaryotes, many animals have several tubulin-encoding genes that differ slightly. Humans, for example, have eight α-tubulin and nine β-tubulin genes, resulting in a variety of tubulin isotypes, in part with tissue-specific expression profiles (37, 38). In addition, tubulins can undergo post-translational modification. These occur mainly on the flexible C-terminal tails of α- and β-tubulin. Thus, tubulin isotypes and post-translational modification results in a flurry of tubulin types that can alter dynamic instability (39–41).

In addition, microtubule dynamics are regulated by microtubule associated proteins (MAPs) (25, 42, 43). MAPs are non-tubulin proteins that interact with the microtubule through recognition of specific features of either the lattice, the plus- or the minus-end (44). For example, end-binding proteins (EBs) bind growing plus-ends and mediate recruitment of a variety of additional effectors, which provide the growing microtubule plus-end with specific properties. Microtubule polymerases such as XMAP215 family members

(chTOG/CKAP5 in humans) or depolymerases of the kinesin family can directly add or remove tubulin subunits from microtubule ends (45, 46). In addition, severing enzymes increase microtubule dynamicity by extracting individual tubulins from the lattice (47, 48). Other proteins such as TPX2 can bridge several tubulins and suppresses catastrophes (49–51). At the other end of the lattice, CAMSAP proteins can bind and stabilize minus-ends through a currently unknown mechanism (52, 53).

Organization of individual microtubules into arrays requires additional factors that bundle, crosslink or mediate sliding between neighboring microtubules. To perform their tasks, these factors can either use the free energy released by ATP-hydrolysis, or function independently of ATP hydrolysis. Microtubule motors couple ATP-hydrolysis to mechanical movement along microtubule lattices, allowing them to modulate the alignment and anchoring of microtubules within microtubule arrays. These motors are either kinesins, which mainly move towards plus-ends, or the minus-end directed dyneins (54, 55). Apart from motors, similar activities have been observed for other non-motor proteins (56–58). Besides organizing microtubule arrays, another central function of kinesins and dyneins is microtubule-based cargo transport.

In summary, many studies have focused on how tubulin types, MAPs and microtubule motors modulate growth and shrinkage, transport and positioning of existing microtubules, and how this organizes microtubules into arrays with different configurations. Before these factors can exert their function, however, a microtubule needs to be assembled first. In cells, a kinetic barrier inhibits spontaneous formation of new microtubules in the cytoplasm. To avoid formation at random sites, this kinetic barrier is lowered only when new microtubules are needed at specific locations. Formation of new microtubules, also known as microtubule nucleation, is controlled by nucleation factors found at the minus-end.

1.3 Microtubule nucleation occurs at microtubule organizing centers

Microtubule nucleation is spatially restricted to microtubule organizing centers (MTOCs) (59–61). A major MTOC in many animal cells is the centrosome. As for genome duplication, cells duplicate the centrosome once every cell cycle (62). Centrosomes consist of a pair of centrioles connected by a proteinaceous linker, which are associated with the

pericentriolar material (PCM). Centrioles are barrel-shaped structures composed of highly stable microtubules that are arranged in a 9-fold radial symmetry. Duplication of centrioles is initiated in S phase and requires polo-like kinase 4 (PLK4), which controls the ordered recruitment of various centriole-duplication factors to the wall of each 'mother' centriole to initiate formation of exactly one 'daughter' centriole (**Figure 3A**) (63, 64). The daughter centrioles grow in perpendicular orientation to the old 'mother' centrioles. In G2/M, the proteinaceous linker is disassembled, allowing separation of the two mother-daughter centriole pairs. Upon mitotic onset, the PCM expands, a process controlled by mitotic kinases such as PLK1 and known as centrosome maturation, and each centrosome associates with one of the two spindle poles (**Figure 3B**). This ensures inheritance of one

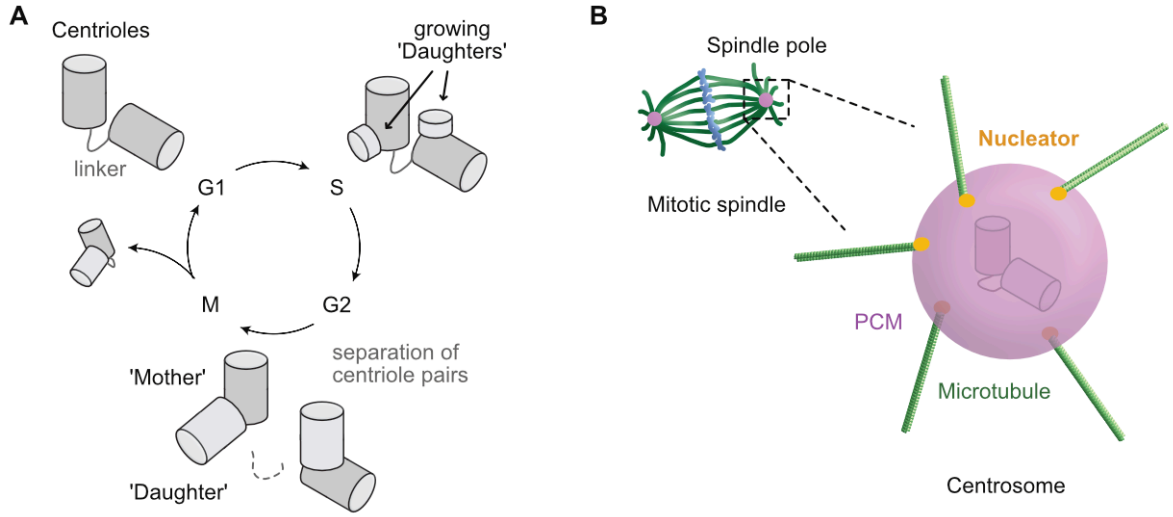

Figure 3: Centriole duplication cycle and centrosomal MTOCs. (A) Somatic cells contain a pair of cylinder-shaped structures in rectangular orientation, the centrioles (grey), that at their proximal base are connected by a proteinaceous linker. Centrioles are duplicated in S-phase when 'daughter' centrioles (light grey) emerge perpendicularly from old "mother" centrioles (dark grey). The daughters fully elongate and by G2 form a second daughter-mother centriole pair. The two pairs separate in G2/M after linker disassembly. (B) An expanded PCM (pink) is necessary to recruit sufficient microtubule nucleation factors (yellow) necessary for proper formation of the mitotic spindle.

centriole pair to each daughter cell. In somatic cells, the mother centriole is a crucial part of basal bodies essential to formation of cilia and flagella (16, 62, 65). While centrioles contribute to proper mitotic spindle formation, acentrosomal spindle poles can still form in the absence of centrioles (64, 66). The structure that accounts for the microtubule nucleation capacity of centrosomes is the PCM.

Despite numerous efforts, little is known about the molecular structure of the PCM. One of the few things that are clear, however, is that it consists of a limited number of scaffold proteins (among them PCNT and CDK5RAP2), which seem to be organized around centrioles in layered substructures (67–70). While the mechanism of PCM formation remains unknown, its growth after centriole duplication together with evidence of layered structures suggests that it may form by hierarchical assembly of PCM proteins. Proteins that account for the microtubule nucleation capacity ('nucleators') are recruited to the centrosome's outer layer. (**Figure 3B**). Despite the centrosome's dominant role as a microtubule organizer, non-centrosomal MTOCs can exist at the cytoplasmic surfaces of the Golgi apparatus, the nuclear envelope, at the mitochondrial outer membrane, the apical cell cortex, mitotic chromatin or at the lattice of pre-existing microtubules (71). Such non-centrosomal MTOCs may become dominant as part of differentiation programs during development, when centrosomal MTOC-activity is downregulated or switched off completely.

1.4 γ-Tubulin

A factor commonly present at all MTOCs, is a third tubulin: γ-tubulin. In contrast to α- and β-tubulin, γ-tubulin is not part of the microtubule lattice but specifically localizes to MTOCs where it is key for microtubule nucleation. γ-Tubulin was first discovered in the filamentous fungi *A. nidulans* as a component of the spindle pole body (a major MTOC in fungi), where it is required for microtubule nucleation and spindle formation (72, 73). Soon after, γ-tubulin was identified in other fungal and metazoan species with similar centrosomal localization and requirements for spindle assembly, but also for non-centrosomal MTOCs (74–81). As part of mitotic spindle formation, centrosomal γ-tubulin levels increase, which correlates with an overall increased microtubule nucleation capacity and an increased microtubule plus-end growth rate from centrosomes (76, 82, 83). Loss of γ-tubulin is lethal in fungi and various human cell lines (73–75, 84–87) and reduced levels produce severe defects in microtubule organization (88, 89). Similarly, injection of anti-γ-tubulin antibodies inhibits microtubule nucleation from MTOCs (77, 90).

Comparison of primary sequences between organisms shows that γ-tubulins are somewhat divergent (91). Whereas frog and human γ-tubulin share 98% identity, they are less similar to γ-tubulins in *A.nidulans* (~67% identity) (76) and even less to worm (~42% identity) or

budding yeast γ-tubulins (~35% identity) (75). It remains an open question whether this high divergence also leads to functional specialization of γ-tubulin. Consistent with this idea, budding yeast γ-tubulin cannot complement a fission yeast γ-tubulin null mutant (92), and neither human nor frog γ-tubulin can replace budding yeast γ-tubulin (89). Structurally, human γ-tubulin is more similar to β-tubulin than to α-tubulin (93). Two models were originally proposed to explain how γ-tubulin nucleates microtubules that differ mainly in the structural orientation that γ-tubulin may have during nucleation. First, nucleation may either occur by providing a short γ-tubulin-based protofilament (protofilament model) or, second, by mimicking the function of a layer of β-tubulins as part of a growing microtubule lattice, effectively creating a microtubule template (template model) (94).

1.5 The microtubule nucleator γTuRC

Structural control over γ-tubulin orientation is achieved through formation of dedicated protein complexes. In vertebrates and in the fruit fly *D. melanogaster,* γ-tubulin is assembled into γ-tubulin ring complexes (γTuRCs), the cell's main microtubule nucleators (97–102). γTuRCs are cone-shaped, ~2 mDa assemblies with an opening, giving them an overall lock washer shape with a helical pitch that reminds of the protofilament offset in a microtubule (103) (**Figure 4A**, compare to **Figure 2**). γTuRCs isolated from cell extracts and mixed with purified tubulin lower the critical concentration required for microtubule growth and cap minus ends of nucleated microtubules (98, 104, 105). In cells they were proposed to also regulate microtubule dynamics at the plus-end (106). Although the molecular details remain obscure, γTuRCs are thought to mediate microtubule nucleation by arranging γ-tubulin molecules in a way to create a tubulin recruitment platform. By direct binding of tubulin-heterodimers through γ-tubulin, γTuRC is thought to facilitate formation of a 'critical nucleus', leading to microtubule formation, a process that is otherwise unlikely to occur from free tubulin alone (**Figure 4B**). As mentioned above, historically two models of the mechanism of γTuRC-mediated nucleation have been proposed.

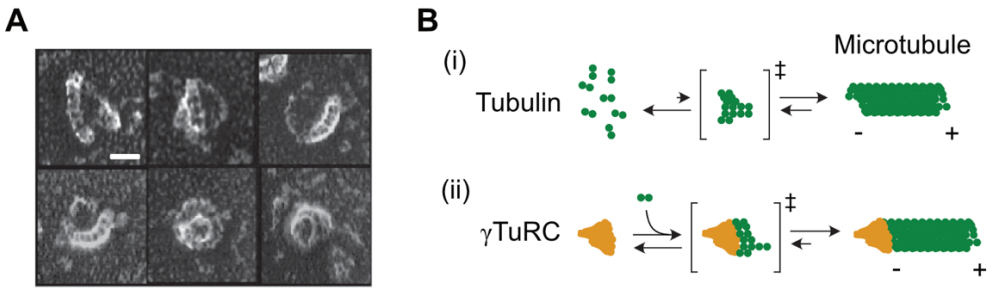

Figure 4: The microtubule nucleator γTuRC. (A) Electron microscopy image of purified *D. melanogaster* γTuRC (modified from Moritz *et al*., 2000). Scale bar 10 nm. (B) Microtubule nucleation from free tubulin (green) is unlikely under physiological conditions. (ii) γTuRC (brown) stimulates microtubule nucleation by providing a tubulin binding platform with microtubule symmetry (i). Potential transition states (‡) are in brackets.

In the protofilament model, a short γ-tubulin-based protofilament would bind α- and/or β-tubulin laterally and/or longitudinally in a manner that may involve dissolution of the γTuRC cone structure. In contrast, the template model would predict that during nucleation γTuRC overall retains its cone structure when γ-tubulin recruits tubulin-heterodimers through longitudinal interaction with α-tubulin (94, 107). Apart from γ-tubulin, formation of the higher-order γTuRC structure involves several other highly conserved proteins, the γ-tubulin complex proteins (GCPs, also known as TUBGCPs), that are key to understanding how the microtubule nucleator is built.

1.6 GCPs

GCPs form higher-order γ-tubulin-containing protein complexes and are essential for building a microtubule nucleator γTuRC. The GCP family of proteins comprises five members: GCP2, GCP3, GCP4, GCP5, and GCP6. In the following, I will use the nomenclature of human GCPs when referring to orthologues from other species but provide a guide to species-specific nomenclature of the most studied model organisms (**Table 1**). Vertebrates such as humans and frogs have GCP2, GCP3, GCP4, GCP5, and GCP6, which are also present in the fruit fly *D. melanogaster* and higher plants. Other metazoans such as the worm *C. elegans* only have GCP2 and GCP3. Similar to vertebrates, some fungal species such as the fission yeast *S .pombe* or the filamentous fungi *A. nidulans* also have GCP2, GCP3, GCP4, GCP5, and GCP6, but *Saccharomycetes* such as the budding yeast *S. cerevisiae* or the pathogenic yeast *C. albicans* only have GCP2 and GCP3, resembling the situation in *C. elegans*. Overall, organisms that have γ-tubulin always have GCP2 and GCP3, but some lack the GCP4/GCP5/GCP6 'set' of GCPs.

Table 1: GCP orthologues in metazoan and fungal organisms. (-) no orthologue identified.

H. sapiens	*X. leavis*	*A. thaliana*	*D. melanogaster*	*C. elegans*	*S. pombe*	*A. nidulans*	*C. albicans*	*S. cerevisiae*
GCP2	Xgrip110	AtGCP2	Grip84	Grip1/Gip1	Alp4	GCPB	Spc97	Spc97
GCP3	Xgrip109	AtGCP3	Grip91	Grip2/Gip2	Alp6	GCPC	Spc98	Spc98
GCP4	Xgrip75	AtGCP4	Grip75	-	Gfh1	GCPD	-	-
GCP5	Xgrip133	AtGCP5	Grip128	-	Mod21	GCPE	-	-
GCP6	Xgrip210	AtGCP6	Grip163	-	Alp16	GCPF	-	-

Similar to loss of γ-tubulin, loss of GCP2, GCP3, GCP4, GCP5, and GCP6 is lethal in human cells (84–86) and reduced levels impair γTuRC integrity and cause defects in interphase microtubule arrays and mitotic spindles in vertebrates and *D. melanogaster* (108–113). In fungi only the loss of GCP2 and GCP3 is lethal, and cells are viable without GCP4, GCP5, and GCP6. However, interphase microtubule nucleation is reduced, and spindle defects are observed (114–119). Besides causing γTuRC integrity defects, depletion of GCP2, GCP3, GCP4, GCP5, and GCP6 also leads to centriole duplication defects (113). The same defect is observed in cells with reduced γ-tubulin levels (120), raising the interesting possibility that γTuRC is also involved in formation of centriolar microtubules (121). Together, the set of GCP family members and cellular consequences of their disruptions are somewhat different across species, which may indicate species-specific differences in microtubule nucleation complexes.

1.7 Structure and assembly of γTuRCs

All GCPs are characterized by conserved N- and C-terminal γ-tubulin ring protein (GRIP) domains (N- and C-GRIP, respectively) (**Figure 5A**). GRIP domains share similarity on primary sequence level with a few conserved stretches (also known as GRIP motifs) but an overall low sequence identity (122). This prevented accurate prediction of domain boundaries between GRIP domains and the remaining GCPs regions based on sequence information alone. Except for GCP4, all GCPs contain an N-terminal extension (NTE) that

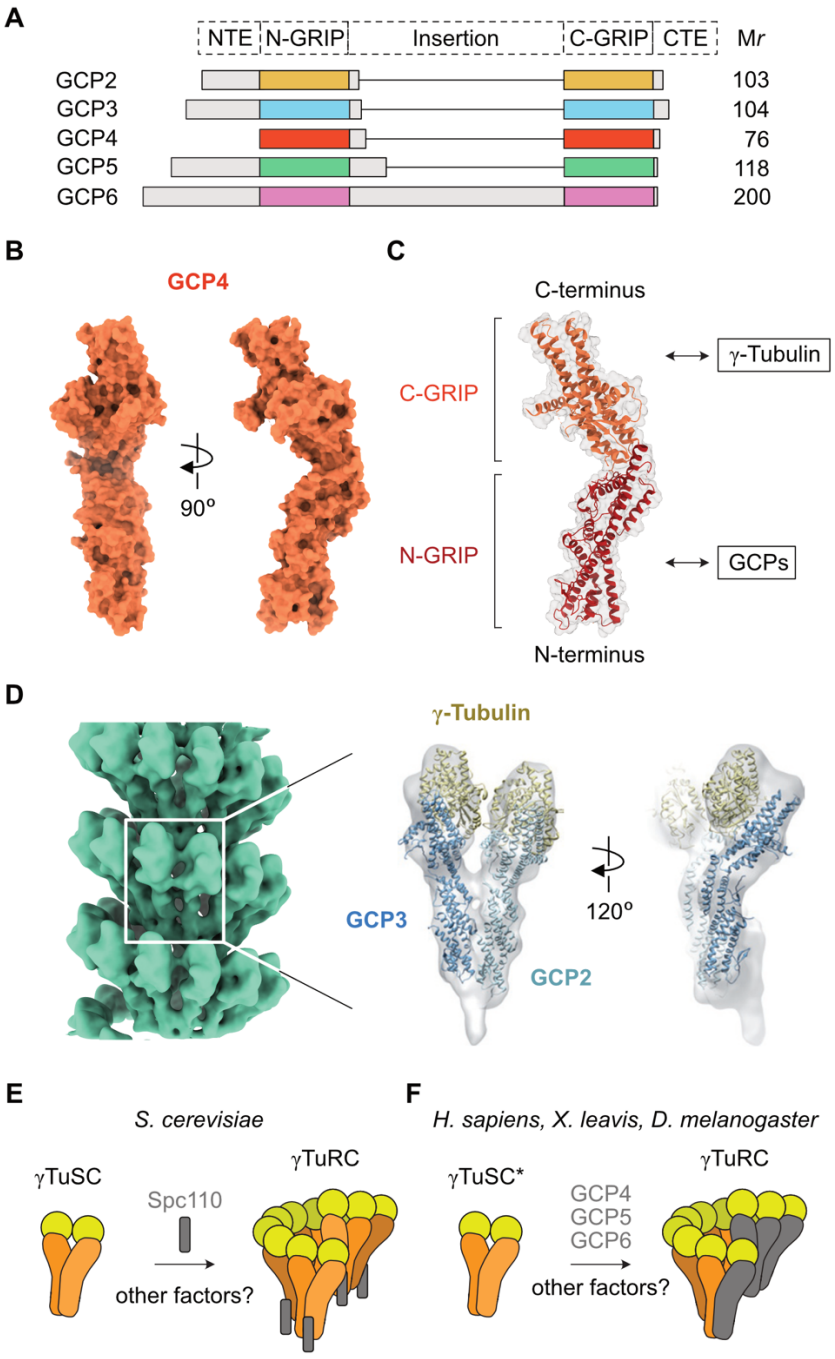

Figure 5: GCPs generate γ-tubulin surfaces for nucleation templates. (A) Bar representation of GCP2-6 domain architecture and relative molecular mass (M*r*) for the human proteins. N-GRIP, C-GRIP are highlighted in color. NTE, insertion, and CTE are indicated in grey. Black lines are spacers to illustrate the significantly smaller insertions of GCP2-5 compared to GCP6. (B) Structure of GCP4 (PDB 3RIP) shown as surface representation. (C) Ribbon diagram of GCP4 (PDB 3RIP) with its N-GRIP (dark red) and C-GRIP (orange) domains. (D) Helical filaments formed from oligomerized budding yeast γTuSCs (EMD 2799). Inset shows a pseudoatomic model of Y-shaped γTuSC with the subunits GCP3 (dark blue), GCP2 (light blue), and two γ-tubulins (light brown) (modified from Kollman *et al.*, 2011). Assembly and composition of γTuRCs in (E) *S.cerevisiae* occurs at MTOCs by direct oligomerization of γTuSCs by Spc110 (grey), whereas (F) other species assemble γTuRCs with GCP4, GCP5, and GCP6 (grey) in the cytoplasm. Other factors may participate in both modes of γTuRC assembly. Asterisk denotes that the exact subunit composition of vertebrate γTuSC is yet unknown.

precedes the N-GRIP domain and is about ~150-300 aa in length. The N-GRIP domain is followed by an insertion domain that is large in GCP6 (~800 aa) but substantially smaller, if not absent, in the rest of the GCPs. In addition, very short C-terminal extensions (CTEs) seem to exist adjacent to the C-GRIP domain.

Structural analysis of GCP4 has provided atomic insight into GCP architecture and defined the N- and C-GRIP domains to have a characteristic, mostly alpha-helical fold, forming an elongated, stalk-like structure with a kink (**Figure *5*B**) (123). Whereas the C-GRIP domain is a γ-tubulin binding domain, the N-GRIP domain can mediate lateral interactions between GCPs (**Figure *5*C**) (123). Structural key residues in the two GRIP domains are highly conserved between GCP2-6, arguing for strong structural and functional similarity of GCPs. Thus, by using their GRIP domains, GCPs can associate laterally and at the same time expose γ-tubulins on one end. Past work with budding yeast and fruit fly proteins has shown that GCP2 and GCP3 can each bind a copy of γ-tubulin to form a heterotetrameric γ-tubulin small complex (γTuSC) with a characteristic Y-shape (95, 114, 124, 125). In γTuSC, GCP2-and GCP3-bound γ-tubulins are bound to the C-GRIP domains in a manner that allows lateral interactions between γ-tubulins, and at the same time orientates free longitudinal tubulin interaction sites away from the Y-shaped stalk (**Figure *5*D**, right panel) (95). This structure generates γ-tubulin polarity that favors a template-based microtubule nucleation mechanism in which γ-tubulin could directly bind tubulin-heterodimers through the longitudinal interaction with the α-tubulin subunit.

In the presence of the spindle pole body component 110 (Spc110), budding yeast γTuSCs can oligomerize into helical filaments forming a γTuSC-spiral (**Figure *5*D**) (95, 96). These γTuSC-spirals resemble microtubule symmetry in cross-section and have some microtubule nucleation activity when incubated with purified tubulin. Thus, at least in budding yeast γ-tubulin is brought into a nucleation-competent state by direct recruitment and oligomerization of γTuSCs at the spindle pole body, the functional equivalent of the centrosome in animal cells. Notably, γTuSC-spirals do not have perfect microtubule symmetry as GCP3-bound γ-tubulins are displaced outwards. This template mismatch indicates that γTuSCs recruited to spindle pole bodies most likely require a conformational change for full nucleation activity. Indeed, γTuSCs engineered to adapt a ‘closed’ conformation that matches better the microtubule symmetry nucleates almost twice (~75% increase) the number of microtubules under otherwise equal conditions (96). Whether

γTuSC-spirals formed *in vitro* also exist *in vivo* remains unknown. If so, excessive oligomerization of γTuSC would have to be prevented. In fact, γTuSCs bound to a larger fragment of Spc110 does not form spirals (96), but the precise structure of this γTuSC oligomer has remained unexplored. Nevertheless, it can be hypothesized that budding yeast builds a γTuRC-like particle from seven γTuSCs that oligomerize into a lock washer-shaped cone with the first and last γ-tubulin overlapping. This configuration would be compatible with a template for the nucleation of a 13-protofilament microtubule (**Figure *5*E**).

In contrast to budding yeast, pre-assembled γTuRCs are found in the cytosol of vertebrates and flies. These γTuRCs contain GCP4, GCP5 and GCP6 and display only low microtubule nucleation *in vitro* (98, 102, 126). Individual depletion of GCP2-6 in cells causes γTuRC integrity defects on sucrose gradients and leads to reduced recruitment of γ-tubulin to centrosomes, suggesting that only fully assembled γTuRC localizes to centrosomes and GCP2-6 have a non-redundant function as part of γTuRC (113, 127, 128). As judged by dye-stained protein band intensities of purified native γTuRC, GCP4, GCP5 and GCP6 are of lower abundance compared to the γTuSC subunits GCP2 and GCP3. As γTuRC purification methods in these studies differed and dye-stained protein band intensities did not allow precise quantification, the γTuRC subunit stoichiometry remained vaguely defined. Estimates ranged from one to three GCP4 copies, one GCP5 copy, one to three GCP6 copies, 5-6 of each GCP2 and GCP3, and 10-14 γ-tubulins. Moreover, it was unclear whether the different GCPs occupy fixed positions in γTuRC or may display some interchangeability (**Figure *5*F**). Using FLIM-FRET techniques in human cells expressing fluorescently tagged GCPs, past work localized GCP4 directly adjacent to GCP5 in γTuRC (129), suggesting that certain positions may be fixed. As the spatial resolution of this technique is limited, structural und functional analysis of purified γTuRC is needed to define the positions and functions of specific GCPs in the ring. Such studies could also clarify the number of γ-tubulins in pre-assembled γTuRC. As the γ-tubulin number equals the number of potential binding sites for tubulin heterodimers, this aspect has direct implications for our understanding of the mechanism of γTuRC-mediated microtubule nucleation and its kinetics. While a γTuRC with 13 γ-tubulins should bind one α-tubulin per γ-tubulin upon activation of microtubule nucleation, formation of a 13 protofilament microtubule could also occur on a template that does not contain 13 γ-tubulins. This could

be achieved by two different modes. First, if γTuRC had more than 13 γ-tubulins, sterical hinderance by structural elements could block tubulin binding sites. An example for this is the hypothetical 'minimal' yeast γTuRC made of seven 7 γTuSCs. Here, the first and the last of the 14 γ-tubulins of the ring are superimposed at the seam when viewed from the top, effectively impeding the first γ-tubulin from tubulin binding. Second, if less than 13 γ-tubulins were present, 'gap filling' could complete a 13 protofilament microtubule. In this scenario closure of the microtubule would be driven by tubulin lateral interactions that incorporate into the gaps between γ-tubulin-bound tubulins at the nucleation surface.

Assembly of a complete γTuRC with all its core subunits is likely achieved sequentially, via sub-complexes. Indeed, density gradient analysis of cell extracts suggests that smaller γ-tubulin/GCP complexes exist (99, 102, 113), which may correspond to γTuSC or γ-tubulin/GCP4/5/6 complexes. In agreement with this, fission yeast seems to have γTuSC-like GCP4/GCP5 and GCP4/GCP6 complexes that can interact with γTuSC (116). Very recent work in human cells has shown that a sub-complex consisting of γ-tubulin/GCP4/GCP5/GCP6 with low levels of GCP2/GCP3 can be purified when γTuRC is treated with high salt buffers (130). While this γ-tubulin/GCP4/GCP5/GCP6-enriched disassembly product does not support microtubule nucleation, treatment with γTuSC-containing extracts rescues nucleation activity. While it remains elusive if complete γTuRCs were assembled in this assay, these experiments suggest that GCP4/GCP5/GCP6-containing γTuRC sub-complexes also exist in humans (130). Interestingly, domain swapping experiments have shown that the C-terminal halves of GCPs (comprising C-GRIP and CTE domains) can be interchanged without affecting γTuRC integrity. In contrast, interchanging the N-terminal halves (comprising NTE, N-GRIP and insertion domains) abolishes γTuRC assembly (129). Thus, while the γ-tubulin-binding activity is similar among all GCPs, the interactions mediated by the N-terminal half are specific to each GCP. Consequently, the GCP-GCP lateral interactions are likely mediated by unique features in their N-GRIP domains, the NTEs, and/or the insertion domains.

In summary, past studies have shown that complexes made of γ-tubulin and GCPs are basic ingredients of a microtubule nucleator. Key structural elements that build the γTuRC structure are the N- and C-GRIP domains of GCPs, which establish the polarity at the nucleation surface and mediate formation of the higher-order structure. Additional GCP domains are likely crucial for γTuRC assembly, but their roles remain poorly understood

and species-specific differences in the GCP protein family add further complexity. Apart from the core subunits discussed above, additional factors may be required to build γTuRC sub-complexes and assemble these into a complete γTuRC.

1.8 Additional γTuRC binding factors

Several additional factors readily copurify with γTuRC. In contrast to GCPs, these proteins lack GRIP domains, suggesting they have either different structural or regulatory roles.

1.8.1 MZT proteins

MZT1 and MZT2 (also known as MOZART proteins) are two relatively small proteins that interact with γTuRC in many organisms.

MZT1 is an ~8 kDa protein that is highly conserved across eukaryotes except in budding yeast (60, 131). First identified in plants as a GCP3 interacting protein (132), MZT1 also co-purifies with vertebrate γTuRC (122, 133, 134). Yeast-two-hybrid assays suggest that human MZT1 does not only bind to the NTE of GCP3, but also to the NTE of GCP5 and GCP6 (113, 135). This interaction requires a conserved MZT1-binding motif found in the GCP NTEs (113). By binding to GCP NTEs, MZT1 is thought to have regulatory function by modulating the targeting of γTuRC to MTOCs (113, 133, 135–139), which I explain in more detail below. Depletion of MZT1 by RNAi in human tissue culture cells causes severe spindle assembly and centriole duplication defects, effectively phenocopying γ-tubulin depletion (113, 133). Loss of fission yeast and *C.albicans* MZT1 is lethal (135, 137, 140), and *C.elegans* depleted of MZT1 show early embryonic lethality (139). Not all species, however, show such dramatic MZT1 phenotypes. Mutant MZT1 alleles in *D.melanogaster* result in γTuRC recruitment defects to only a subset of MTOCs and only cause mild defects in microtubule based structures (141). Despite its requirement for γTuRC targeting, there's conflicting evidence whether MZT1 plays a role in γTuRC assembly. Two studies depleted human cell lines of MZT1 using RNAi and analyzed γTuRC integrity by subjecting cell extracts to analytical gradient centrifugation. Whereas one study could observe loss of γTuRC in U2OS cells upon MZT1 depletion (135), another study did not observe this effect in HeLa cells (113). Thus, more work is needed to clarify a potential structural role for MZT1 in γTuRC.

Despite its small size, MZT1 has surprisingly complex biochemical properties. MZT1 preparations from *E.coli* have a strong tendency to homo-oligomerize into multimers, yielding polydisperse samples with equilibria between trimeric to dodecameric MZT1 states (136, 142). Somewhat similar properties have been attributed to *C.albicans* MZT1. When added to purified *C.albicans* γTuSC, MZT1 induces formation of high-molecular weight oligomers (135). The authors interpreted this observation to be due to an oligomerization activity of MZT1, that is needed to form a nucleation template. In EM micrographs, however, these high-molecular weight oligomers resemble aggregates more than ring-like structures (135). Fission yeast MZT1 has very recently been shown to prevent aggregation of purified fission yeast γTuSC *in vitro*, likely by direct binding to GCP3 (140). An interesting detail of this study is that the aggregation-prone fission yeast γTuSC carries a solubilizing MBP-tag used for purification. Thus, it remains a possibility that in the absence of MBP fission yeast γTuSC would be even more aggregation-prone under the conditions used. As a result, solubilization mediated by MZT1 may indeed be central for overall complex solubility. Thus, although some evidence obtained in fungi suggests a role for MZT1 in γTuSC oligomerization and γTuSC integrity, the molecular basis of this activity is incompletely understood.

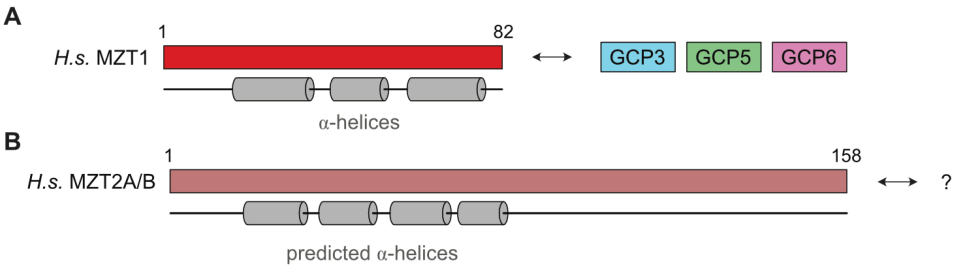

Figure 6: MZT proteins. (A) Domain organization of human MZT1 (red) with three α-helices (grey cylinders) and reported interacting GCPs (B) MZT2A/B are predicted to contain four α-helices but its cellular interactions remain poorly understood. Regions predicted to be unstructured in secondary structure predictions are shown as black line.

A recent study used NMR to show that human MZT1 contains three short helices, confirming previous secondary structure and *de novo* structure predictions of plant MZT1 (**Figure *6*A**) (131, 142). Despite providing insight into MZT1 secondary structure, the study failed to confirm the tertiary structure of the *de novo* model due to insufficient spectral quality. Thus, we lack crucial structural information on how MZT1 helices fold in three dimensions, a feature this is possibly key to understanding how MZT1 interacts with

itself and other binding partners. It should be noted that the authors added detergent to inhibit oligomerization of MZT1. This likely stabilized monomeric MZT1 and allowed structural analysis by NMR. Under these detergent conditions, MZT1 shows weak but direct interaction with purified GCP3-NTE. Notably, also purified GCP3-NTE contained a solubility-providing SUMO-tag, perhaps indicating instability of GCP3-NTE on its own (142). Upon interaction of both proteins, several MZT1 residues located in the α-helices show changes in their chemical environment upon GCP3-NTE addition, indicating that MZT1 undergoes structural changes when it forms a complex with GCP3-NTE. In summary, there is little doubt that MZT1 performs tasks that are crucial for the function of γTuSCs and γTuRCs in microtubule nucleation and organization. Likely, this involves direct interaction between MZT1 and the NTEs of GCPs, two polypeptides with complex biochemical properties when studied in isolation. More work is needed to understand the molecular details of these interactions, and how these may relate to γTuSC and γTuRC integrity and function.

MZT2A and MZT2B are two additional proteins that associate with human γTuRC (122, 126, 133, 134). MZT2A and MZT2B are ~16 kDa proteins encoded by distinct genes and almost identical (96% amino acid identity) (122). In fact, among the organisms where MZT2 has been identified humans are the only species that has two MZT2 genes. They are present on different chromosomes but share several flanking genes. Thus, they are likely the result of a duplication of a larger segment of chromosomal DNA. For simplicity, since the two proteins are essentially identical, I will refer to MZT2A and MZT2B as 'MZT2' if not stated otherwise. MZT2 also copurifies with *X. leavis* γTuRC (134) and is generally present in deuterostomes (comprising vertebrates, sea stars, and crinoids), in some insects such as the honeybee *A. mellifera*, but neither in *D. melanogaster* nor in *C. elegans* or fungi. Apart from its reported copurifications with γTuRC, only one study has presented an analysis of the cellular function of MZT2 to date (122). MZT2 binds to γTuRC and possibly γTuRC sub-complexes throughout the cell cycle and MZT2 depletion by RNAi does not seem to affect γTuRC integrity. Depletion of MZT2 reduces γTuRC recruitment and microtubule nucleation from interphase centrosomes but not from the mitotic spindle. Secondary structure predictions of MZT2 find four α-helices in its N-terminal half and an unstructured C-terminal half (**Figure *6*B**). Yeast two-hybrid analysis has shown that MZT2B interacts with the N-terminal half of GCP2, but this interaction has not been analysed yet in its native cellular environment (135). Thus, more work is needed to define

the molecular details of how MZT2 interacts with γTuRC to understand its function as an interphase-specific γTuRC regulator.

1.8.2 NME7 and LGALS3BP

NME7 and LGALS3BP are two additional proteins that have been found in various purifications of human γTuRC (122, 126, 133).

NME7 is a member of the NME kinase family thought to have developmental roles in metazoans (143). NME7 localizes to centrosomes in a γTuRC-dependent manner and its depletion does not alter centrosomal γ-tubulin levels, arguing for a regulatory rather than a structural role in γTuRC (144). Findings that NME7 can stimulate γTuRC-mediated microtubule nucleation (144) have recently been questioned (145). NME kinase family members can have dual activity as protein and nucleoside diphosphate kinase (143). Thus, a hint towards understanding the role of NME7 as γTuRC interactor would be to address what γTuRC component is phosphorylated by NME7, if at all.

LGALS3BP is known as a glycoprotein that is secreted into the extracellular matrix to regulate cell adhesion and immune system function, and is a potential tumor marker (146). More recently, LGALS3BP was found to localize near centrioles and basal bodies, where it appears to regulate centriole biogenesis and proper mitotic spindle formation (147). At the centrosome, LGALS3BP is found in a complex with various centrosomal proteins including CDK5RAP2, EB1, SMYLE (a short myomegalin isoform) and γTuRC, which has been proposed to regulate dynamics of newly formed microtubules at centrosomes or the leading edge of migrating cells (148). Depletion of LGALS3BP by RNAi does not alter γ-tubulin recruitment to the centrosome, which argues against it being a structural γTuRC component or required for γTuRC recruitment to MTOCs.

Summing up, MZT1 and MZT2, NME7 and LGALS3BP are commonly found γTuRC binding proteins whose roles remain incompletely understood. A comparison among species shows that NME7 and LGALS3BP have only been identified to bind to human γTuRC, MZT2 to human and frog γTuRC, and MZT1 to γ-tubulin complexes in all organisms studied but budding yeast (**Table 2**). Thus, while some of these factors may have a conserved evolutionary function, others may play specific roles in higher eukaryotes.

Alternatively, other yet to be identified factors could carry out their function in organisms lacking a clear orthologue.

Table 2: Orthologues of γTuRC binding proteins in metazoan and fungal model organisms. Confirmed orthologue (+) and no orthologue identified (-).

	H.sapiens	*X.leavis*	*A.thaliana*	*D.melanogaster*	*C.elegans*	*S.pombe*	*A.nidulans*	*C.albicans*	*S.cerevisiae*
MZT1	+	+	+	+	+	+	+	+	-
MZT2	+	+	-	-	-	-	-	-	-
NME7	+	+	-	-	-	-	-	-	-
LGALS3BP	+	-	-	-	-	-	-	-	-

1.9 Regulation of γTuRC by adapters

Several γTuRC adapters have been identified that regulate the subcellular targeting of γTuRC to MTOCs and/or modulate the nucleation activity of γTuRC. These factors can be divided into two classes based on the presence of conserved sequence motifs that are necessary to bind γ-tubulin complexes. Whereas one class contains centrosomin (CM1) motifs, the other does not.

1.9.1 Non-CM1 adapters

Non-CM1 adapters comprise proteins such as CEP192, NIN, NINL, or NEDD1 (71, 149). NEDD1 (Grip71 in *D. melanogaster*) is the crucial factor in animal cells that recruits γTuRC to the centrosome (127, 128, 150–152). In addition, NEDD1 is also required to recruit γTuRC to non-centrosomal MTOCs such as the lattice of pre-existing microtubules. This occurs for example at spindle microtubules or in the interphase microtubule network and additionally requires augmin, another multi-protein complex (153–156). NEDD1 is also required for centriole biogenesis, which may be related to γTuRC's proposed role in nucleating the microtubules of the centriole wall (128). Two conserved domains in NEDD1 are central to facilitate γTuRC recruitment. First, the N-terminal half mediates NEDD1 localization to the centrosome, likely through a β-propeller structure formed by five WD40 repeats. Second, an alpha-helical domain in the C-terminal half mediates the binding to

γTuRC (127, 128). This domain oligomerizes and can bind γ-tubulin *in vitro* (152) but does not alter microtubule nucleation activity of γTuRC (157). It should be mentioned that NEDD1 binding to isolated γ-tubulin was observed using purified γ-tubulin produced in *E. coli* under denaturing/refolding conditions. As mentioned above, γ-tubulin requires folding by chaperones that only exist in eukaryotes. As no quality control of the purified protein was presented by the authors, the binding activity to NEDD1 must be taken with a grain of salt. *D. melanogaster* NEDD1 also binds to individually expressed GCP2, GCP3, GCP5, and GCP6 (158), but in human cells NEDD1 seems to preferentially bind γTuRC rather than individual subunits or subcomplexes (113, 127). Moreover, the interaction between NEDD1 and γTuRC was shown to require MZT1 (113). Additionally, one study has presented evidence that depletion of NEDD1 by RNAi affects γTuRC integrity, arguing it may perhaps also have a structural role (128). Overall, the current view is that NEDD1 mediates the interaction of γTuRCs with MTOCs but the molecular details of this interaction, and how NEDD1 interacts with γTuRC, remain poorly understood.

1.9.2 CM1 adapters

The second class of γTuRC adapters are large proteins consisting of coiled-coils and disordered regions but also harboring a conserved CM1 motif. Multiple coiled-coils in large polypeptide chains are often found in scaffold proteins as such structures can allow a protein to multimerize with itself, or even with similar domains in other proteins, while at the same time being able to span over relatively large space (159). While the molecular principles of coiled-coiled domain interactions are so far best understood for non-centrosomal proteins, it remains elusive how these protein domains contribute to the higher-order centrosome structure. In some cases, CM1 motifs found in different proteins and species are degenerated at the primary sequence level but in most cases have been show to mediate binding to γ-tubulin complexes.

When ectopically expressed in cells, the isolated ~50 amino acid CM1 motif of CDK5RAP2 (CnnT in *D.melanogaster*) activates microtubule nucleation from γTuRC in the cytoplasm, effectively bypassing MTOC-restricted nucleation activation (126). This observation has coined describing the CM1 motif γTuNA (γ-tubulin nucleation activator). Like NEDD1, CM1 binding to γTuRC requires MZT1, and MZT1 depletion abolishes CM1-mediated nucleation activation from γTuRC (113, 135). Consistent with its

proposed role in γTuRC binding and activation, recombinant CM1 motif can be used to purify γTuRC from cell extracts. Curiously, the CM1 tends to dissociate during the purification procedure, suggesting that the CM1-γTuRC interaction may not be stable under the conditions used (126, 160). Nevertheless, when added back in an *in vitro* nucleation assay purified CM1 motif can directly activate nucleation activity of purified native human γTuRC (126, 157). Interestingly, CM1 cannot activate purified native *X. leavis* γTuRC in a similar assay setup (145). Thus, the interaction mode of CM1 and γTuRC as well as the mechanism of CM1-mediated nucleation activation remains to be determined. Further complexity towards this goal is likely added by inter-species differences and low affinity interactions. In fact, interaction stabilizing elements may not even require additional proteins, since a larger CM1-containing fragment of CDK5RAP2 interacts with MZT1, whereas the isolated CM1 motif does not (135).

More insights into γ-tubulin complex regulation by adapters come from studies in fungi. In contrast to animals which display open mitosis, fungi do not break down their nuclear envelope during mitosis. To form spindle microtubules, fungi nucleate microtubules from two distinct sites at spindle pole bodies, the nuclear and cytoplasmic site, where distinct CM1 factors mediate γ-tubulin complex recruitment. On the nuclear side these are *S. cerevisiae* Spc110 and *S. pombe* Pcp1, which are thought to be orthologues of PCNT. On the cytoplasmic side are *S. cerevisiae* Spc72 and *S. pombe* Mto1, which are thought to be orthologues of CDK5RAP2. Notably, while vertebrate PCNT shows interaction with γ-tubulin, GCP2, and GCP3 in cellular assays, PCNT lacks a conserved CM1 motif (149, 161, 162). PCNT may therefore use a different mode to bind to γ-tubulin complexes, perhaps enabling simultaneous binding of CM1 and PCNT in these organisms.

As described in Section 1.6, Spc110 can mediate oligomerization of *S. cerevisiae* γTuSC into nucleation complexes. A similar oligomerization activity has not been shown for Spc72, however, Spc72 can simultaneously bind to γ-tubulin complexes and the microtubule polymerase Stu2 (163). Direct coupling of a microtubule polymerase to a nucleation template represents an attractive model to explain the overall low nucleation activity observed for isolated γ-tubulin complexes.

In fission yeast, the CM1-containing protein Mto1 is the main γ-tubulin complex receptor at spindle pole bodies and cytoplasmic MTOCs where it acts together with Mto2 to recruit

fission yeast γTuSC to form microtubule nucleation complexes (164). Mto1 and Mto2 form a complex, which can recruit fission yeast γTuSC, leading to formation of γTuRC-like rings (140). These γTuRC-like rings support microtubule nucleation *in vitro*, arguing for a concerted Mto1/Mto2-mediated recruitment-activation mode of γ-tubulin complexes in fission yeast. On a structural level, preliminary results indicate that separate oligomerization domains present in Mto1/Mto2 can interact with each other to form higher-order oligomers, which in turn may influence positioning of γTuSCs upon recruitment (165).

Spatial separation of γTuRC assembly from activation, as observed in animal cells, may not only prevent uncontrolled nucleation but also provide additional means of regulation. For example, similar to the activation step, assembly of γTuRC could be subject to specific control. This may explain why, to date, more than two decades after the discovery of γTuRC (97, 98), the field has been unsuccessful in reconstituting γTuRC from recombinant proteins *in vitro*.

1.10 Folding chaperones and assembly chaperones as γTuRC interactors

Chaperones and chaperone-like proteins are yet another class of proteins commonly found to copurify with γTuRC (122, 133). These proteins are predominantly known for preventing newly synthesized and stress-denatured proteins from aggregation and assist them in folding into their native structure (166). This emphasis falls short in appreciating the fact that the term ‘chaperone’ was originally coined to describe nucleoplasmin, a nuclear protein that can coordinate assembly of folded histones into oligomeric structures with DNA to yield what we commonly call a nucleosome (167), and thus by default an essential mechanism even under non-stress conditions. From a mechanistic perspective, assembly of multiprotein complexes - such as γTuRC - requires several subunits to come together through random, diffusion-limited collision. With an increasing number of subunits, this results in a remarkable number of possible assembly intermediate permutations each with its own kinetic parameters (168, 169). Importantly, this scenario assumes that each subunit can exist in a stable, folded state that can ‘scan’ its environment for interaction partners. This poses a serious challenge in the environment of the cytosol where molecular crowding favours non-specific, unproductive interactions (170–172). As a result, isolated subunits of macromolecular complexes are often prone to aggregation or misassembly in cells (169).

Unsurprisingly, cells have evolved specialized mechanisms to facilitate multiprotein complex assembly. Prominent examples are the proteasome, Rubisco, or histones (173, 174), and involves for example stable subcomplexes, which also exist in the case of γTuRC. From a substrate perspective, folding of a single polypeptide chain into its stable form is determined only by its own sequence, whereas assembly is characterized by association of two or more folded polypeptide chains into a functional complex or oligomer. Consequently, quaternary structure can only be generated by assembly, and not by folding. Importantly, however, also assembly can generate changes in protein conformation, so the conceptual distinction into folding chaperones and assembly chaperones is reasonable but not absolute (174).

One well-studied family of chaperones are the heat shock protein (Hsp) ATPases, which in eukaryotes comprise Hsp/Hsc70, Hsp90, and the chaperonin CCT (also known as TRiC) systems (175, 176). Hsp70/Hsc70 works together with its cochaperone Hsp40 and is understood to recognize hydrophobic side chains of proteins and guide them through productive folding pathways using ATP-hydrolysis driven cycles of protein binding and release. Hsp70/Hsp40 can act co-translationally to complete protein folding upon exit of the nascent polypeptide chain from the ribosome (177). Hsp70/Hsp40 assistance is often needed to form multidomain proteins that rely on the sequential folding of domains independent from each other to avoid potentially interfering interactions (178). Folding of the substrate may be completed by Hsp70/Hsp40, or alternatively require transfer to CCT or Hsp90 by either Hsp70/Hsp40 itself or by the multiprotein complex prefoldin. CCT assists in folding of an estimated 10% of the proteome, including actin, and as mentioned above, α-, β-, and γ-tubulin (179–183). In agreement with its role as an obligate γ-tubulin biogenesis factor, some CCT copurifies with γTuRC in γ-tubulin and GCP3 affinity purifications (122, 133). Although a very recent preprint has provided first structural insights into how CCT folds tubulins (23), the mechanisms of tubulin biogenesis are still poorly understood.

1.11 RUVBL1-RUVBL2 AAA ATPases

RUVBL1 and RUVBL2 are other chaperone-like proteins found in γTuRC purifications (122). RUVBL1 and RUVBL2 are two closely related AAA ATPases that are conserved and essential in all eukaryotes. RUVBL1 interacts with α- and γ-tubulin in coIP

experiments, colocalizes with microtubules at centrosomes and in the mitotic spindle, and is required for the assembly and organization of microtubules in mitosis (184, 185). While the mechanisms underlying these activities are not understood, the current view is that RUVBL1-RUVBL2 complexes function in the assembly of multiprotein complexes important for a wide range of processes such as chromatin remodeling, transcription, ribosome biogenesis, and signal transduction (186, 187).

While RUVBL1 and RUVBL2 can form both homohexamers and heterohexamers (1:1 stoichiometry) *in vitro* (188–192), the hetero-oligomeric RUVBL1-RUVBL2 complexes seem to be biologically most relevant as both subunits copurify with each other and depletion of either one destabilizes the other (193, 194). Dodecameric forms made of two heterohexamers also exist, which are thought to be inactive forms of RUVBL1-RUVBL2 (190, 195, 196). For simplicity, I will hereafter use the short form 'RUVBL' when referring to heterohexameric RUVBL1-RUVBL2. RUVBL has a characteristic doughnut shaped structure typical for AAA ATPases (**Figure *7*A**). Whereas the ATPase domain with the nucleotide binding pocket forms the AAA core fold on one surface, the so-called DII domains are located on the other surface. DII domains are unique to RUVBL1 and RUVBL2 and are involved in binding most of RUVBL substrates. Generally, RUVBL1-RUVBL2 is known to engage with substrates in two different ways. First, it teams up with other cofactors to function as assembly chaperone of multiprotein complexes, or second, it becomes a structural component of the complex itself.

One of the best described structural roles of RUVBL are as integral subunits of the SRCAP (SWR1 in yeast) and INO80 chromatin remodeling complexes (197, 198). Structural analyses of these complexes have shown that RUVBL's main function is to provide a scaffold onto which the other subunits can assemble. At its DII domain face, RUVBL coordinates the catalytic domain of INO80 or SRCAP on one side, while the other side is occupied by regulatory proteins such as actin-related proteins (ARPs). Interestingly, RUVBL uses its DII face to accommodate large insertion domains found in both INO80 and SRCAP, and guides it towards the opposite face where it can interact with ARPs (**Figure *7*B**). The insertion domains are activators of RUVBL ATPase activity and are thought to cause conformational changes in the DII domains needed for assembly. Overall, the interplay between RUVBL and the insertion domains of both motor proteins are thought

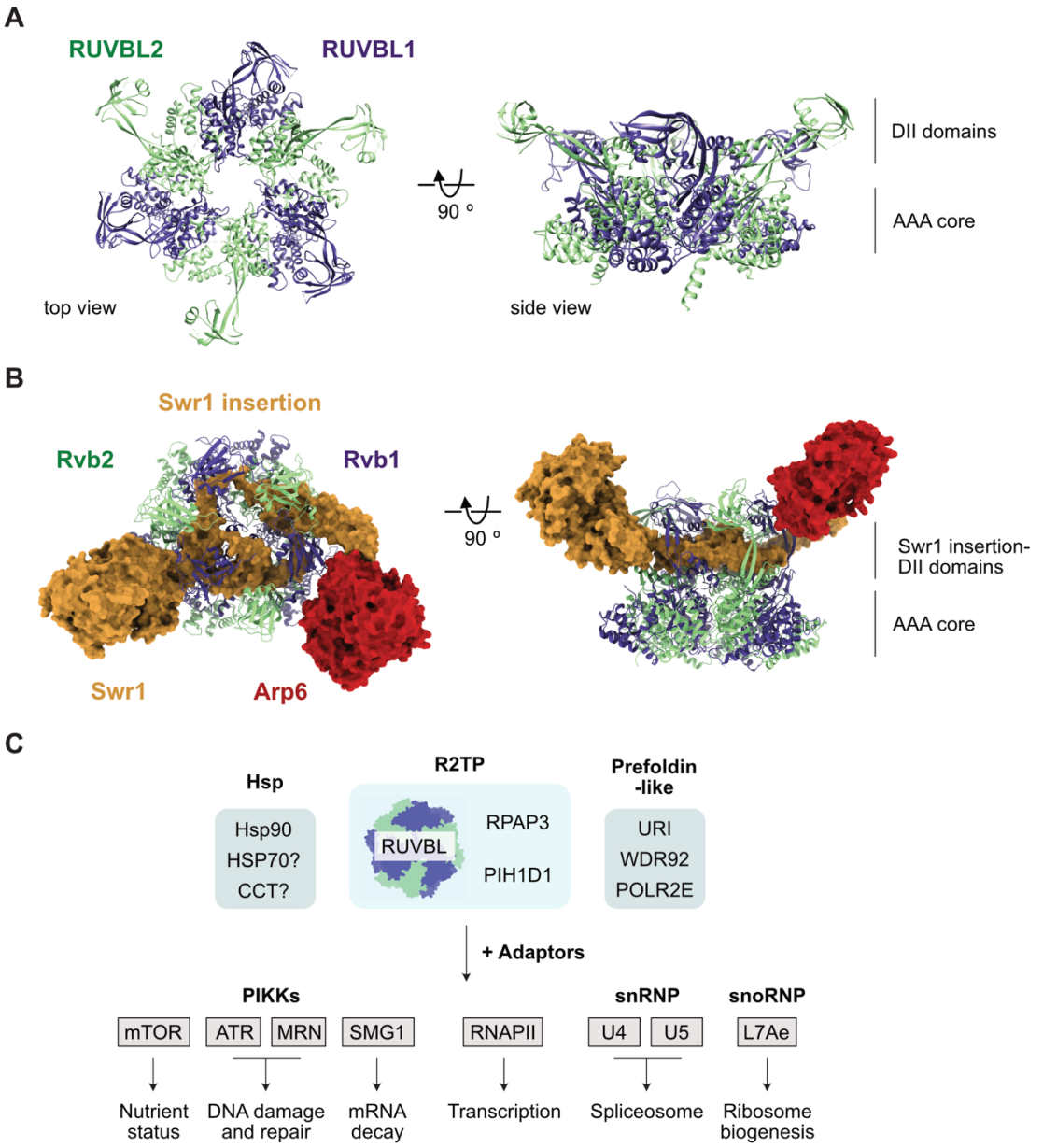

Figure 7: RUVBL1-RUVBL2 AAA ATPases. (A) Structure of a RUVBL1-RUVBL2 hexamer with AAA core and external DII domains. Crystal structures of RUVBL1 (purple, PDB 2C9O) and RUVBL2 (green, 6H7X) were docked into heterohexameric RUVBL1-RUVBL2 (2XSZ) using ChimeraX. (B) Structure of the *S.cerevisiae* Swr1 nucleosome remodeller (PDB 6GEJ). The insertion domain of Swr1 (orange) is bound to Rvb1-Rvb2 (shown as their human homologues as in (A)) via the Rvb DII domains and connects to Arp6. (C) Overview over R2TP-based chaperone systems involved in assisting the assembly of multiprotein complexes involved in a wide range of cellular processes.

to create the inherent asymmetric structure of INO80 and SRCAP that is essential to carry out their function on chromatin (198–200). Apart from its function as structural subunit, RUVBL is known to assist in assembly, maturation, and activation of many multiprotein complexes without being part of the final complex. Here, RUVBL teams up with the cofactors RPAP3 and PIH1D1 to form R2TP (Rvb1-Rvb2-Tah1-Pih1, using the yeast

nomenclature). R2TP is a specialized Hsp90 cochaperone that is necessary for assembly of spliceosomal U4 and U5 snRNP, L7Ae snoRNP for ribosomal biogenesis, RNAPII for transcription, and various kinases of the PIKK family involved in nutrient and stress signalling (**Figure *7*C**) (187, 201). Instead of Hsp90, R2TP can also engage with a Prefoldin-like complex that includes URI, WDR92, and POLR2E to form the PAQosome (particle for arrangement of quaternary structure, named after its proposed function) (186, 202). Still, a detailed understanding of the R2TP-based chaperone systems is lacking. For example, some of their functions may be independent of PIH1D or RPAP3 (187) and whether Hsp70 and CCT work together with the PAQosome is controversial (203). Adding additional complexity, R2TP-mediated assembly of multiprotein complexes often requires coordination by additional adaptor proteins (204, 205).

While mechanistic details of PAQosome activity remain to be discovered, recent studies have made progress in understanding R2TP. In R2TP, the cofactors PIH1D1 and RPAP3 cooperate to recruit substrates and Hsp90 to RUVBL. While PIH1D1 can recognize phosphorylated substrates, RPAP3 is responsible of coupling Hsp90 to R2TP. A recent study has found that PIH1D and RPAP3 binding to RUVBL activate its ATPase activity and promote nucleotide exchange (206). RUVBL1 and RUVBL2 both contain flexible N-terminal tails that act as gate keepers that stabilize the bound nucleotide (190, 195). Muñoz-Hernández *et al.* (206) originally showed that PIH1D1-binding to RUVBL results in a conformational change in one RUVBL2 DII domain, which is accompanied by rearrangement of the N-terminal tail. The N-terminal tails loses its gate keeper function and triggers release of ADP from the RUVBL2 subunit, making it available to bind a new ATP molecule. Interestingly, a more recent study questioned these results and did not find any significant stimulation of RUVBL ATPase activity or increased nucleotide exchange by RPAP3-PIH1D1 (207). Another RUVBL substrate is DHX34, an RNA helicase involved in NMD, which has been shown to downregulate RUVBL ATPase activity upon interaction with RUVBL (208). At a molecular level, DHX34 binding to RUVBL induces similar changes as PIH1D1 binding but triggering release of nucleotide from all three RUVBL2 nucleotide binding pockets. Downregulation of ATPase activity in this case is thought to keep the complex in a temporally inactive state until further subunits arrive to continue assembly. This reminds of some Hsp90-only substrates that can be inherently unstable in their native form and are kept in an inactive, Hsp90-bound state until an activation signal releases and activates them (209).

In summary, RUVBL is a versatile AAA ATPase involved in formation of a variety of multiprotein complexes. RUVBL can be either a structural component of these complexes or assist in their assembly as part of a larger chaperone network, whose physiological implications and mechanistic details we are only beginning to understand. Despite this, or perhaps because of that, a role for RUVBL in assembly of γTuRC has not yet been considered.

2. Objectives

In order to overcome current limitations in understanding the γTuRC and γTuRC-mediated microtubule nucleation, I followed four main objectives during my doctorate:

1. Reconstitution of γTuRC from a minimal set of components.
2. Identification and characterization of factors necessary for γTuRC assembly.
3. Production of recombinant γTuRC and γTuRC subcomplexes for functional and structural analysis.
4. Analysis of the assembly mechanism of γTuRC.

3. Materials and Methods

3.1 Cloning and plasmids

Plasmids for baculovirus-mediated expression in insect cells were cloned using the biGBac system (**Figure 8**) (210, 211). Coding sequences of full length γ-tubulin (TUBG1), MZT1, MZT2B, GCP2, GCP3, GCP4, GCP5, GCP6, RUVBL1, and RUVBL2 were amplified from respective cDNA by PCR and cloned into pLIB using Gibson Assembly reaction (NEB) or restriction endonucleases (**Figure 8A**). Purification tags were encoded in the reverse primer used for PCR amplification or introduced subsequently with restriction endonucleases. GCP3^{His6} contains a hexahistidine tag preceded by a pentaglycine linker at the C-terminus of GCP3 to form GCP3-GGGGGG-HHHHHH. GCP3$^{3C\text{-}TwinStrep}$ and GCP6$^{3C\text{-}TwinStrep}$ contain a TwinStrep-tag preceded by a HRV 3C cleavage site, preceded by an alanine-serine linker at the C-terminus of GCP3 or GCP6 to form GCP3- or GCP6-AS-LEVLFQGP-SSWSHPQFEKGGGSGGGSGGGSSWSHPQFEK, respectively. GCP5$^{mBFP\text{-}Avi\text{-}TEV\text{-}ALFA}$ contains a monomeric blue fluorescent protein (mBFP) preceded by an alanine-serine linker, followed by a biotin acceptor peptide, a 5x glycine linker, a TEV protease cleavage site, and an ALFA-tag, to form GCP5-AS-mBFP-$(G)_5$-GLNDIFEAQKIEWHE-ENLYFQG-PSRLEEELRRRLTE. Clones were analyzed by restriction endonuclease digestion and verified by sequencing. Following verification, cassette (Cas) primers were used to amplify gene expression cassettes (GECs) from pLIB vectors with desired homology arms and cloned into pBIG1 plasmids using Gibson Assembly reaction (**Figure 8B**). Correct assembly of poly gene cassettes (PGCs) into pBIG1 was verified by SwaI and PmeI digestion and sequencing. Using different combinations of pBIG1 plasmids, PGCs were released from pBIG1 plasmids by PmeI digestion and cloned into pBIG2 plasmids using Gibson Assembly reaction. Correct assembly of PGCs into pBIG2 plasmids was verified by SwaI and PacI digestion (**Figure 8C**). For generation of expression constructs for mutant γTuSCs, GCP2$_{126\text{-}902}$ (GCP2 ΔH1-H6), GCP3$_{111\text{-}907}$ (GCP3 ΔH1-H5) and GCP3$_{245\text{-}907}$ (GCP3 ΔH1-H5 Δ3L) were amplified from respective cDNA by PCR and integrated into the biGBac system as described above.

For expression of 3xFLAG-tagged GCPs, Nt-GCPs, and Nt-GCP ΔNTE fragments in HEK293T cells, the corresponding regions were amplified by polymerase chain reaction

(PCR) were amplified by PCR and cloned into pCS2+-based vector encoding an N-terminal 3xFLAG tag and carrying a modified cloning site with FseI and AscI restriction sites.

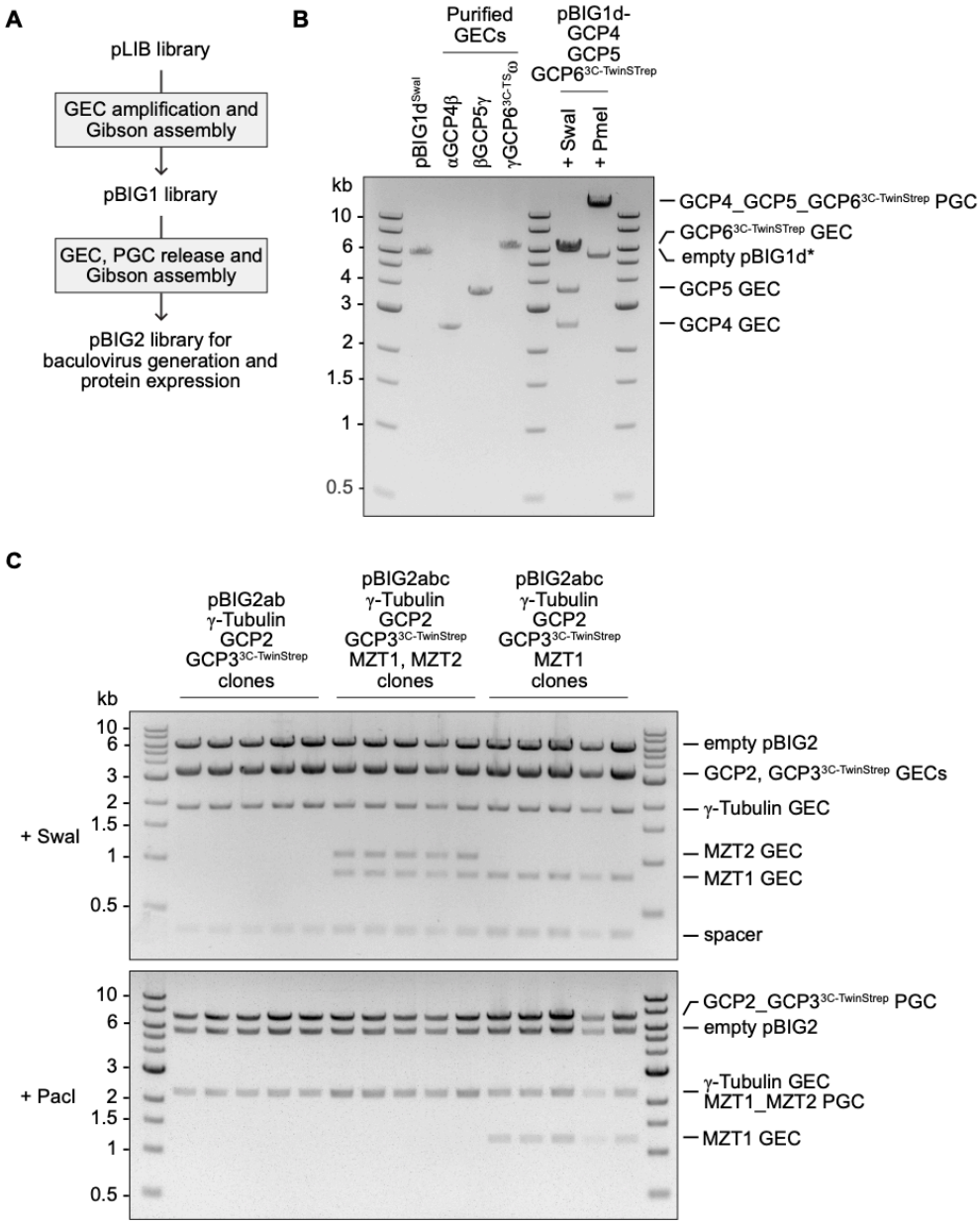

Figure 8: A biGBac system for recombinant expression of γTuRC subunits in insect cells. (A) Cloning scheme for biGBac-based vector library for human γ-tubulin complexes. (B) Ethidium bromide (EtBr) stained native agarose gel showing cloning of pBIG1d-GCP4_GCP5_GCP6$^{3C\text{-}TwinStrep}$ by Gibson Assembly of amplified GECs into linearized pBIG1d. (C) EtBr-stained native agarose gel showing examples for cloning of pBIG2 plasmids for coexpression of γTuSC subunits. 5 clones were analyzed for each construct.

3.2 Cell culture and treatments

HeLa and HEK293T cells were grown in Dulbecco's modified Eagle's medium (DMEM) + 10% fetal calf serum + 100 U/mL penicillin + 100 µg/mL streptomycin at 37°C and 5% CO_2. For siRNA treatment, HeLa cells were transfected with either Luciferase Control siRNA (Thermo Fisher) or RUVBL1 siRNAs (212) using Lipofectamine RNAiMAX (Life Technologies), and analyzed after 68-72 h. For immunofluorescence microscopy, cells were grown on poly-D-lysine coated coverslips and fixed with either 3.6% paraformaldehyde (Sigma Aldrich) at room temperature or ice-cold methanol. For co-expression of EGFP-MZT2 and 3xFLAG-GCP2 fragments, HEK293T cells were transfected using Lipofectamine 2000 (Life Technologies) and harvested after 24 h. For expression of 3xFLAG-GCPs -NtGCP and -NtGCP ΔNTE fragments, $3*10^6$ HEK293T cells were seeded in a 10 cm dish the day before transfection. The following day, cells were transfected with 10 µg plasmid DNA with 40 kDa linear PEI (Polysciences) pH 7.0 at a DNA:PEI ratio of 1:3 (w/w) diluted in Opti-MEM (Gibco). Transfection mix was removed 4 h after transfection and cells were harvested after 24 h.

For baculovirus generation and protein expression, *S.frugiperda* (Sf9) cells (Thermofisher) were grown in suspension in Sf-900 III SFM (Gibco) + 25 U/mL penicillin + 25 µg/mL streptomycin at 27°C, at 120 rpm with 25 mm shaking throw.

3.3 Sucrose gradient centrifugation

For cell extract fractionation, HeLa cells were harvested, washed with PBS and lysed in Buffer A (50 mM HEPES pH 7.2, 150 mM NaCl, 5 mM $MgCl_2$, 1 mM EGTA, 0.5% IGEPAL CA-630, 2 mM β-mercaptoethanol, 2x protease inhibitors EDTA-free (Roche), 1x PhosSTOP phosphatase inhibitors (Roche) on ice. Cleared extracts were prepared by centrifugation for 20 min at 16,100 x *g* at 4°C. Protein concentration was determined by Bradford assay (Bio-Rad) and adjusted with Buffer A. 250 µL of extract was then loaded onto a 4.2 mL 10-40% linear sucrose gradient prepared in Buffer B (Buffer A without IGEPAL CA-630, protease inhibitors, phosphatase inhibitors). For analysis of recombinant proteins, 250 µL of affinity purified sample was loaded onto a 4.2 mL 10-40% linear sucrose gradient prepared in Buffer E (described below). For γTuRC constructs purified by preparative gradients, 550 µL of sample was loaded onto a 4.2 mL 10-35% linear sucrose gradient prepared in Buffer E. Centrifugation was carried out using an MLS-50 rotor at

50,000 rpm for 4 h at 4°C or 3 h at 4°C for the 10-35% gradient. 10-40% gradients were fractionated from top to bottom in 300 µL fractions, and the 10-35% gradients in a 550 µl top fraction, and 350 µL fractions for the rest from top to bottom.

3.4 Immunofluorescence microscopy

Fixed cells grown on coverslips were washed with PBS to remove residual methanol before blocking in PBS-BT (PBS, 3% BSA, 0.1% Triton X-100) for 30 min at room temperature. Blocked coverslips were then consecutively incubated with primary and secondary antibodies diluted in PBS-BT as indicated for 30 min at room temperature, with thorough washes with PBS-BT in between the incubation steps. DNA was stained with 0.5 µg/mL DAPI (diluted in PBS-BT) for 2 min at room temperature. Stained coverslips were mounted on glass-slides using ProLong Gold Antifade (Thermofisher). Immunofluorescence microscopy was performed using a DMI6000B microscope (Leica) with 1.4 NA 63x and 100x oil immersion objectives. Images were acquired with an Orca AG camera (Hamamatsu) and AF6000 software (Leica). Image processing and quantification of fluorescence intensities was performed with ImageJ software. Intensities were measured in images acquired with constant exposure settings and background-corrected. Antibodies used for immunofluorescence microscopy were: rabbit anti-MZT2 (122), mouse anti-NEDD1 (7D10; Sigma-Aldrich); mouse anti-α-tubulin (DM1A, Sigma-Aldrich); mouse anti-centrin (20H5, Sigma-Aldrich). Alexa-Fluor-488 and Alexa-Fluor-568- secondary antibodies were purchased from Thermo Fisher. For co-labeling with two mouse primary antibodies, isotype-specific secondary antibodies were used.

3.5 Bacmid and bacoluvirus generation

Bacmids were generated by Tn7 transposition of pBIG2-based constructs into the EMBacY baculovirus genome as described (211). Baculoviruses were generated as described (213) with minor modifications. Briefly, freshly prepared bacmid DNA was diluted in sterile filtered, prewarmed PBS and mixed with 40 kDa linear PEI pH 7.0 at a DNA:PEI ratio of 1:2 (w/w). The amount of bacmid DNA for transfection was 1µg bacmid DNA per 1 mL Sf9 culture. Following mixing, DNA:PEI complexes were allowed to form for 20-25 min at room temperature. For transfection, DNA:PEI complex was added dropwise to 15-25 mL Sf9 cells at 10^6 cells/mL culture and incubated 5 days at 27°C. 5 days after transfection the infection status was evaluated by the fraction of YFP-positive Sf9 cells using an Eclipse

Ts2 microscope (Nikon). P_0 virus was harvested if >90% of Sf9 cells were positive for YFP expression. To harvest P_0 virus, cells were pelleted at 300 x *g* for 5 min, the supernatant was recovered, filtered through a 0.2 µm syringe filter (GE healthcare) and stored at 4°C. Further virus amplification steps were omitted.

3.6 Baculovirus-mediated protein expression in insect cells

For expression of multi-subunit protein complexes, Sf9 suspension cultures at 10^6 cells/mL density were infected with P_0 virus at a ratio of 1:100 (V:V) relative to suspension culture volume. After 68-72 h of incubation at 27°C, cells were harvested and pelleted at 300 x *g* for 5 min, washed with PBS and either used directly for purification or snap frozen in liquid nitrogen and stored at -80°C until use.

3.7 Protein complex purification

γTuSC:

For purification of recombinant human γTuSC we used a TwinStrep-tag preceded by a 3C protease cleavage site fused to the C-terminus of GCP3. Following multi-subunit expression, insect cell pellets were resuspended in 5 mL Buffer C (50 mM Tris pH 8.0, 200 mM NaCl, 1 mM $MgCl_2$, 1 mM EGTA, 2 mM β-mercaptoethanol, 0.1% IGEPAL CA-630, 2x protease inhibitors EDTA-free) per gram of cell pellet, lysed using a dounce tissue grinder (Sigma) with 20 strokes on ice, and centrifuged for 25 min at 20,000 x *g* at 4°C. Cleared cell extracts were recovered, supplemented with 2.5 mg avidin (E-proteins) and 625 U Universal Nuclease (Pierce) or Denarase (C-lecta) per 10 mL of extract, and incubated 5 min on a tube roller mixer at 4°C. γTuSC was then bound by gravity flow to 1 mL StrepTactin XT Superflow High Capacity (IBA) resin equilibrated in Buffer D (Buffer C without IGEPAL CA-630, protease inhibitors EDTA-free) per liter suspension culture, washed with 10 column volumes (CV) Buffer D + 0.1 mM GTP (Carbosynth), and subsequently with 10 CV of Buffer E (Buffer D containing HEPES pH 7.5 instead of Tris pH 8.0) + 0.1 mM GTP. To elute γTuSC, the resin was resuspended in 1.5-2 CV Buffer E + 0.1 mM GTP and digested with 100 µg 3C protease per 1 mL resin for 12-16 h on an incubator wheel at 5-7 rpm at 4°C. To remove His-tagged 3C protease, the recovered eluate was gravity flown over 50 µL of Ni-Sepharose (GE healthcare) equilibrated in Buffer E + 0.1 mM GTP. After protease removal, γTuSC was centrifuged at 16,100 x g for 10 min at 4°C, concentrated using Vivaspin 500 devices with 30 kDa MWCO (Sartorius), centrifuged

again at 16,100 x *g* for 10 min at 4°C, aliquoted at 2.8-4.5 mg/mL, snap frozen in liquid nitrogen and stored at -80°C until further use. Usually, the yield was ~1 mg γTuSC per 1 L expression culture. The concentration of γTuSC was determined by UV/Vis spectroscopy using a Nanodrop (Thermofisher).

RUVBL1-RUVBL2:

Recombinant ^{His8}RUVBL1-RUVBL2 complex was purified as described (214) and contributed by Marina Serna (Oscar Llorca group, CNIO, Madrid).

γTuSC-RUVBL1-RUVBL2:

Recombinant human γTuSC-RUVBL1-RUVBL2 was either purified from Sf9 cells infected with a single baculovirus clone or reconstituted from separately purified complexes. γTuSC-RUVBL1-RUVBL2 generated by co-expression was purified as described for γTuSC but omitting removal of 3C protease.

To generate γTuSC-^{His8}RUVBL1-RUVBL2, γTuSC was first purified from a 1 g insect cell pellet as described up to the affinity purification step. After γTuSC binding to 0.25 mL StrepTactinXT Superflow High Capacity, the resin was washed and resuspended in 3 CV Buffer E + 0.1 mM GTP. 250 µg of purified recombinant ^{His6}RUVBL1-RUVBL2 was added either to γTuSC-bound resin or 0.25 mL StrepTactinXT Superflow High Capacity (equilibrated successively in Buffer D and E + 0.1 mM GTP) and incubated 30 min at 4ºC on an incubator wheel at 7 rpm. Unbound ^{His8}RUVBL1-RUVBL2 was removed by washing the resin in batch twice with 3 CV of Buffer E + 0.1 mM GTP. γTuSC-^{His8}RUVBL1-RUVBL2 was then eluted by adding 25 µg 3C protease and incubated for 12-16 h on an incubator wheel at 5-7 rpm at 4°C. Following elution, γTuSC-^{His8}RUVBL1-RUVBL2 was centrifuged at 16,100 x *g* for 10 min at 4°C, and either concentrated using Vivaspin 500 devices as described for γTuSC or directly snap frozen in liquid nitrogen and stored at -80°C until further use.

γTuRC:

For purification of recombinant human γTuRC, I used a TwinStrep-tag preceded by a 3C protease cleavage site fused to the C-terminus of GCP6. Following multi-subunit expression, insect cell pellets were resuspended in 5 mL Buffer C + 1x PhosSTOP

phosphatase inhibitors (Roche) + 0.1 mM GTP per gram of cell pellet, lysed using a dounce tissue grinder with 20 strokes on ice, and centrifuged for 25 min at 20,000 x g at 4°C. Cleared cell extracts were recovered and supplemented with avidin and nuclease as described for γTuSC. γTuRC was then bound by gravity flow to 0.5 mL equilibrated StrepTactin XT Superflow High Capacity resin per liter suspension culture. Resin was washed and γTuRC was eluted by 3C protease digestion as described for γTuSC. The recovered eluate was directly used for analysis by sucrose gradient centrifugation or concentrated using Vivaspin 500 devices with 30 kDa MWCO, centrifuged at 16,100 x *g* for 10 min at 4°C, either snap frozen in liquid nitrogen and stored at -80°C, or stored on ice until further use. I usually obtained ~0.2 mg γTuRC per 1.5 L expression culture. The concentration of purified γTuRC was determined by comparison to a BSA dilution series on the same SDS-PAGE. The BSA band with equal band intensity to GCP3 in purified γTuRC was determined by visual inspection, and the corresponding BSA concentration was used to calculate γTuRC concentration assuming five GCP3 copies per γTuRC.
For γTuRC constructs with GCP5$^{mBFP\text{-}BAP\text{-}TEV\text{-}ALFA}$, a 750 mL Sf9 culture at 1.5*10^6 cells per mL culture was infected with P_0 virus at 1:75 (V:V). Here, 2 ml StrepTactin XT 4Flow High Capacity (IBA) was used, 0.25 mg 3C protease was added per mL resin, and digestion was shortened to 2 h. Following eluate recovery, the samples were dialyzed against Buffer E + 25% glycerol + 0.1 mM GTP for 3 h at 4°C. Dialyzed samples were recovered and purified by sucrose gradient centrifugation as described above. γTuRC peak fractions were pooled, aliquoted and snap frozen in liquid nitrogen and stored at -80°C. I usually obtained 0.5 mg γTuRC per 0.75 L expression culture. The concentration of γTuRC containing GCP5$^{mBFP\text{-}BAP\text{-}TEV\text{-}ALFA}$ was determined by UV/Vis spectroscopy using a Nanodrop.

Identification of minimal sets of subunits required to reconstitute γTuSC and γTuRC:
To identify the minimal set of subunits required for reconstitute both complexes in Sf9, first 20-50 mL small scale cultures were infected with single recombinant baculovirus clones to co-express various subunit combinations as described above. Following co-expression, purifications were carried out as described above for γTuRC apart from the following steps. Cell lysis was carried out by pushing resuspended cells 5 times through a 27G syringe needle (Becton Dickinson). After obtaining cleared extracts, proteins were bound to 100 µL StrepTactinXT Superflow High Capacity and purified further as described.

3.8 Immunoprecipitation

HEK293T cells were lysed 10 min on ice in lysis buffer (50 mM HEPES pH 7.4, 150 mM NaCl, 1 mM MgCl2, 1 mM EGTA, 1% IGEPAL CA-630) + 1x protease inhibitors. After centrifugation for 15 min at 16,000 x g at 4°C, cleared extracts were incubated with anti-FLAG M2 agarose (Sigma Aldrich) for 2 h at 4°C. Following incubation, beads were pelleted, washed three times with lysis buffer, boiled in Laemmli sample buffer and the samples were analyzed by western blotting. Alternatively, FLAG-tagged proteins were eluted with 0.5 mg/mL 3xFLAG-peptide (Sigma Aldrich) before analysis.

3.9 Protein gel electrophoresis and western blotting

Protein samples in Laemmli Buffer were analyzed by SDS-PAGE using 8, 10, and 12% Bis-Tris polyacrylamide gels. In some cases, we used gels with 10% followed by 20% polyacrylamide in order to retain MZT1 and MZT2 in the gel matrix while preserving separation of GCP2 and GCP3. Proteins were stained with InstantBlue (Expedeon), by adding 0.5% (V:V) Trichloroethanol (Sigma) to the gel matrix followed by stain-free imaging using UV light in a Gbox F3 (Syngene), or by western blotting. For western blotting, proteins were transferred onto nitrocellulose or PVDF membranes as described (89). For detection of GCP2, GCP3, GCP4, GCP, GCP6, MZT1, MZT2, and NEDD1, we used our own antibodies raised in rabbit as previously described (86, 89, 90). Other antibodies used for western blotting were: mouse anti-γ-tubulin (GTU-88; Sigma-Aldrich), mouse anti-FLAG M2 (F1804; Sigma-Aldrich); mouse anti-GAPDH (sc-47724, Santa Cruz), rabbit anti-RUVBL1 (10210-2-AP, Proteintech); mouse anti-RUVBL2 (sc-374135, Santa Cruz); rabbit anti-GFP (TP401, Torrey Pines Biolabs).

3.10 Chemical cross-linking

Purified γTuSC aliquots stored at -80ºC were quickly thawed and centrifuged at 16,100 x *g* for 10 min at 4°C and kept on ice. Concentration was then adjusted to 1 mg/mL (3 µM, assuming M_r(γTuSC) = 334,892) with freshly degassed Buffer E. For γTuSC-RUVBL, ^{His8}RUVBL1-RUVBL2 was added to a final concentration of 0.375 µM and incubated 30 min on ice before cross-linking. Disuccinimidyl dibutyric urea (DSBU) was freshly dissolved in DMSO (LC-MS grade, Thermo Fisher) and added to 180 µg γTuSC aliquots at final concentrations of 150, 300, 600, 1200, and 3000 µM (50, 100, 200, 400, and 1000x molar excess), mixed, and incubated for 30 min at 20ºC. As a control reaction, 1 µL DMSO

was added to a similar γTuSC aliquot, mixed, and incubated likewise. The cross-linking reaction was then quenched by adding Tris pH 8.0 to a final concentration of 100 mM followed by incubation for 30 min at 20ºC. Aliquots were taken and boiled in Laemmli Buffer for 5 min at 95ºC and analyzed by SDS-PAGE using Coomassie Brilliant Blue or stain-free imaging. Only Coomassie-stained polyacrylamide gels were used for subsequent CL-MS analysis.

3.11 Cross-linking mass spectrometry (CL-MS)

The following steps were performed and contributed by the IRB mass-spectrometry facility. Bands were excised from an 8% polyacrylamide gel and submitted to in-gel digestion. Briefly, excised gel bands were cut in smaller pieces, washed with 50 mM NH_4HCO_3 and acetonitrile (ACN), reduced with 10 mM dithiothreitol (DTT) and alkylated with 50 mM iodoacetic acid (IAA). Following this, γTuSC samples crosslinked with 200x and 1000x molar excess DSBU were digested with trypsin (Sequencing Grade Modified Trypsin, Promega), whereas the sample crosslinked 400x molar excess DSBU digested with chymotrypsin. Digestions were stopped with 5% formic acid (FA) and eluted with ACN. Sample solutions were dried completely in SpeedVac and reconstituted in 20 µL of 3% ACN, 1% FA in aqueous solution for MS analysis. Subsequently, samples were loaded to a 100 µm × 2 cm Acclaim PepMap100, 5 µm, 100 Å, C18 (Thermo Fisher) at a flow rate of 15 µL/min using a Dionex Ultimate 3000 chromatographic system (Thermo Fisher). Peptides were separated using a C18 analytical column (NanoEase MZ HSS T3 column, 75 µm × 250 mm, 1.8 µm, 100 Å, Waters) with a 90 min run, comprising three consecutive steps with linear gradients from 3 to 35% B in 60 min, from 35 to 50% B in 5 min, and from 50% to 85% B in 2 min, followed by isocratic elution at 85% B in 5 min and stabilization to initial conditions (A= 0.1% FA in water, B= 0.1% FA in ACN). The column outlet was directly connected to an Advion TriVersa NanoMate (Advion) fitted on an Orbitrap Fusion LumosTM Tribrid (Thermo Fisher). The mass spectrometer was operated in a data-dependent acquisition (DDA) mode. Survey MS scans were acquired in the Orbitrap with the resolution (defined at 200 m/z) set to 120,000. The highest charge state ions per scan were fragmented in the HCD cell and detected in the orbitrap (30,000 resolution) with stepped collision energies. The ion count target value was 400,000 for the survey scan and 10,000 for the MS/MS scan. Target ions already selected for MS/MS were dynamically excluded for 15 s. Spray voltage in the NanoMate source was set to 1.70 kV.

RF lens were tuned to 30%. The spectrometer was working in positive polarity mode and singly charge state precursors were rejected for fragmentation.

For the proteomics bioinformatics workflow, we devised a multiple software search comprising three crosslinking identifying nodes: XlinkX (v2.2) from the Thermo Scientific software Proteome Discoverer (v2.3), MeroX (v2.0.1.1) (215) and xiSEARCH (v1.7.4) (216). All searches were run against a FASTA database containing γTuSC subunits TUBG1 (P23258), GCP2 (Q9BSJ2), GCP3 (Q96CW5), MZT1 (Q08AG7), MZT2B (Q6NZ67), RUVBL1 (Q9Y265), and RUVBL2 (Q9Y230). The main search parameters for these three nodes were: trypsin or chymotrypsin as digesting enzymes allowing two missed cleavage sites (three for MeroX); carbamidomethyl in cysteine as static modification; oxidation in methionine as dynamic modification; DSBU definition as crosslinker between lysine, protein amino-terminus and lysine, serine, threonine, tyrosine, protein carboxyl-terminus; peptide mass tolerance of 10 ppm; MS/MS tolerance of 20 ppm (10 ppm for MeroX); and FDR > 1% threshold definition. We integrated the three search results in a single harmonized data set, ready to be visualized with the interactive online tool xiNET (217).

3.12 End-point *in vitro* microtubule nucleation assay

To visualize microtubules in fluorescence microscopy-based microtubule nucleation assays I used a mix of rhodamine-labelled porcine brain tubulin (Cytoskeleton) and unlabelled porcine brain tubulin (218) at a ratio of 1:10. A fresh tubulin stock mix was prepared by diluting labelled and unlabelled tubulin on ice in Assay Buffer (80 mM PIPES-KOH pH 6.9, 2 mM $MgCl_2$, 0.5 mM EGTA, 1 mM GTP) and mixed at a ratio of 1:10 to a final concentration of 50 µM. To remove tubulin aggregates, the tubulin mix was centrifuged at 50,000 rpm in a TLA-55 rotor (Beckman) for 10 min at 4ºC. After centrifugation, tubulin concentration was verified by Bradford assay (Bio-Rad). Nucleation assays were set up in PCR-tubes in 10 µL reactions by diluting 1 µL γTuRC prep (final concentration ~1 nM) and tubulin stock mix (final concentration 20 µM) with Assay Buffer on ice. While still on ice, 1 µL aliquots were taken and mixed with 9 µL pre-warmed Fixation Buffer (80 mM PIPES-KOH pH 6.9, 2 mM $MgCl_2$, 0.5 mM EGTA, 50% glycerol, 0.1% glutaraldehyde) to obtain a "0 min" sample. The assay was started by transferring the reactions to a T100 Thermal Cycler (Bio-Rad) set to 37ºC. After 5 min, 1 µL samples were taken and fixed with Fixation Buffer. Sample aliquots of 1 µL were then pipetted on microscope glass slides

(Knittel Glass) and covered with 12 mm round cover slips (Thermo Scientific). Rhodamine-labelled microtubules were imaged by fluorescence microscopy using a DMI6000B microscope (Leica) with 1.4 NA 63× oil immersion objectives. Images were acquired with an Orca AG camera (Hamamatsu) and AF6000 software (Leica).

3.14 Negative stain EM of γTuSC complexes

Aliquots of purified γTuSC (2.5 µL) were applied to carbon-coated grids and stained using 1% uranyl acetate. Samples were observed using a FEI Tecnai G2 Spirit with a Lab6 filament and operated at 120 kV. Several hundreds of micrographs were collected using an automatic low-dose data collection in a TVIPS camera and particles extracted. Images were then processed using Relion 3.1 (219) and CryoSPARC v2 (220). After 2D classification and averaging we obtained several 2D averages and we selected two representative examples containing 4,489 particles for γTuSC and 344 particles for an average showing two γTuSC associating laterally.

3.15 Negative stain structure of RUVBL-γTuSC complexes

The RUVBL-γTuSC complex was stabilized by mild cross-linking using 0.01% (v/v) glutaraldehyde for 1 h on ice with an excess of γTuSC (8-fold excess considering monomeric γTuSC as above) in a buffer containing 50 mM HEPES-NaOH pH 7.5, 200 mM NaCl, 1 mM EGTA, 1 mM $MgCl_2$ and 2 mM β-mercaptoethanol. The cross-linking reaction was stopped by adding 40 mM Tris-HCl pH 7 to the sample. The complex was purified by pulling down ^{His8}RUVBL1-RUVBL2 using the same buffer supplemented with 500 mM Imidazole. Finally, the sample was stained using 1% uranyl acetate on carbon-coated copper grids. We collected 536 micrographs using a FEI Tecnai G2 Spirit with a Lab6 filament and a TVIPS camera. 32,327 particles were extracted and subjected to image processing using Relion 3.1 and CryoSPARC v2. After classification, representative 2D averages were obtained containing around 200-300 particles per average (see details in figure legend for the selected examples). Particles were classified in 3D into more homogenous subgroup, and the sub-class containing 10,455 particles was further refined into a reconstruction at ~26 Å resolution estimated using the gold-standard criterion and a cut-off of 0.143. The negative-stain structure of RUVBL-γTuSC was interpreted by fitting low resolution versions of γTuSC and RUVBL obtained by filtering γTuSC from this work, and a RUVBL1-RUVBL2 ATPase hexamer lacking most of the domain II (DII) (PDB

2XSZ). Fitting was performed using the sequential fitting tool in UCSF Chimera without user intervention (221). UCSF Chimera fitted copies of γTuSC into each GCP pair of the low-resolution structure whereas the RUVBL ring was fitted within the extra density.

3.16 Cryo-EM of the γTuRC, sample preparation and image acquisition.

Aliquots of purified γTuRC (2.5 µL) were applied to glow-discharge holey carbon grids (Quantifoil R1.2/1.3 300-square mesh copper grids) coated with a continuous carbon film. Excess buffer was blotted away and the sample was vitrified in liquid ethane using a Vitrobot IV Mark (Thermo Fisher Scientific) set to 4 ºC and 90% humidity. Cryo-EM grids were stored at liquid nitrogen temperature.

Data were collected using EPU on a 300 kV Titan Krios G3 electron microscope (Thermo Fisher Scientific) using a Bioquantum energy filter (Gatan) and a K3 direct-electron detector operated in counting mode. A total of 13,035 movies where collected over two sessions at a pixel size of 0.545 Å/pixel and a defocus range of 1.0 to 3.0 µm underfocus. 1,686 movies were collected in the first session, with a total dose of 41.85 $e^-/Å^2$ across 45 frames (0.93 $e/Å^2$/frame). Two larger datasets were collected in a second session (11,349 movies in total) with a total dose of 58.5 $e^-/Å^2$ across 90 frames (0.65 $e/Å^2$/frame).

3.17 Image processing

Data sets were pre-processed individually and subsequently combined for data alignment, classification and 3D refinement steps. Large beam-induced motions were corrected by aligning all movie frames using MotionCor2 and 7x5 patches (222). Contrast transfer function (CTF) parameters were estimated using Gctf (223). Particles were auto-picked using Relion 3.1 after creating references from manually selected particles.

More than 2 million particles were initially selected and binned by a factor of 4 and subjected to reference-free alignment and 2D classification using Relion 3.1 and CryoSPARC v2. Using 2D classification and averaging, we selected a dataset of 139,143 best quality particles that were used to generate an initial template using the *ab initio* reconstruction tools in cryoSPARC. This starting reference was used as template for subsequent 3D classification and refinement steps. Further image processing steps were entirely carried out in Relion 3.1. After an initial 3D refinement, CTF parameters, such as

beam-tilt, magnification anisotropy as well as particle defocus and micrographs astigmatism were refined. After another run of 3D refinement, particles were individually corrected for beam-induced motion using the bayesian particle-polishing tool and consecutively input for another round of CTF refinement. Following another consensus 3D refinement that included all the selected particles, several rounds of 3D classification were carried to further improve homogeneity of the dataset by selecting the most homogenous and best quality particles. 100,182 particles were included in the final refinement of the γTuRC structure. Modulation transfer function correction and B-factor sharpening were carried out using the 'post-processing' protocols in Relion 3.1. The resolution was estimated using the gold-standard criterion and a cut-off of 0.143. We estimated 4.2 Å average resolution, with best resolution regions up to 4.0 Å after local resolution estimations. Local resolutions estimations revealed the anisotropic resolution of the map, with some regions of the complex notably more flexible than others. To improve resolutions, those regions with significant differences in their resolution values were segmented and subjected to two different strategies to improve their electron density. A soft mask was applied to each of those regions in order to remove the extra density of the complex (particle density subtraction) and carry out focused refinements.

3.18 Model building

First, subunits in the complex were identified without any bias from the structures of the native complex. γ-Tubulin and the actin-like protein were identified in the cryo-EM map by making use of available crystal structures. GCP core proteins were detected by using the available crystal structure of GCP4 (PDB 3RIP) (123). Each GCP unit in the consensus cryo-EM map was first fitted with the crystal structure of GCP4 as starting point for modelling. Each subunit was then identified by specific elements of their structure and sequence in which the resolution of the cryo-EM map was sufficient to confidently fit side chains. Assignment of GCP3 subunits was also supported by the presence of a longer C-terminal hairpin. Subsequently, homology models for GCP2, GCP3, GCP5 and GCP6 subunits were built with the I-Tasser homology modelling server (224), which used information from the previously published structure of the native human γTuRC complex (PDB 6V6S). A crystal structure was available for GCP4 (PDB ID 3RIP) (123). These models, together with the γ-tubulin crystal structure (PDB 3CB2) (93) were fitted as rigid-bodies into the corresponding electron density map (consensus map or subvolumes) using

the sequential fitting tool of UCSF Chimera, within the positions previously identified without the bias from existing structures of the native complex. The corresponding models for the γTuRC units, composed by GCP and γ-Tubulin, were refined iteratively in real space within subvolumes containing just three γTuRC units with Coot (225), Phenix (226) and Refmac5 (227). Residues absent in the initial homology model that were identified as pertaining to the extra densities observed in the GCP subunits, such as the GCP2 staples and the $GCP6_{1415-1475}$ helices, were manually assigned and refined. Since the resolution of the map in positions 13 and 14 is lower, GCP2, GCP3, and γ-tubulin molecules from positions 7/8 were rigid body-fitted in positions 13/14 using Coot. The extra densities corresponding to the staples were clearly connected to the N-terminal density of the closest GCP2 core fold in most of the γTuSC copies. To model the structure, we identified this connection and then traced back the backbone up to the staple, fitting the residues and side chains. The resolution was sufficiently high to assign long or bulky side chains, such as K164, K167, K168, F177, W180, Y182, and R184, to the arms of the staple element (**Figure *28***D). This also allowed modeling of the loops that connect the two helical arms of the staples. The C-terminal end of the GCP6 insertion domain contains a helix (residues 1484 to 1510) that connects to the N-terminal end of the second GRIP domain and was partially modeled in the published structure of native human γTuRC (PDB 6V6S). Our cryo-EM map shows two additional, preceding helices. Although resolution was not sufficient to fit side chains in any of the three helices, we could observe clear connections between all three helices. Based on this information and guided by the helical densities of the cryo-EM map and secondary structure predictions by the JPred4 server (228), we were able to model the new α-helices of residues 1415 to 1439 and 1444 to 1475. To model the luminal bridge, we first identified three well-connected helices in bundle 2 whose N- and C-terminal helices were not connected to any other density, indicating that they were a separate protein and not part of the GCPs. A prediction of MTZ1 tertiary structure performed using the I-TASSER server was fitted as rigid body fitting into the cryo-EM density as a start for modeling. Subsequently, the identification of bulky amino acid side chains was used to unequivocally assign the protein sequence of MTZ1 to the model, which was refined in real space with Coot, Phenix, and Refmac. MTZ1 in bundle 2 was embedded within a five-helix bundle that we identified as GCP3 NTEs as follows. The connectivity between the five helices of the bundle in the cryo-EM map was identified using denoising and sharpening tools. Helix H5 in the bundle was identified in the cryo-EM map of bundle 2 as the short

C-terminal helix in closer contact with MTZ1. H5 has been predicted in GCP3, GCP5, and GCP6 as a short helix containing the MTZ1-binding motif (113). This motif contains residues with large side chains, W90 and Y95 in GCP3, Y108 in GCP5, but none in GCP6. Residues at the immediate N- and C-terminal ends of H5 do not have large side chains in any of the three proteins. Since H5 is not very long and the resolution in the cryo-EM density was sufficiently high to identify large side chains, we were able to assign H5 as GCP3. Cryo-EM density of H5 in bundle 2 shows two prominent side chains that could only be fitted by W90 and Y95 in GCP3. Then, we were able to build a model for the remaining helices of the bundle, and the good agreement of large side chains with the cryoEM density corroborated the assignment. Bundle 1 was found to be very similar to bundle 2 after a 180° rotation, and this was used to identify a second molecule of MTZ1. Using similar procedures to those described for bundle 2, we identified H5 in this bundle as GCP6 because large side chains of residues Y95 and W90 in GCP3 and Y108 in GCP5 could not be accommodated in the density, whereas H5 in GCP6 lacks residues with large side chains. Then, we modeled the remaining helices confirming this assignment thanks to the good agreement of side chains and the cryo-EM map. During preparation of this manuscript, structures of the bundles in the luminal bridge were published, and our model and register of helices agree with the published structures (229, 230). For bundle 1, resolution of the map did not allow modeling of helices H1 and H2, and these were left as a poly-alanine model.

4. Results

4.1 The RUVBL1-RUVBL2 complex is required for γTuRC integrity

To test the idea that RUVBL may play a role in γTuRC assembly or folding of γTuRC subunits, I depleted RUVBL1 in HeLa cells using RNAi. 72h after transfection of siRNAs against RUVBL1 I observed strongly reduced levels of RUVBL1 by Western Blotting (**Figure 9A,B**). In line with previous studies, depletion of RUVBL1 co-depleted RUVBL2 suggesting disruption of RUVBL. Interestingly, RUVBL-depleted extracts showed slightly reduced levels of γ-tubulin, GCP5 and GCP6 (**Figure 9A,C**), suggesting RUVBL may regulate overall levels of these subunits.

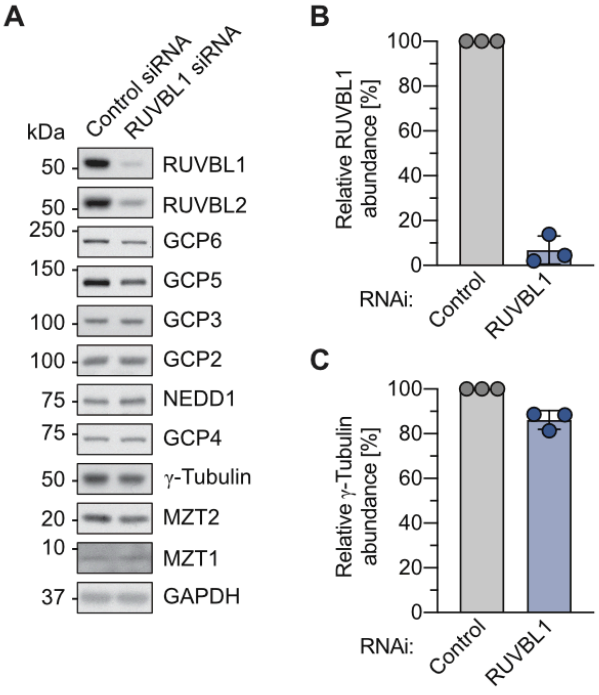

Figure 9: Disruption of the RUVBL1-RUVBL2 complex by RUVBL1 RNAi. (A) Extracts of HeLa cells treated with control and RUVBL1 siRNA were analyzed by Western blotting with the indicated antibodies. (B) RUVBL1 band intensities in control-and RUVBL-depleted extracts were quantified, normalized to the loading control (GAPDH), and plotted as percentage of control set to 100%. Bars indicate mean, error bars show SD; n=3 experiments. (C) γ-Tubulin co-depletion by RUVBL1 RNAi determined as in B. Bars indicate mean, error bars show SD; n=3 experiments.

To gain further insight into the integrity of γ-tubulin complexes in cells with reduced RUVBL levels, I performed sucrose gradient centrifugation and analyzed levels of γTuRC core subunits in each gradient fraction by Western Blotting. As expected, γTuRC subunits GCP2-6, MZT1-2, and γ-tubulin cosedimented in control-depleted extracts as a characteristic γTuRC peak with a size larger than 19S (**Figure 10A**, upper panel fractions

7-8). Albeit to a lesser extent, I also observed complexes containing γTuRC subunits in lower molecular weight fractions, most likely representing γTuSC and γTuSC-like complexes (**Figure 10A**, upper panel, fractions 3-6) (89, 108). Notably, RUVBL depletion

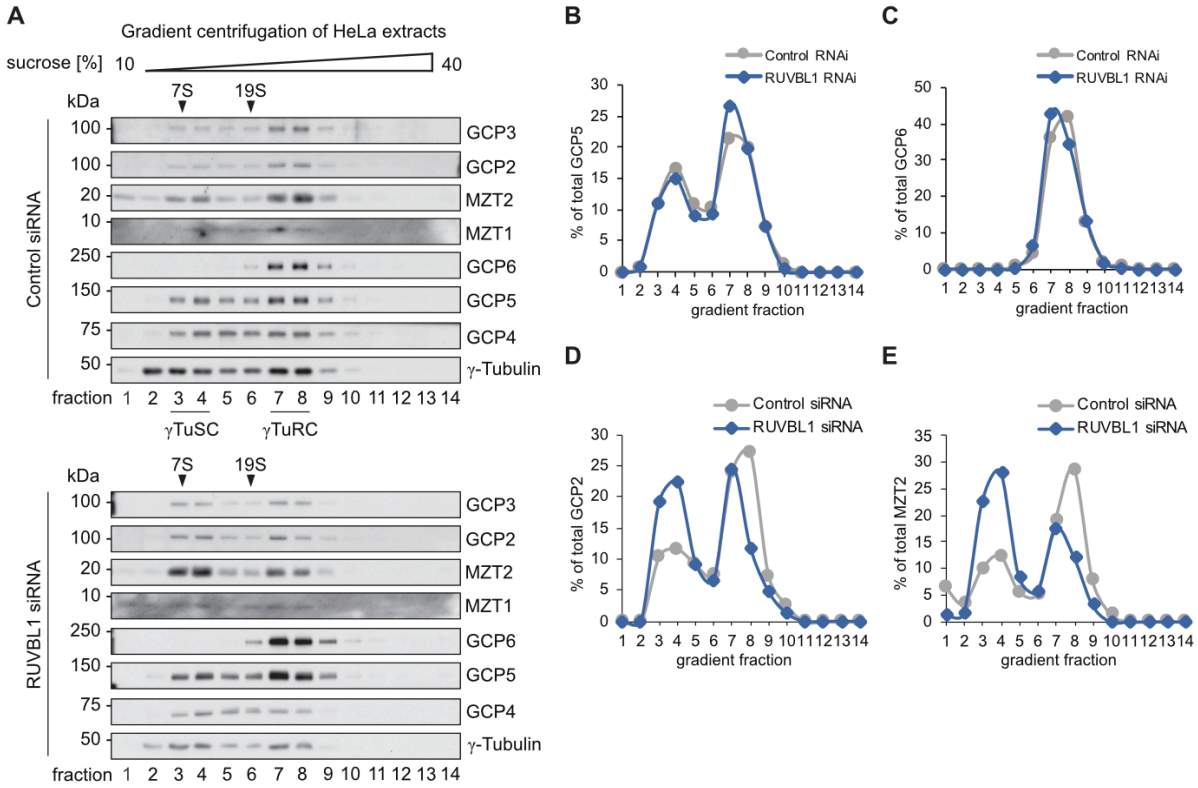

Figure 10: RUVBL-depleted cells have γTuRC integrity defects. (A) Extracts of HeLa cells treated with control and RUVBL1 siRNA were fractionated on sucrose gradients and analyzed by Western blotting. Aldolase (7S, 158 kDa) and thyroglobulin (19S, 669 kDa) served as standards. (B) Fractionation profiles of GCP5 in sucrose gradients shown in (A). Band intensities in fractions were quantified and plotted for control and RUVBL1-depleted extracts as indicated. Values are percentages of the sum of band intensities across all fractions. Fractionation profiles of GCP6 (C), GCP2 (D), and MZT2 (E) in sucrose gradients shown in (A) were determined as in (B). Data in (A) to (E) were reproduced in three independent experiments.

caused redistribution of some γTuRC subunits. Whereas the overall distribution of GCP4, GCP5 and GCP6 remained largely unchanged (**Figure 10A-C**), GCP2, GCP3 and MZT2 were shifted to lower molecular weight fractions. Under control conditions, the majority of GCP2 and GCP3 was present in fractions corresponding to γTuRC. In contrast, RUVBL-depletion caused an increase of GCP2 and GCP3 in fractions corresponding to γTuSC (**Figure 10A,D**). A similar redistribution was observed for MZT2, which is known to associate both with γTuSC and γTuRC, likely through binding to GCP2 (89, 109) (**Figure 10A,E**). Thus, RUVBL is required for γTuRC integrity and may be important to connect γTuSC and γTuSC-like complexes containing GCP4, GCP5 and GCP6.

4.2 RUVBL deficiency impairs assembly of centrosomal γTuRC.

Several studies have reported mitotic defects in human cell lines depleted of RUVBL (185, 212, 231). In line with this, I found that RUVBL-depletion similarly caused accumulation of mitotic cells with spindle- and chromosome congression defects (**Figure 11A,B**).

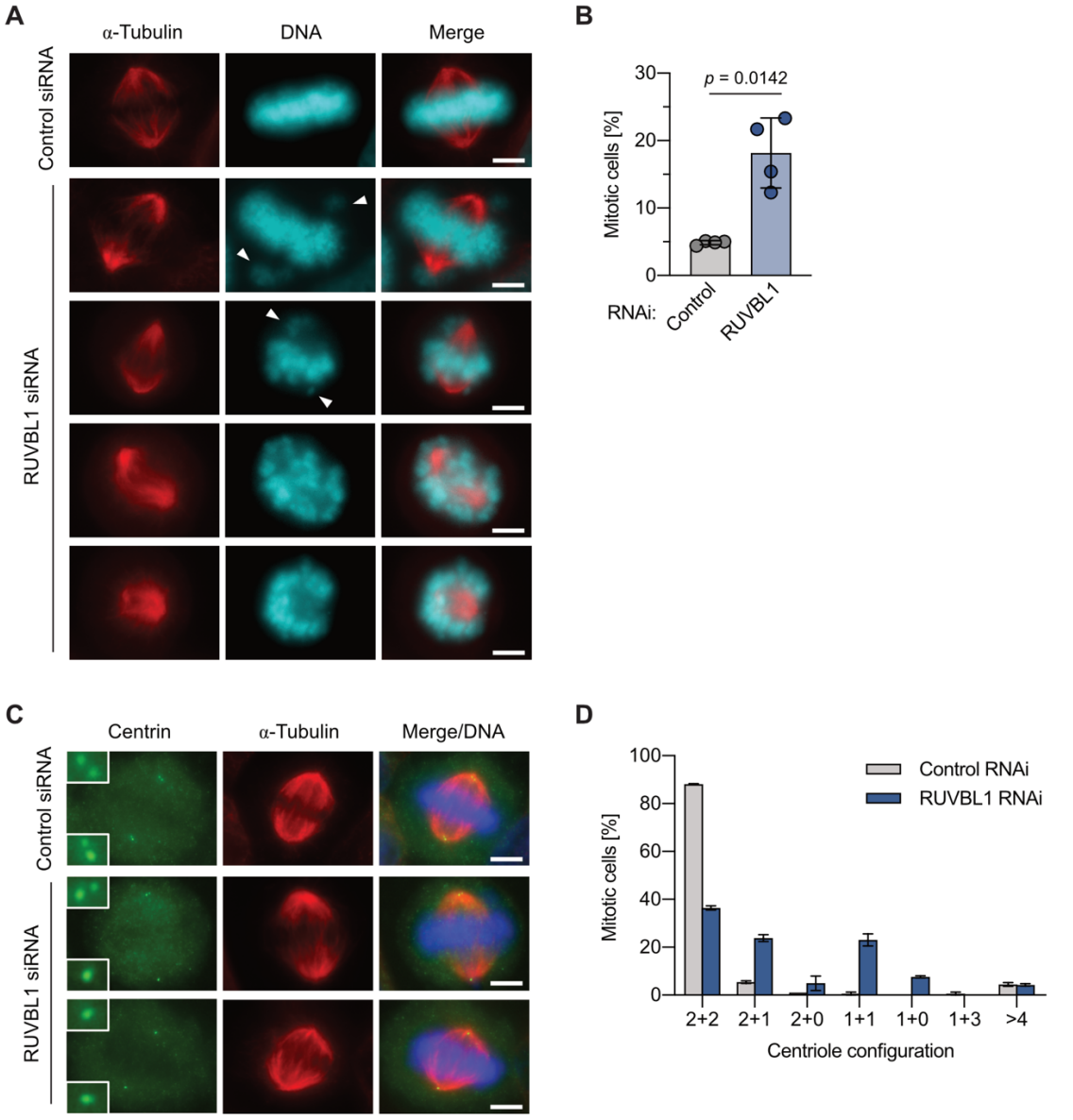

Figure 11: RUVBL depletion causes mitotic defects. (A) Immunofluorescence microscopy of HeLa cells depleted as in Figure 9A after staining with anti-PCNT, anti-α-tubulin antibodies, and DAPI to label DNA. White arrowheads indicate lagging chromosomes. Scale bar: 5 µm. (B) Percentage of mitotic HeLa cells stained as in A. Bars indicate mean, error bars show SD; n=4 experiments, 499-734 cells per condition; P=0.0142 (two-tailed, unpaired t-test with Welch's correction). (C) Mitotic HeLa cells after staining with anti-centrin and anti-α-tubulin antibodies, and DAPI to stain DNA. Scale bar: 5 µm, inset is 5-fold magnified. (D) Configuration of centrin foci in cells as in L. Values are percentages of total cell number. Bars indicate mean, error bars show SD; n=2 experiments, 100-127 mitotic cells per condition.

When I scored these cells for centrin-foci as a read-out for centriole number, I found severe centriole duplication defects. While ~90% of control-depleted cells showed two centrin foci at each spindle pole (2+2 configuration) as expected, this configuration was observed in only ~35% of RUVBL-depleted cells. Here, most cells lacked one or more centrin foci (**Figure 11C,D**). Thus, apart from mitotic spindle assembly, RUVBL is required for centriole duplication. Notably, these two processes also require γTuRC (113, 128, 232). As I previously observed altered γTuRC subunit composition upon RUVBL-depletion I next asked whether this affects γTuRC localization at MTOCs. To test this, I measured centrosomal MZT2 levels in control- and RUVBL depleted cells and compared it to levels of NEDD1, which is known to localize to centrosomes independently of γTuRC (127, 128). Indeed, interphase centrosomes showed a specific reduction in MZT2 levels in RUVBL-depleted cells while NEDD1 levels stayed constant (**Figure 12**). Thus, RUVBL controls the correct assembly of γTuRC at MTOCs.

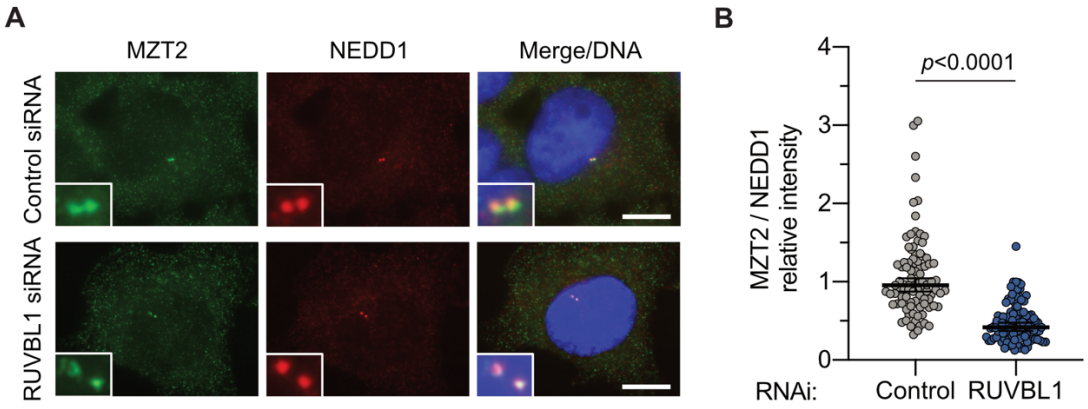

Figure 12: RUVBL depletion alters γTuRC subunit composition at MTOCs. (A) Immunofluorescence microscopy of control and RUVBL-depleted HeLa cells after staining with anti-MZT2 and anti-NEDD1 antibodies and DAPI to stain DNA. Inset is fivefold magnified. Scale bars, 10 µm. (B) Fluorescence intensities for centrosomal MZT2 and NEDD1 staining as in (A) were quantified and plotted. Intensities were normalized to controls and plotted as fraction of MZT2 relative to NEDD1; n=92 to 109 centrosomes per condition combined from two independent experiments. Bars indicate median with 95% confidence interval; P<0.0001 (unpaired, two-tailed Mann-Whitney U test).

4.3 MZT1 and MZT2 are required for reconstitution of human γTuSC

Having identified RUVBL as a novel factor that regulates γTuRC in human cells, possibly by promoting the incorporation of γTuSC and MZT2 into γTuRC, I hypothesized that RUVBL directly assembles γTuRC. To test this hypothesis, I sought to reconstitute this process *in vitro* with recombinant components. By combining knowledge from previous reconstitutions of non-animal γTuSC (124, 125) with recently developed baculovirus-based

expression vectors, I established a versatile coexpression system for human γTuRC subunits based on biGBac (210, 211) (see Materials and Methods section for details). With this system at hand, I followed a bottom-up approach and first attempted to reconstitute human γTuSC. After expressing distinct subunit combinations in Sf9 cells using single baculovirus constructs in each case, I affinity-purified the proteins using a 3C-protease cleavable TwinStrep-tag on GCP3 ($GCP3^{3C\text{-}TwinStrep}$). While SDS-PAGE analysis of Sf9 cells revealed robust expression of GCP2, GCP3 and γ-tubulin, only negligibly amounts of protein, if any, could be purified (**Figure 13A**). This hardly improved with additional expression of either MZT1 or MZT2. Strikingly, expression of all five subunits significantly boosted solubility and yield of a complex containing all coexpressed subunits. Notably, the subunit stoichiometry of γ-tubulin, GCP2 and GCP3 was highly reminiscent of budding yeast and fruit fly γTuSC as judged by Coomassie staining (Gunawardane.2000, Vinh.2002). When I further analysed the purified complex by sucrose gradient centrifugation, I observed that it migrated around 7S, similar to γTuSC in cell extracts (**Figure 13B**, compare to **Figure 10B**). To gain structural insight, Marina Serna (Oscar Llorca group, CNIO, Madrid) analysed the purified complex by negative stain electron microscopy (negative stain-EM). Negative stain-EM micrographs revealed V-shaped particles that resembled the characteristic shape of budding yeast γTuSC (233) (**Figure 13C**). This indicates that the overall structure of γTuSC is conserved. Most particles were found to be single γTuSCs but some were found to be two laterally associated γTuSCs as it would be expected for their configuration in γTuRC. Taken together, these data define γ-tubulin, GCP2, GCP3, MZT1 and MZT2 as the minimal set of proteins required for efficient reconstitution of human γTuSC and suggests that MZT1 and MZT2 solubilize GCP3 and GCP2, respectively.

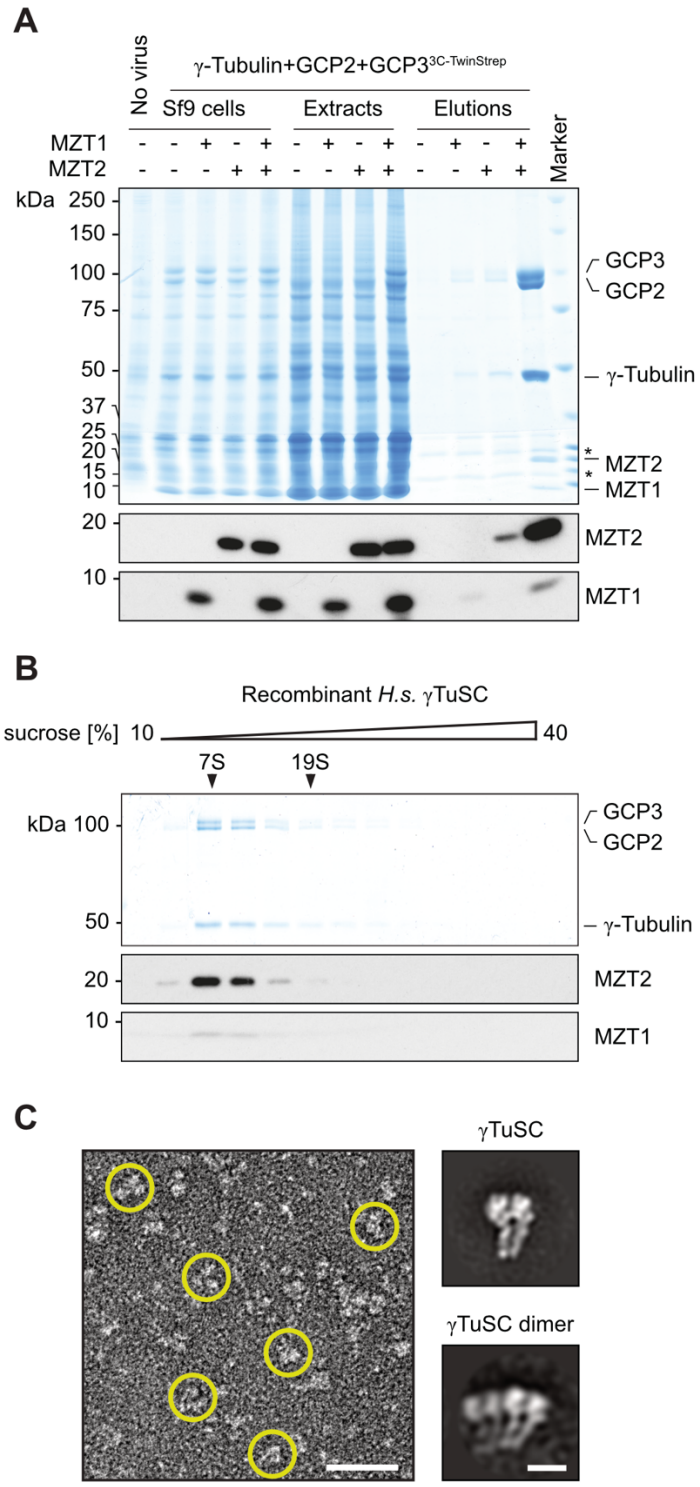

Figure 13: MZT1 and MZT2 are required for reconstitution of human γTuSC. (A) Combinations of the indicated proteins were coexpressed, affinity-purified, and analyzed by SDS–PAGE. MZT1 and MZT2 were detected by Western blotting. Asterisks indicate contaminating Strep-Tactin (15 kDa) used for affinity purification and 3C protease (25 kDa) used for elution (B) Recombinant Homo sapiens (*H.s.*) γTuSC was fractionated on a sucrose gradient and analyzed as in A. (C) Negative-stain EM of purified γTuSC reveals Y-shaped particles (yellow circles) (left). Scale bar, 50 nm. Two-dimensional (2D) averages of γTuSC (4489 particles) (top right) and two laterally associated γTuSCs (344 particles) (bottom right). Scale bar, 10 nm. Subfigure C was contributed by Marina Serna.

4.4 MZT1 and MZT2 form distinct units with the NTEs of GCP3 and GCP2

Considering that MZT1 and MZT2 are not present in budding yeast and thus not required for reconstituting γTuSC of this organism (125), I aimed to understand their interactions within γTuSC in more detail. For MZT1, our lab and others had previously identified a conserved binding site in the NTE of GCP3 (113, 135, 136). Artur Ezquerra in our group conducted a similar analysis for MZT2. He transfected HEK293T cells with EGFP-tagged MZT2 and FLAG-tagged N-terminal halves (Nt) of GCP2-6. FLAG-IP followed by Western Blotting revealed that MZT2 binds to GCP2$^{1\text{-}506}$ but not corresponding fragments of GCP3-6 (**Figure 14A**). Testing of additional fragments mapped the MZT2 binding region in GCP2 to the N-terminal 125 amino acids. Thus, similarly to MZT1 binding to the NTE of GCP3, MZT2 binds to the NTE of GCP2.

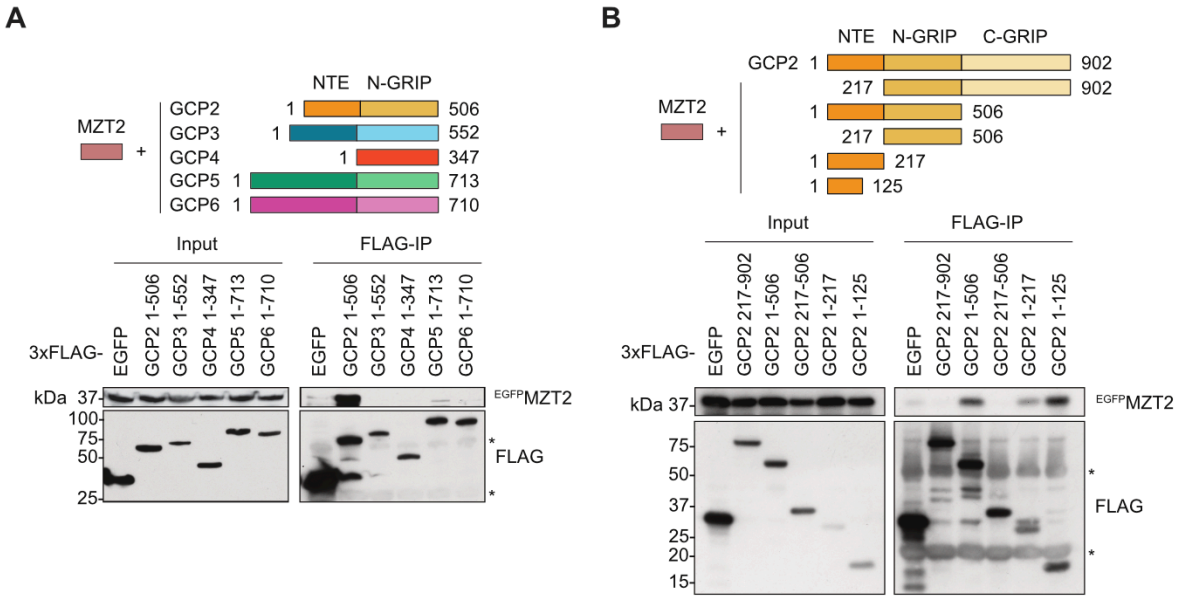

Figure 14: The NTE of GCP2 contains a MZT2 binding site. (A) 3xFLAG-tagged Nt-GCP2-6 were coexpressed with EGFP–MZT2, immunoprecipitated (IP), and probed by Western blotting as indicated. Asterisks indicate contaminating IgG. (B) 3xFLAG-tagged GCP2 fragments were coexpressed with EGFP-MZT2 and analyzed as in (D). Asterisks indicate contaminating IgG. Raw data contributed by Artur Ezquerra.

To gain insights into the interactions between γTuSC subunits on an amino acid level, I analysed purified recombinant γTuSC by cross-linking mass spectrometry (CL-MS). To do this, I incubated equal amounts of γTuSC with increasing concentrations of DSBU (234), a bifunctional cross-linker that mainly reacts with lysine, but to a lesser extent also with serine, threonine, tyrosine, and N-terminal amines. SDS-PAGE of cross-linking reactions revealed that γTuSC subunits were covalently linked only when DSBU was

added, as observed by high molecular weight adducts in a concentration dependent manner (**Figure 15A**). Notably, these adducts migrated more slowly than expected for a single, cross-linked γTuSC of ~330 kDa. This would be consistent with lateral association and crosslinking of multiple γTuSCs as seen in negative stain-EM (**Figure 13C**). Next, samples were analysed by the IRB Barcelona Mass Spectrometry Facility, which resulted in a cross-link network map of γTuSC (**Figure 15B**). In agreement with the previously reported interaction of MZT1 and the NTE of GCP3 (hereafter termed MZT1:3NTE) I found cross-links between MZT1 and this region, but not with the NTE of GCP2 (**Figure 15C**, black lines). Both subunits of MZT1:3NTE also showed cross-links with more central residues of the GCP2 and GCP3 core fold, suggesting they occupy similar space and behave as a unit (**Figure 15C**, light and dark blue lines). Verifying the interaction found by IP, MZT2 was cross-linked to the NTE of GCP2 (hereafter termed MZT2:2NTE), but not with the NTE of GCP3 (**Figure 15C**, black lines). As observed for the MZT1:3NTE, MZT2:2NTE was cross-linked to more central parts of GCP2 and GCP3 (**Figure 15C**, red and orange lines). However, the central residues were distinct for MZT1:3NTE and MZT2:2NTE. Together, these data suggest that the NTEs of GCP2 and GCP3 within γTuSC associate with MZT2 and MZT1, respectively, and form distinct spatial units that are able to 'fold back' onto more centrally localized regions of the GCP2/3 core structure.

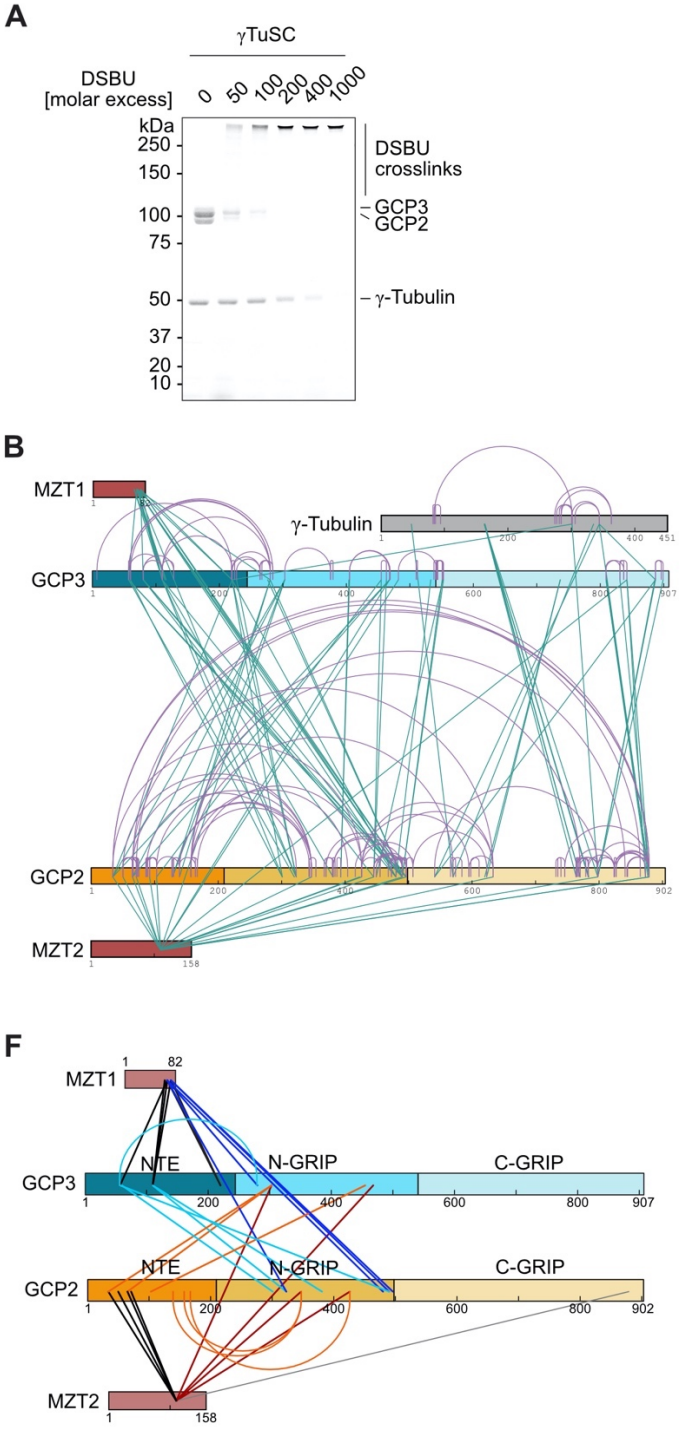

Figure 15: Characterization of recombinant γTuSC by chemical crosslinking and CL-MS. (A) Recombinant γTuSC was crosslinked in vitro using increasing concentrations of DSBU and analyzed by SDS-PAGE. Proteins with tryptophan residues were visualized by stain-free imaging. (B) Network map representation of CL-MS analysis of γTuSC displaying all identified crosslinks. Inter-subunit crosslinks are shown in cyan and intra-subunit crosslinks in purple. (C) Cross-links of MZT1, MZT2, or the NTEs with other regions identified at least twice. MZT1 and GCP3-NTE were cross-linked with each other (black lines) and with the N-GRIP domains of GCP2 and GCP3 (light and dark blue lines). MZT2 and GCP2-NTE were cross-linked with each other (black lines) and with the N-GRIP domains of GCP2 and GCP3 (orange and red lines). A cross-link between MZT2 and a C-terminal loop of GCP2 is shown in gray.

4.5 Increased GCP NTE levels are counterbalanced by MZT proteins

Intrigued by the strong interdependency of MZT:NTE units in the heterologous expression system, I asked whether similar coregulation exists in their native cellular environment. To test this, I transfected plasmids encoding single FLAG-tagged GCP2-6 in HEK293 cells and analysed cell extracts 24h after transfection. Western Blotting confirmed ectopic expression of FLAG-tagged GCP2-6, and moreover revealed elevated MZT1 levels in cells transfected with GCP3, GCP5, and GCP6 but not GCP2 (**Figure 16A**). Thus, cells respond to elevated levels of MZT1-binding GCPs (113, 135) by increasing MZT1 levels. My γTuSC reconstitution together with previous studies (113, 135, 142) showed that MZT1 and MZT2 bind to the NTE of GCP3 and GCP2, respectively. To test whether coregulation of MZT proteins and MZT-binding GCPs depends on the NTE, I expressed FLAG-tagged Nt-GCP2-6 and the corresponding Nt lacking the NTE (Nt ΔNTE). Western Blotting of cell extracts showed elevated MZT2 levels for Nt-GCP2 and higher MZT1 levels for Nt-GCP3, GCP5, and GCP6, whereas levels were normal for Nt-GCP4 (**Figure 16B**). This effect was abolished in the Nt ΔNTE constructs, which lacked the MZT-binding NTE. Thus, increased levels of GCP NTEs correlates with an upregulation of their respective MZT protein binding partner in human cells.

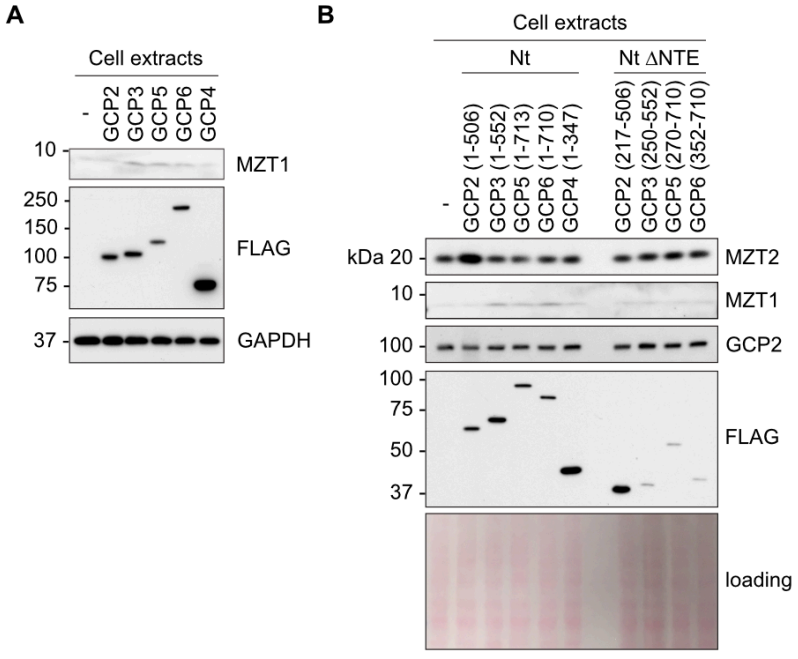

Figure 16: Overexpression of GCP NTEs correlates with upregulation of MZT proteins. (A) 3xFLAG-tagged GCP2-6 were expressed in HEK293T cells and extracts were analyzed by Western Blotting with the indicated antibodies. (B) 3xFLAG-tagged Nt-GCP2-6 and Nt ΔNTE-GCP2, GCP3, GCP5, and GCP6 were expressed as in (A) and analyzed by Western Blotting with the indicated antibodies. Ponceau S staining before antibody probing was used as loading control.

4.6 RUVBL associates with γTuSC

Given that RUVBL-depletion compromised γTuRC integrity in HeLa cells, I next used the recombinant insect cell expression system to investigate if RUVBL had an effect on γTuSC biogenesis. To do this, I generated a single baculovirus for coexpression of all five γTuSC subunits and additionally RUVBL1 and RUVBL2 and purified γTuSC as before using a TwinStrep-tag on GCP3. RUVBL1-RUVBL2 coexpression did not change the overall yield of γTuSC, but instead copurified with it (**Figure 17A**).

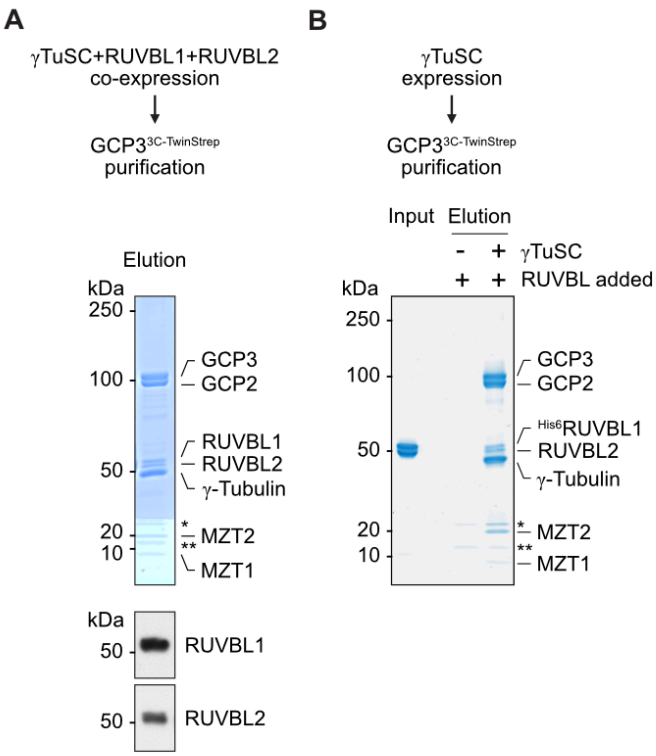

Figure 17: RUVBL1-RUVBL2 can directly bind to γTuSC. (A) γTuSC, coexpressed with RUVBL1-RUVBL2, was purified and analyzed by SDS-PAGE and Coomassie staining, as well as Western Blotting with the indicated antibodies. (B) Purified, immobilized γTuSC was incubated with recombinant RUVBL1-RUVBL2 before elution and analysis as in (A). Asterisks denote contaminants as in Figure 13A.

The presence of equal amounts of RUVBL1 and RUVBL2 suggested copurification of RUVBL complex, however, RUVBL did not appear to bind γTuSC stoichiometrically. To exclude that the γTuSC-RUVBL interaction depends on additional factors in the insect cell expression host, I asked whether this interaction can be reconstituted from separately purified complexes. Using an *in vitro* pulldown-assay, I observed that, similar to coexpression, purified RUVBL was specifically retained on γTuSC-bound resin but not on control-treated resin (Figure 14B). These results show that RUVBL directly binds γTuSC.

Next, Marina Serna (Oscar Llorca group, CNIO, Madrid) visualized γTuSC-RUVBL complexes using negative stain-EM. To enable image processing the complex had to be stabilized by mild crosslinking with glutaraldehyde (GA). In the absence of RUVBL, we observed curved γTuSC oligomers and γTuRC-like rings (**Figure 18A**). These assemblies were more extensive than observed for γTuSC in the absence of cross-linker suggesting that consecutive lateral binding events had been trapped by the cross-linker. We then repeated the mild cross-linking in the presence of RUVBL and additionally used the His-tag on RUVBL to enrich for RUVBL-bound γTuSC. Negative stain-EM with subsequent 2D-avaraging revealed a doughnut-shaped density near the seam of the γTuSC-ring (**Figure 18B**). A 3D reconstruction resulted in a ~26 Å resolution map where the doughnut-shaped density could accommodate a RUVBL-hexamer filtered to low resolution (**Figure 18C,D**). Together, we found that under these conditions a RUVBL-hexamer is associated with the seam region of a γTuSC-ring.

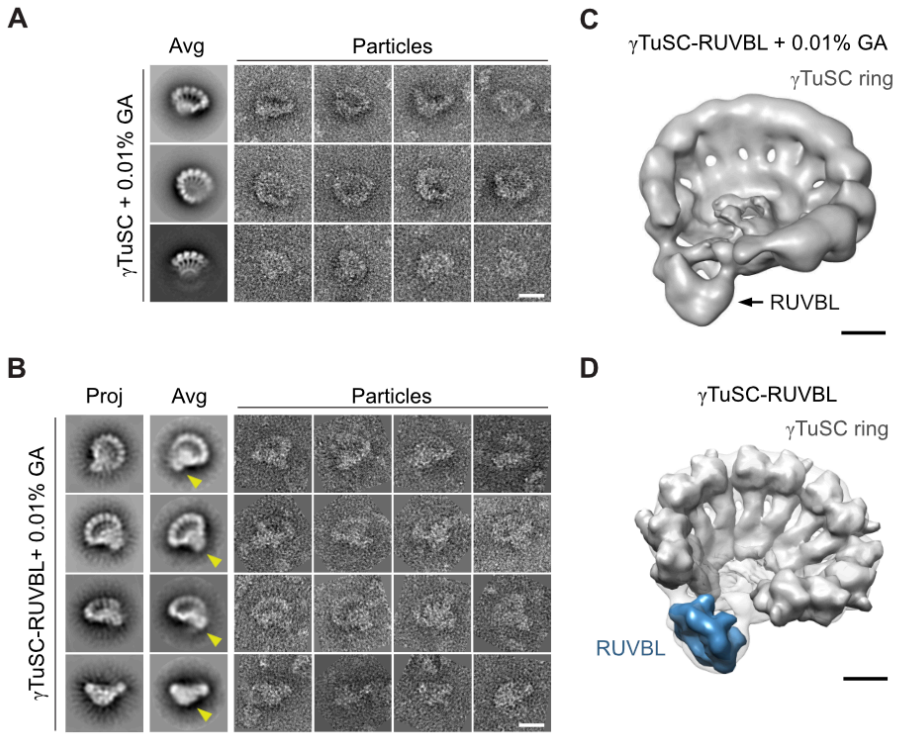

Figure 18: RUVBL binds to a defined region in γTuSC. (A) Negative-stain EM of ring-shaped γTuSC oligomers after cross-linking with 0.01% glutaraldehyde (GA). 2D averages (Avg) correspond to 1667, 1809, and 2002 particles from top to bottom. Representative particles are shown. Scale bar, 20 nm. (B) Negative-stain EM of reconstituted γTuSC-RUVBL complex purified after cross-linking reveals a globular density (yellow arrowheads) bound to γTuSC rings. 2D averages correspond to 213, 397, 214, and 227 particles from top to bottom and are compared to projections (proj) of the EM volume in A. Scale bar, 20 nm. (C) View of negative-stain structure of γTuSC-RUVBL (~26 Å resolution). Scale bar, 5 nm. (D) Structure of γTuSC-RUVBL (transparent) fitted with structures of γTuSC and RUVBL1-RUVBL2 hexamer [PDB 2XSZ] filtered at low resolution. Scale bar, 5 nm. Data contributed by Marina Serna.

The low resolution of the negative-stain EM analysis did not allow analysis of the γTuSC-RUVBL interaction at the molecular level. To gain insight into structural determinants of this interaction, I mixed purified RUVBL with γTuSC and performed DSBU cross-linking with subsequent CL-MS analysis as done before for γTuSC alone. The analysis revealed cross-linked residues within and between RUVBL1 and RUVBL2 (**Figure 19A**, purple and green lines), γTuSC subunits (**Figure 19A**, black lines), and between RUVBL2 and GCP2 and GCP3 (**Figure 19A**, red lines). Examination of γTuSC cross-links revealed high similarity to CL-MS data obtained for γTuSC alone (data not shown). For RUVBL cross-links, I made use of available crystal structures and mapped cross-links onto a RUVBL1-RUVBL2 hexamer. While not all cross-linked residues were resolved in the X-ray structures, all intra-RUVBL1, intra-RUVBL2, and RUVBL1-RUVBL2 cross-links that could be mapped satisfied the cross-linker constraints, suggesting the RUVBL1-RUVBL2 hexamer core was preserved throughout the cross-linking procedure (**Figure 19B**). Together, both complexes maintained their overall structure upon interaction, which is consistent with the negative-stain EM images, where we observed γTuSC-rings with a RUVBL hexamer attached (**Figure 18B-D**).

Next, I examined cross-links between RUVBL and γTuSC and found that RUVBL exclusively cross-linked to γTuSC through the RUVBL2 subunit (**Figure 19A**). Close examination of the GCP2-RUVBL2 cross-link revealed that RUVBL2$_{K177}$ is in the RUVBL2 DII domain, which extends to the periphery of to the hexameric core and has previously been implicated in substrate binding (**Figure 19C**, red spheres) (206, 208). The other RUVBL2 residues that formed cross-links were RUVBL2$_{M1}$ and RUVBL2$_{K83}$, which cross-linked to GCP2$_{T334}$ and GCP3$_{K533}$, respectively. Whereas RUVBL2$_{M1}$ is located in the unstructured N-terminus not resolved in available structures, RUVBL2$_{K83}$ is part of the nucleotide-binding pocket. Previous studies suggested that the flexible N-terminus localizes to the nucleotide-binding pocket, where it is released upon substrate binding. Substrate binding can lead to opening of the nucleotide-binding pocket to release ATP, resulting in an empty pocket (208) where residues may become available for forming crosslinks. Mapping of the crosslinked γTuSC residues revealed that RUVBL2 crosslinks to the N-GRIP domain of GCP2 (RUVBL2$_{M1}$-GCP2$_{T334}$ crosslink) and to the GCP2 kink between N- and C-GRIP (RUVBL2$_{K177}$-GCP2$_{T507}$ crosslink) (**Figure 19D**). Additionally, RUVBL2$_{K83}$ crosslinked to the GCP3 C-GRIP via GCP3$_{K533}$ (**Figure 19E**). Together,

CL-MS analysis of γTuSC-RUVBL suggests that several regions of RUVBL2 may directly interact with the GCP core folds of γTuSC.

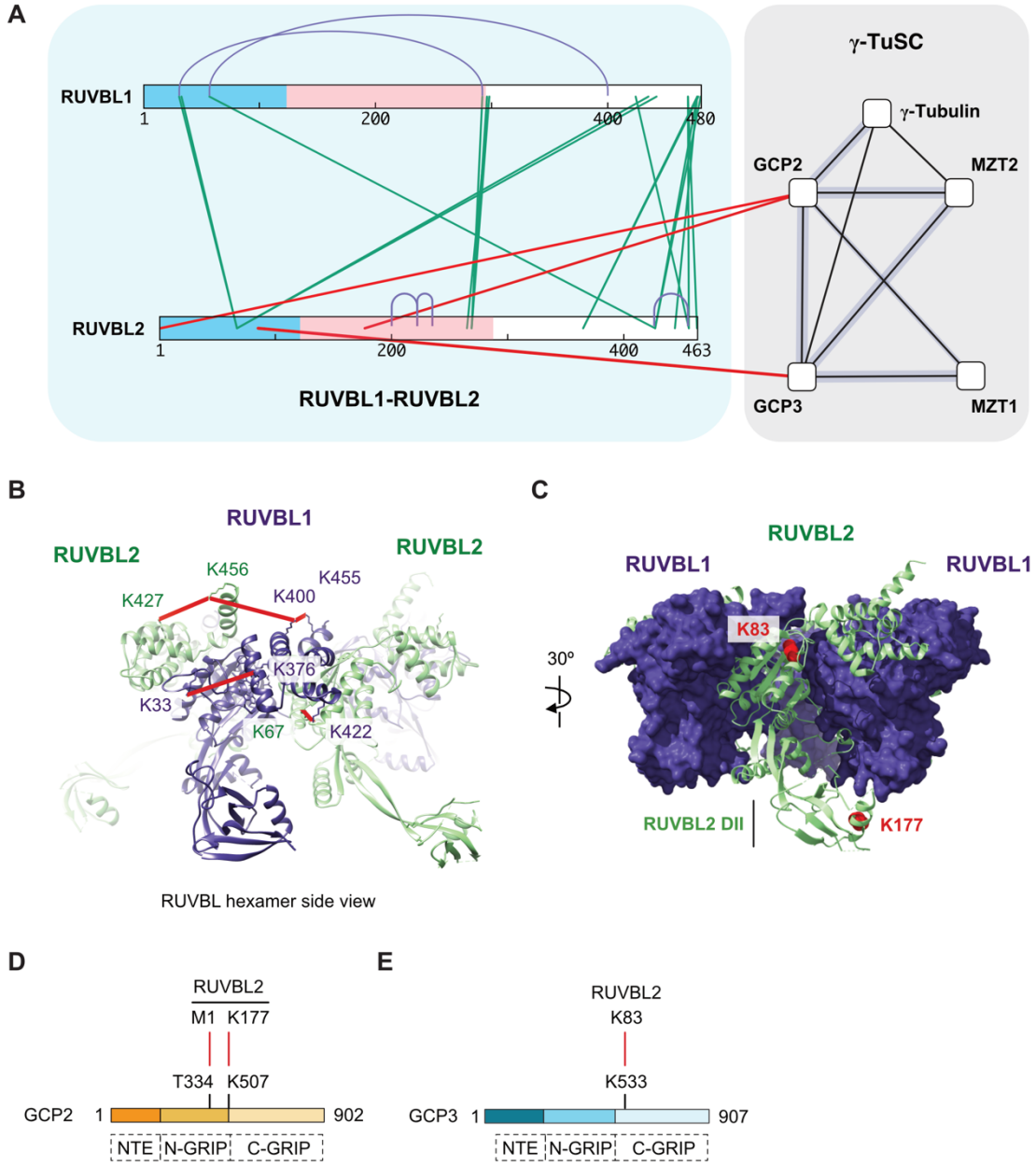

Figure 19: Characterization of the γTuSC-RUVBL complex by CL-MS. (A) Network map representation of detected cross-links of CL/MS analysis of γTuSC:^{His8}RUVBL1-RUVBL2 mix (molar ratio 8:1) after *in vitro* cross-linking with DSBU. Intra-RUVBL1 and intra-RUVBL2 crosslinks detected ≥2 times are shown in purple, RUVBL1-RUVBL2 cross-links in green, and RUVBL-γTuSC cross-links in red. Cross-links within γTuSC as black lines, and shaded black lines if >1 residues between subunits were cross-linked. (B) Side-view of a RUVBL1-RUVBL2 hexamer as in Figure 7 with identified intra- and inter-RUVBL1/2 crosslinks (red lines): Intra-RUVBL1 K_{427}-K_{455}; intra-RUVBL2 K_{400}-K_{456} and K_{33}-K_{376}; $RUVBL1_{K455}$-$RUVBL2_{K400}$ and $RUVBL1_{K67}$-$RUVBL2_{K422}$, spaced by 19 Å, 12 Å, 20 Å, 24 Å, 6 Å, respectively. (C) RUVBL2 residues crosslinked to γTuSC are highlighted as red spheres in a RUVBL1-RUVBL2 hexamer generated by docking of RUVBL2 (green, 6H7X) into heterohexameric RUVBL1-RUVBL2 (2XSZ) using ChimeraX. (D) $RUVBL2_{M1}$ crosslinks to $GCP2_{T334}$ and $RUVBL2_{K177}$ crosslinks to $GCP2_{K507}$. (E) $RUVBL2_{K83}$ crosslinks to $GCP3_{K533}$. Crosslinks in D and E are indicated as red lines.

4.7 RUVBL can interact with GCP4, GCP5 and GCP6

Previous studies suggested that other γTuRC subcomplexes may exist besides the relatively well-characterized γTuSC. These may be γTuSC-like combinations of GCP4/GCP5 and GCP4/GCP6 (116), or a larger GCP4/GCP5/GCP6 complex (130). To test whether RUVBL may additionally interact with the remaining GCPs, I transfected HEK293T cells with FLAG-tagged GCP4, GCP5, and GCP6. FLAG-IP followed by Western Blotting identified that endogenous RUVBL2 coimmunoprecipitates with GCP2-6 (**Figure 20**).

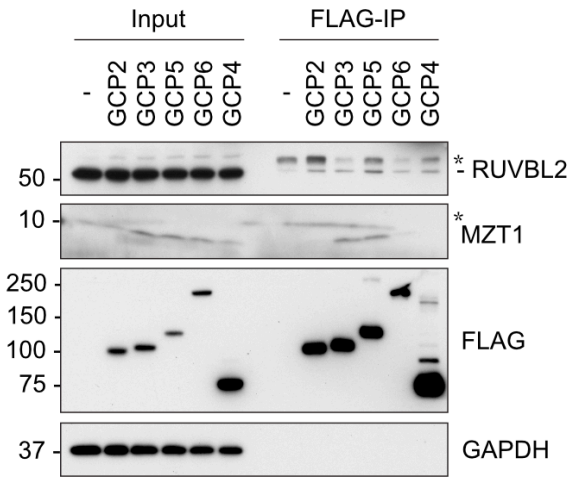

Figure 20: RUVBL interacts with GCP2-6 in human cells. 3xFLAG-tagged GCP2-6 were expressed in HEK293T cells, immunoprecipitated (IP), and probed by Western blotting as indicated. Cell extract (input) samples are the same as in Figure 16A, as same experiment allowed several observations. Asterisk indicates unspecific signals.

4.8 RUVBL reconstitutes recombinant γTuRC

Next, I asked if RUVBL participates in assembly of γTuRC. For this, I first tested if coexpression of γTuSC subunits together with GCP4, GCP5 and GCP6 alone was sufficient to reconstitute γTuRC. I combined expression of γ-tubulin, GCP2, GCP3^{His6}, MZT1, MZT2, GCP4, GCP5 and GCP6 and moved the 3C-cleaveable TwinStrep-tag to the GCP6 C-terminus to allow a more specific purification of γTuRC. All subunits were robustly expressed and could be copurified with GCP6 to reasonable purity but low yield (**Figure 21A,B**). However, sucrose gradient centrifugation of this sample failed to detect a defined complex. γ-Tubulin was evenly spread over all fractions and detection of the other subunits was poor (**Figure 21C**).

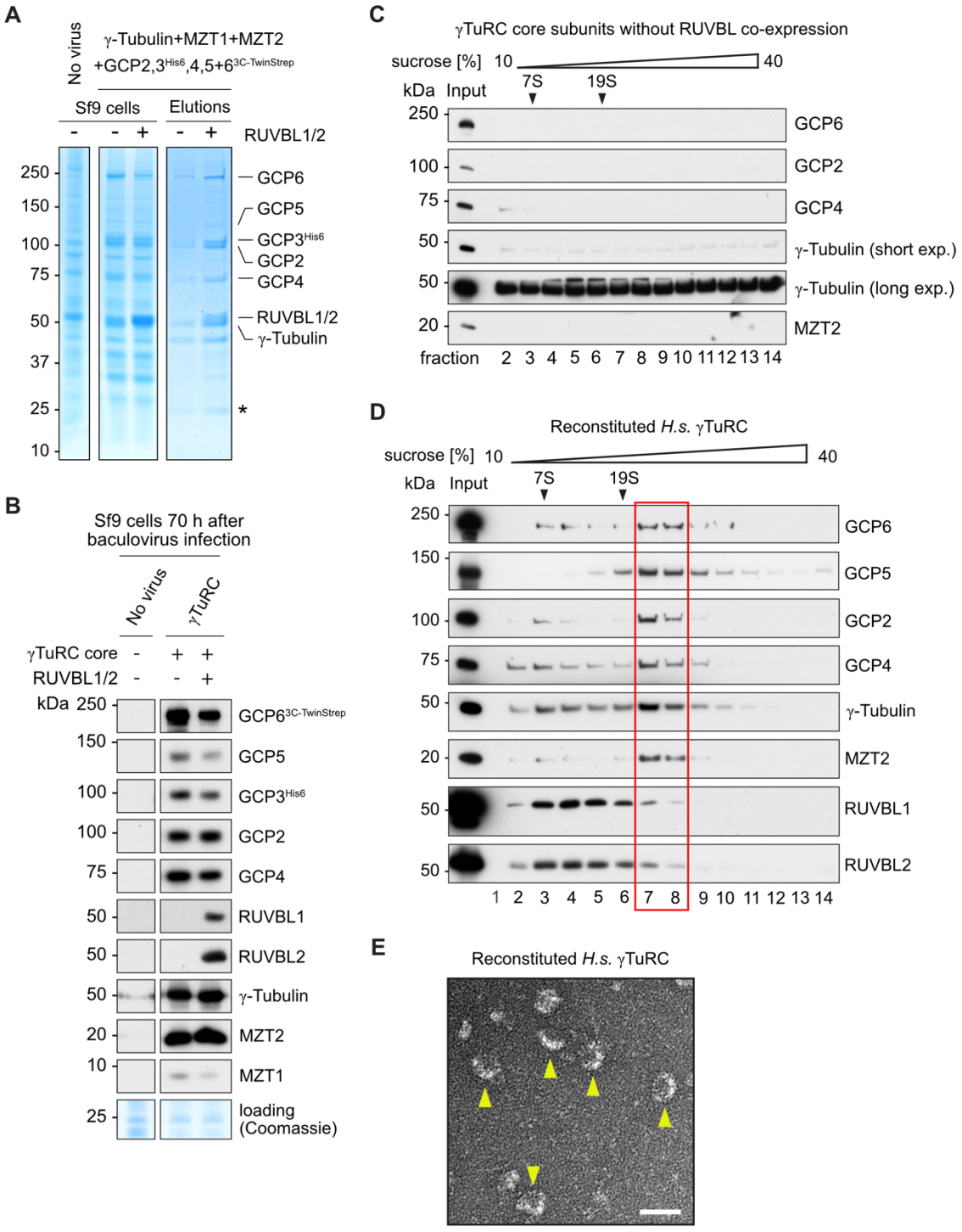

Figure 21: RUVBL1-RUVBL2 is required for reconstitution of human γTuRC. (A) γTuRC subunits coexpressed in Sf9 cells with or without RUVBL1-RUVBL2, affinity-purified, and analyzed by SDS-PAGE. (B) Overall expression levels of γTuRC subunits. After infection with single baculoviruses with the indicated subunit combination, Sf9 cells were analysed by Western Blotting with indicated antibodies. (C) γTuSC ($GCP3^{His6}$) co-expressed with GCP4, GCP5, and $GCP6^{3C\text{-}TwinStrep}$ in Sf9 cells, affinity-purified, fractionated by sucrose gradient centrifugation and analyzed by Western Blotting with indicated antibodies. (D) Sucrose gradient analysis of recombinant γTuRC, probed by Western blotting as indicated. Red box marks γTuRC peak fractions (compare to Figure 10A). (E) Negative-stain EM of purified recombinant H.s. γTuRC. Yellow arrowheads denote ring-shaped particles with 25-30 nm diameter. Scale bar: 50 nm. Subfigure E contributed by Marina Serna.

Thus, while coexpression of γTuRC subunits enables their copurification, they fail to assemble γTuRC. I then repeated the experiment by infecting insect cells with a single baculovirus clone coexpressing all γTuRC subunits together with RUVBL1-RUVBL2. Whereas overall expression levels of γTuRC subunits were similar, the yield of purified subunits was significantly boosted, suggesting RUVBL promoted their solubility (**Figure 21A,B**). Strikingly, fractionation on sucrose gradients revealed a defined peak of γTuRC subunits in the same fractions as native γTuRC in cell extracts, consistent with a size of ~2 mDa (**Figure 21D**). In agreement with a catalytic role of RUVBL in γTuRC assembly, the bulk of copurifying RUVBL1-RUVBL2 did not cofractionate with γTuRC but was present in smaller molecular weight fractions. Negative-stain EM of the purified material done by Marina Serna (Oscar Llorca group, CNIO, Madrid) revealed ring-shaped complexes confirming successful reconstitution of γTuRC (**Figure 21E**). To test whether recombinant γTuRC has nucleation activity, I incubated recombinant γTuRC with pure tubulin spiked with fluorescently labelled tubulin in the presence of GTP. Aliquots of the reaction were taken at different time points, fixed with glutaraldehyde, spotted on glass slides and imaged by fluorescence microscopy. At a concentration of 20 µM tubulin and 1 nM γTuRC we observed microtubule formation in a time dependent manner but not in a reaction with tubulin alone (**Figure 22**). I concluded that coexpression of γTuRC subunits together with RUVBL1-RUVBL2 in a heterologous insect cell expression system allows efficient reconstitution and provides a source for purified recombinant human γTuRC for *in vitro* microtubule nucleation studies.

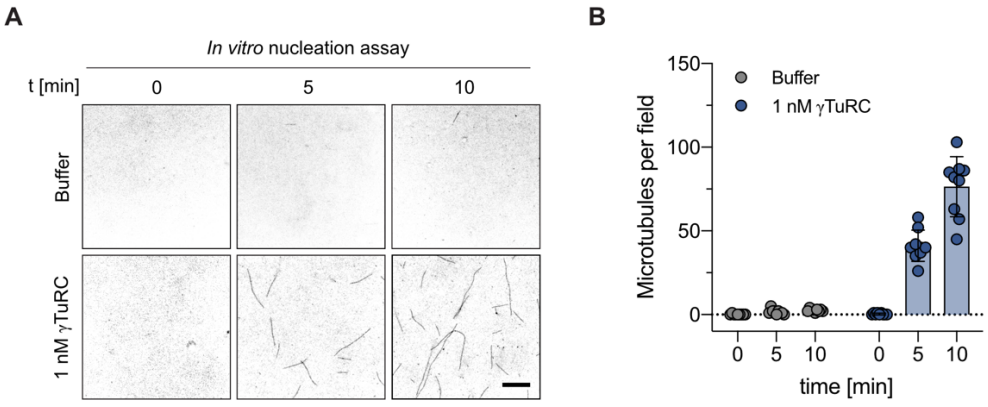

Figure 22: Recombinant γTuRC has microtubule nucleation activity. (A) Rhodamine-labeled microtubules nucleated by recombinant γTuRC were detected by fluorescence microscopy. Scale bar, 10 µm. (B) Quantification of microtubule number (per 137.06x104.84 µm microscope field) of nucleation assays in A. n=9 randomly chosen fields per condition, combined from three independent assays performed with γTuRC from independent preparations. Bars indicate mean, error bars show SD.

4.9 Recombinant γTuRC resembles native γTuRC

To gain insight into the molecular architecture of recombinant γTuRC we sought to determine a high-resolution structure by cryo-EM. At that time no structural information of vertebrate γTuRC was available. The affinity-purified γTuRC sample was vitrified using holey grids with a thin carbon film placed on top. Marina Serna (Oscar Llorca group, CNIO, Madrid) collected cryo-EM images on a 300-kV electron microscope and selected the best particles after several cycles of 2D and 3D classification and averaging (data not shown). The dataset contained views of the complex in several orientations (**Figure 23A**), sufficient to determine its 3D structure at an average resolution of 4.2 Å. In the course of determining the structure of recombinant γTuRC three independent studies reported structures and defined atomic models for native γTuRC (235–237). As our structure was largely identical, I will only provide a summary of the γTuRC core structure and then move on to describe

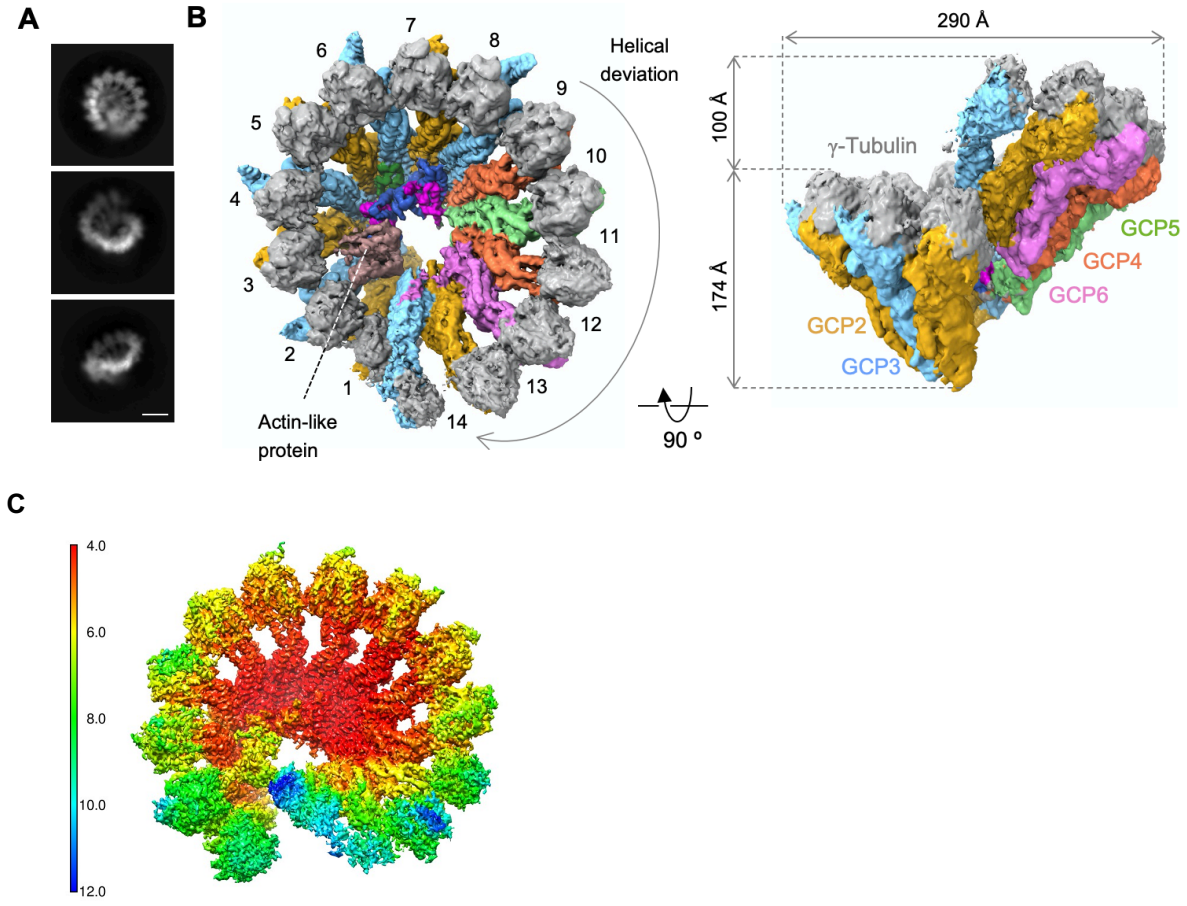

Figure 23: Cryo-EM structure of recombinant γTuRC. (A) Representative 2D averages obtained from the cryo-EM images of recombinant γTuRC. The averages show the asymmetric cone-shaped structure of γTuRC. Scale bar, 10 nm. (B) Top and side views of the cryo-EM map for recombinant γTuRC with color-coded subunits. (C) Local resolution map of the cryo-EM volume for recombinant γTuRC color-coded from 4 Å (red) to 12 Å (blue). Data contributed by Marina Serna.

regions where our resolution was sufficiently high to define novel structural features.

Recombinant γTuRC has the shape of a cone that is formed by 14 stalk-like units (**Figure 23B**). Each unit is composed of a GCP that is bound to one molecule of γ-tubulin through its C-terminal domain. Within the cone, GCPs are associated laterally mainly through their N-terminal domain, resulting in a roughly circular, helical assembly with 14 γ-tubulins presented at the open face of the cone. The GCP-γ-tubulin units at positions 9 to 14 deviate from the helical symmetry and display some degree of flexibility, reducing the resolution in this part, whereas the units at positions 1 to 8 are more rigid, resulting in significantly better resolution (**Figure 23C**). As in the native complex, an actin-like protein is present in the lumen of the cone, although the recombinant baculovirus did not contain a corresponding expression cassette (**Figure 23B**). Our collaborator Marina Serna identified GCP4, γ-tubulin, and the actin-like protein with the help of available crystal structures and the remaining GCPs by unique features in their sequences in regions of high resolution, without using structural information of the native complex (**Figure 23B**). As in native γTuRC, GCP2-GCP3 pairs occupy positions 1 to 8 and 13 to 14. The remaining positions are occupied by two γTuSC-like GCP pairs, a GCP4-GCP5 pair at positions 9/10 and a GCP4-GCP6 pair at positions 11/12 (**Figure 23B**).

In addition, several structural features were identified that are also present in native γTuRC. This includes groups of bundled helices bridging the γTuRC lumen, an extended helix-hairpin structure on the inside of the cone, a globular density laterally associated with the GCP3 at position 14, and pairs of short helices situated on the outside surface of γTuSCs. We compared the atomic models of reconstituted γTuRC with the highest resolution structure available of native human γTuRC (236) and quantified the root mean square deviation of the protein backbone for both models (**Figure 24A**). This revealed high resemblance of the reconstituted and native structures with minor differences in regions found in the reconstituted complex but unresolved in the native complex and vice versa (**Figure 24B-D**, see description below). Together, the results indicate that the presence of RUVBL1-RUVBL2 during recombinant expression promotes assembly of a complex that resembles native γTuRC and unequivocally identifies γ-tubulin, GCP2, GCP3, GCP4, GCP5, GCP6, MZT1, MZT2, and actin as the minimal set of proteins required to build the γTuRC core structure.

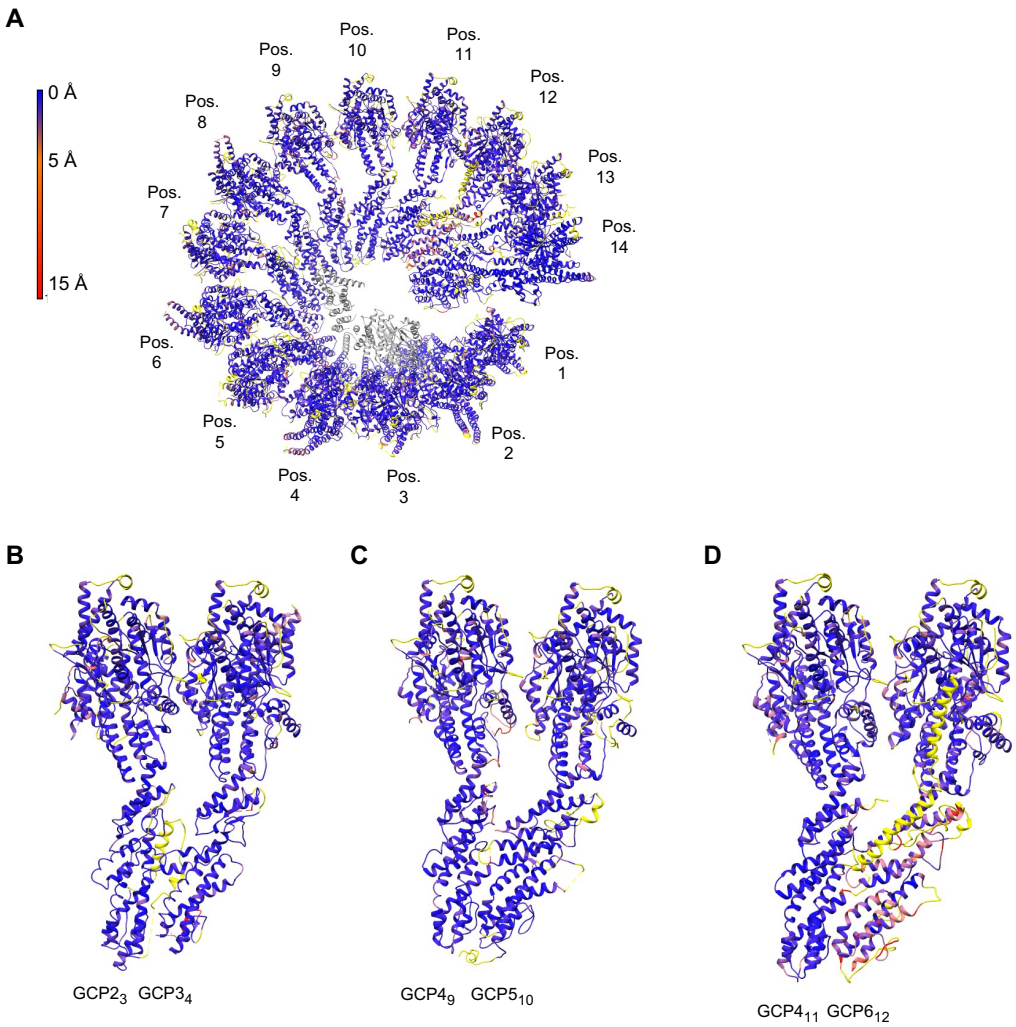

Figure 24: Recombinant γTuRC resembles native γTuRC. (A) Structural differences between the native and the recombinant human γTuRC (PDB 6V6S) models were estimated by calculating the RSMD of the two models color-coded from 0 Å (blue) to 15 Å (red). Structural elements present in the recombinant γTuRC model, but not in the native complex, are shown in yellow. The luminal bridge (grey) has been excluded from the analysis because its structure was not modelled in native γTuRC. The resemblance between both models is revealed by RMSD values <5 Å in large parts of the structure. (B-D) Apart from newly modelled residues such as the staples and insertion helices in GCP6 (yellow), the configuration of GCP pairs in recombinant γTuSC closely resembles the native models, as exemplified by GCP pairs GCP2$_3$-GCP3$_4$ (B) GCP4$_9$-GCP5$_{10}$ (C) and GCP4$_{11}$-GCP6$_{12}$ (D). Data contributed by Marina Serna.

4.10 MZT:NTE units occupy distinct surfaces of the γTuRC cone

A significant limitation of the available γTuRC structures was the lack of structural information of most of the GCP NTEs and their MZT binding partners. To address this, we filtered the CL-MS data of recombinant γTuSC for cross-links between MZT:NTEs and GCP2/GCP3 regions for which we had obtained atomic models through cryo-EM analysis of γTuRC. To first assess the quality of our CL-MS dataset, we mapped several cross-link

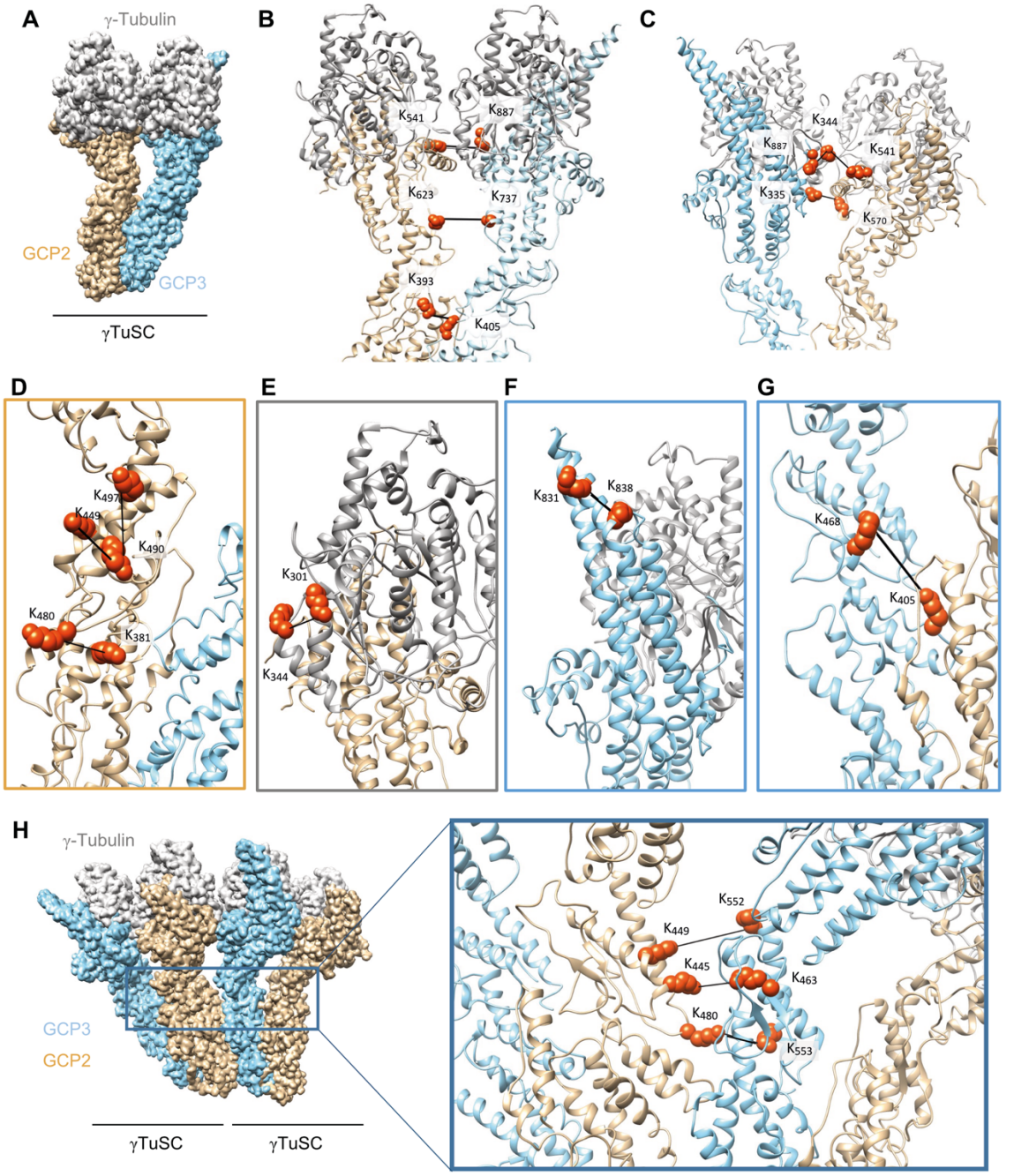

Figure 25: Correlation of CL-MS and cryo-EM data for recombinant γTuSC. Cross-linking analysis confirmed the assembly of the γTuSC (A-C), proper folding of each γTuSC subunit (D-G) and the oligomerization of several γTuSCs (H). (A) Representation of γTuSC composed of GCP2 (yellow), GCP3 (blue) and γ-tubulin (grey). Proper γTuSC assembly is evidenced by intra-γTuSC crosslinks GCP2-GCP3 (B), γ-tubulin-GCP2 and γ-tubulin-GCP3 (C), with the following cross-linking pairs: $GCP2_{K393}$-$GCP3_{K405}$, $GCP2_{K541}$-$GCP3_{K887}$, $GCP2_{K623}$-$GCP3_{K737}$, γ-$tubulin_{K335}$-$GCP2_{K570}$, γ-$tubulin_{K344}$-$GCP2_{K541}$ and γ-$tubulin_{K344}$-$GCP3_{K887}$, spaced by 13 Å, 15.5 Å, 20.5 Å, 15 Å, 15.5 Å and 18 Å, respectively. (D) Proper folding of GCP2 is shown with the cross-linking pairs K381-K480, K449-K490 and K490-K497, spaced by 18 Å, 14.5 Å and 17 Å, respectively. (E) γ-Tubulin folding is supported by K301-K344, spaced by 18.5 Å. (F) GCP3 folding is supported by K405-K468 and K831-K838, spaced by 19 Å and 13 Å, respectively. (G) γTuSC oligomerization is evidenced by crosslinking pairs detected between GCP2 and GCP3 of distinct γTuSCs: $GCP2_{K445}$-$GCP3_{K463}$, $GCP2_{K449}$-$GCP3_{K552}$, $GCP2_{K480}$-$GCP3_{K553}$, spaced by 15 Å, 21 Å and 13 Å, respectively.

pairs within a single γTuSC (**Figure 25A**) and found that these satisfied the restraints defined by the DSBU cross-linker. This analysis confirmed correct assembly of recombinant γTuSC as evidenced by intra-γTuSC cross-links at the lateral interface of GCP2 and GCP3 (**Figure 25B**), at the interface between γ-tubulin GCP2 and GCP3 (**Figure 25C**), and by intra-subunit cross-links (**Figure 25D-G**). In agreement with the idea of transient lateral associating γTuSCs (**Figure 15A** and **Figure 18A**), we also identified inter-γTuSC cross-links that would only occur between adjacent complexes (**Figure 25H**).

When we mapped cross-links of the MZT:NTE modules, we found that they localized to opposite surfaces of the γTuSC structure (**Figure 26**). While MZT2:2NTE exclusively cross-linked on the outer surface that γTuSC would form as part of the γTuRC cone, MZT1:3NTE was cross-linked to the inner, luminal surface. Since individual residues in MZT2:2NTE and MZT1:3NTE were cross-linked to multiple residues on GCP2 and GCP3 that were distributed over an area beyond a ~25 Å radius, the maximal reach of the cross-linker, both units likely have some degree of spatial mobility. Thus, the cross-link data verified proper folding and structural integrity of recombinant γTuSC, as well as interactions between adjacent γTuSCs that would be expected in the context of γTuRC. Moreover, these data show that MZT1:3NTE and MZT2:2NTE units localize to distinct γTuSC surfaces that correspond to the luminal and the outer γTuRC surface, respectively, where they seem to be spatially mobile.

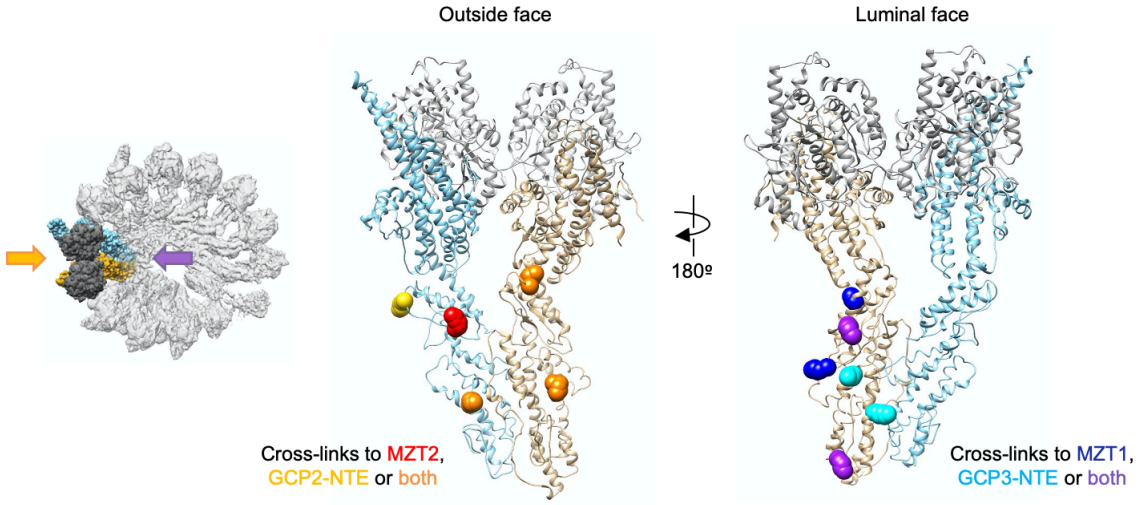

Figure 26: Mapping of crosslinks between MZT:NTE and GCP core folds in γTuSC. Residues in GCP2 and GCP3 that are involved in cross-links with MZT2:2NTE and MZT1:3NTE as indicated by the color code. MZT2:2NTE maps to outside surfaces, and MZT1:3NTE maps to inside surfaces.

4.11 MZT1:NTE units connect nonadjacent GCPs across the γTuRC lumen

Next, we sought to identify the proteins that contributed bundles of short helices in the lumen of reconstituted γTuRC. This structure, previously also observed in native γTuRC and termed "luminal bridge" (236), spans from GCP3 in position 8 ($GCP3_8$) to the region near the actin-like protein and comprises two groups of helical bundles (**Figure 27A**, termed bundle 1 and 2). In our γTuRC structure only proteins used for reconstitution should account for the observed densities. Given our previous observations, MZT1:3NTE was a candidate as CL-MS had mapped it to the γTuRC lumen. Resolution of the luminal bridge was sufficient to identify three

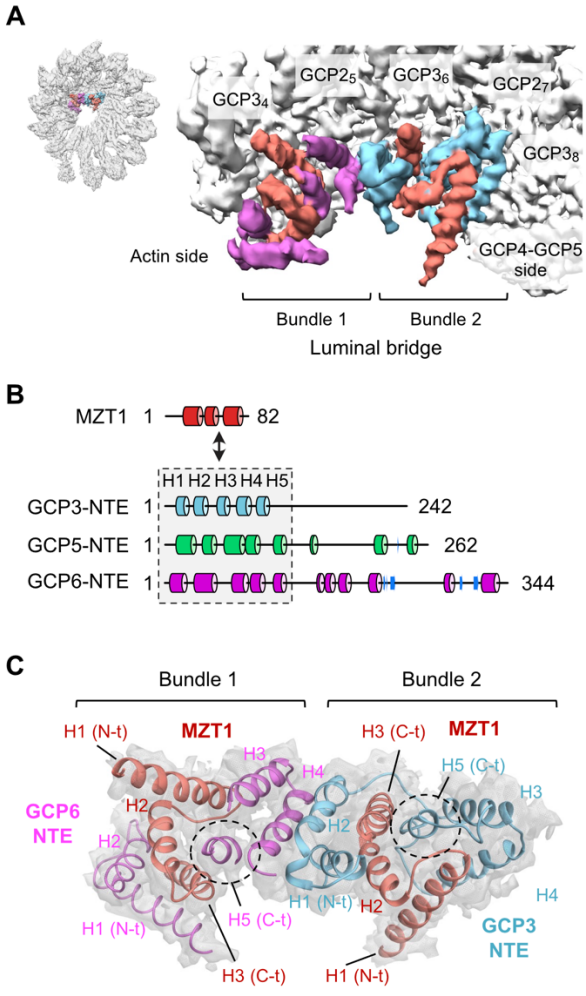

Figure 27: MZT1:3NTE and MZT1:6NTE form part of the luminal bridge. (A) Two helical bundles in the γTuRC lumen that consist of two copies of MZT1 (red), GCP3-NTE (light blue), and GCP6-NTE (purple). (B) Secondary structure predictions for MTZ1 and the NTEs of GCP3, GCP5, and GCP6. α-Helices are shown as cylinders, and β- sheets are shown as blue arrows. (C) Model of the luminal bridge fitted into the cryo-EM map (transparent density). The three helices of each MZT1 (red) are embedded in the five-helix bundles of the GCP6-NTE (purple) and the GCP3-NTE (light blue). Dashed circles highlight helix H5 used to assign bundle 1 to GCP6 and bundle 2 to GCP3. N-terminal (N-t) and C-terminal (C-t) ends are indicated. Subfigure A and C contributed by Marina Serna.

interconnected helices in bundle 2 that matched the predicted three-helix structure of MZT1 (**Figure 27A,B**) and allowed atomic model building. The remaining five helices in bundle 2 which were found intertwined with MZT1 corresponded to the NTE of GCP3 (**Figure 27C**), which we identified through bulky side chains in the MZT1-binding motif in GCP3 (89). As we did not observe a connecting density between GCP3 NTE and the γTuRC cone no firm conclusion was reached regarding which GCP3 forms bundle 2. We note, however, that $GCP3_6$ and $GCP3_8$ would both be sufficiently close. Adjacent to MZT1:3NTE we identified an almost identical three-helix MZT1 structure as part of luminal bundle 1 close to the actin-like protein (**Figure 23B** and **Figure 27A**). Curiously, rotating the structure of bundle 1 by approximately 180º revealed a high degree of similarity to the structure of bundle 2 described above, suggesting the presence of a second MZT1:NTE unit. Following a similar strategy as above, in this case we found MZT1 to be intertwined with the NTE of GCP6 (**Figure 27A-C**). Taken together, our results show that the luminal bridge in reconstituted γTuRC is built as in native γTuRC. Specifically, an actin-like protein and two MZT1:NTE units acts as building blocks of a bridge between nonadjacent GCPs in the γTuRC lumen.

4.12 GCP2 and GCP3 are stapled together by the NTE of GCP2

Next, we turned our attention on unassigned densities on the outer surface of the γTuRC cone. Both reconstituted and native γTuRC display so called “staples” (236, 237), small helical densities at the intra-γTuSC interface of GCP2 and GCP3 subunits at positions 1/2, 3/4, 5/6, 7/8, and 13/14 (**Figure 28A,B**). Previous work argued that these helices might correspond to MZT2 (236). the NTE of GCP2 or the γ-TuNA fragment of CDK5RAP2 used for purification of native γTuRC (122). However, none of these studies could provide direct evidence for a firm assignment. Again, in our recombinant complex, we could exclude proteins other than those used for reconstitution, discarding γ-TuNA. Instead, we focussed on MZT2:2NTE as our CL-MS analysis had previously mapped it to the outside of the cone (**Figure 26**). Secondary structure prediction of human MZT2 predicts four alpha-helices, of which three (H2-H3) are in the evolutionary conserved region (**Figure 28C**) (86). Honeybee (*Apis mellifera)* MZT2 for example is predicted to have three similar helices but is much shorter overall, resembling more the MZT1 domain organization. The MZT2-binding region in GCP2-NTE is predicted to contain six alpha-helices similar to the NTE of GCP3, GCP5, and GCP6 (**Figure 27B** and **Figure 28C**). Bee GCP2 shares the pre-

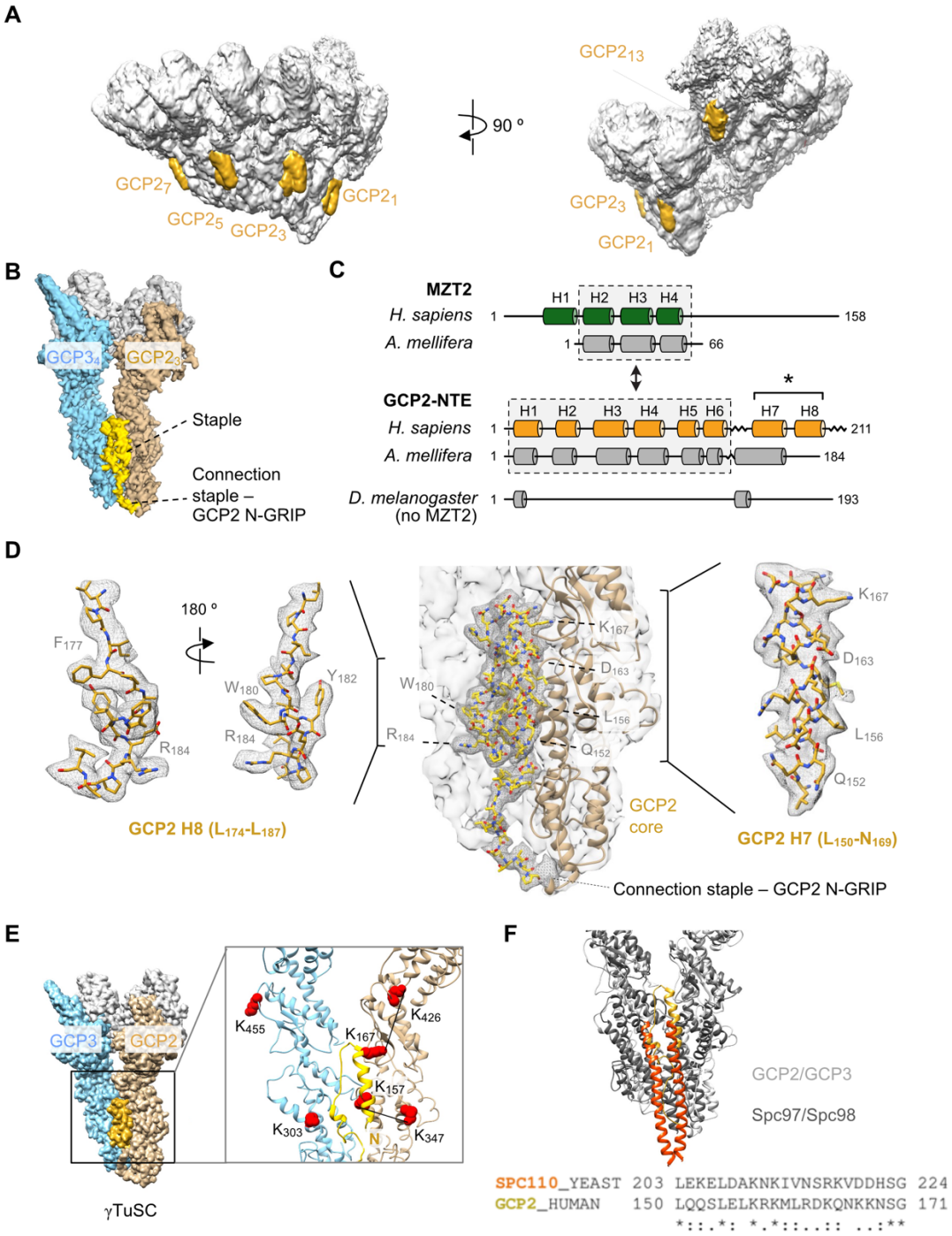

Figure 28: GCP2-NTEs staples together GCP2 and GCP3 within γTuSC. (A) Views of recombinant γTuRC at low contour level with staples highlighted in yellow. (B) The staple at the interface of GCP23 and GCP34 connects to the GCP2 core (shown in yellow). (C) Secondary structure predictions for MTZ2 and GCP2-NTEs from several species using JPred4 (228). α-Helices are indicated as cylinders. The asterisk marks the region of the staple. (D) Close-up view of the modelled staple, the density that connects staple and GCP2 core fold, and the adjustment of the atomic model to the cryo-EM map. Prominent side chains in helix H7 and H8 are indicated. (E) Mapping of cross-links between staple and N-terminal GRIP domain of GCP2 (black lines) as identified by CL-MS. GCP3 residues cross-linked with residues near the staples that were not modelled are also highlighted. (F) Superposition of the structures of GCP2-GCP3 from reconstituted γTuRC and budding yeast γTuSC bound to Spc110 (PDB 5FLZ). Spc110 and the staple partially overlap and show similarities in their primary sequence (bottom). All subfigures contributed by Marina Serna, except subfigure C.

dicted N-terminal alpha-helices with human GCP2, whereas in flies, which lack MZT2, GCP2 concomitantly lacks similar alpha-helical segments (**Figure 28C**). Together, this suggests that MZT2:2NTE may be similar to MZT1:NTE units, and thus structurally different from the staples. Interestingly, GCP2-NTE contains two additional predicted alpha-helices near the C-terminal end of the MZT2-binding region (**Figure 28C**). Examination of this region allowed us to unambiguously assign residues 150 to 188 of the GCP2-NTE to the two arms of the staple (corresponding to H7 and H8, **Figure 28D**) and residues 189 to 209 to the density that connects the staple to the N-terminus of the GCP2 core fold (**Figure 28B,D**). This atomic model was further supported by the CL-MS analysis of γTuSC. We found that GCP2 K157 and K167, that are within the modelled staple, cross-linked to the outer GCP2 surface that surrounded the staple (**Figure 28E**). In summary, to form the staple, the NTE region that immediately precedes the N-terminal GRIP domain of GCP2 generates an interface with the neighboring GCP3, and folds back to provide a second, intramolecular interface with the GCP2 N-terminal GRIP domain.

As described in a previous study, the staple occupies a region at the GCP2-GCP3 interface that is bound to Spc110 in budding yeast γTuSC (237). Budding yeast GCP2 lacks a region corresponding to the staple. Instead, a sequence with similar amino acids as in the staple of human GCP2 is present in a segment of Spc110 (**Figure 28F**). The NTE of GCP2 and Spc110 may thereby share binding determinants necessary to recognize this region of the GCP2-GCP3 interface.

4.13 Additional elements near the seam of the γTuRC cone

Apart from the GCP-NTEs and MZT:NTE entities, several additional, mostly helical elements appear to connect adjacent GCPs, potentially stabilizing the γTuRC structure. First, a likely stabilizing element was observed at the bottom of the γTuRC cone near the N-terminal GRIP domains of GCP5$_{10}$, GCP4$_{11}$, and GCP6$_{12}$ (**Figure 29A**). We could not assign this element to specific subunits, but it establishes contacts with the core folds of all three of the above GCPs, suggesting that it might stabilize their lateral association.

Second, we found a previously undescribed helical “zig-zag” element connecting the N-terminal GRIP domains of GCP6$_{12}$, GCP2$_{13}$, and GCP3$_{14}$ on their luminal side (**Figure 29A**). This feature pointed in the direction of a globular density that protruded laterally from GCP3$_{14}$ (described further below), however, we did not observe a connecting density.

These helices could correspond to parts of the long GCP6 insertion or to the NTE of GCP5. As the zig-zag element transversally connects adjacent GCPs in the γTuRC ring, it likely contributes to the stability and/or assembly of the complex. Third, another new feature not found in native γTuRC was associated with GCP6. GCP6 contains a ~800 amino acid-long insertion between the N- and C-terminal GRIP domain, which could not be located in native

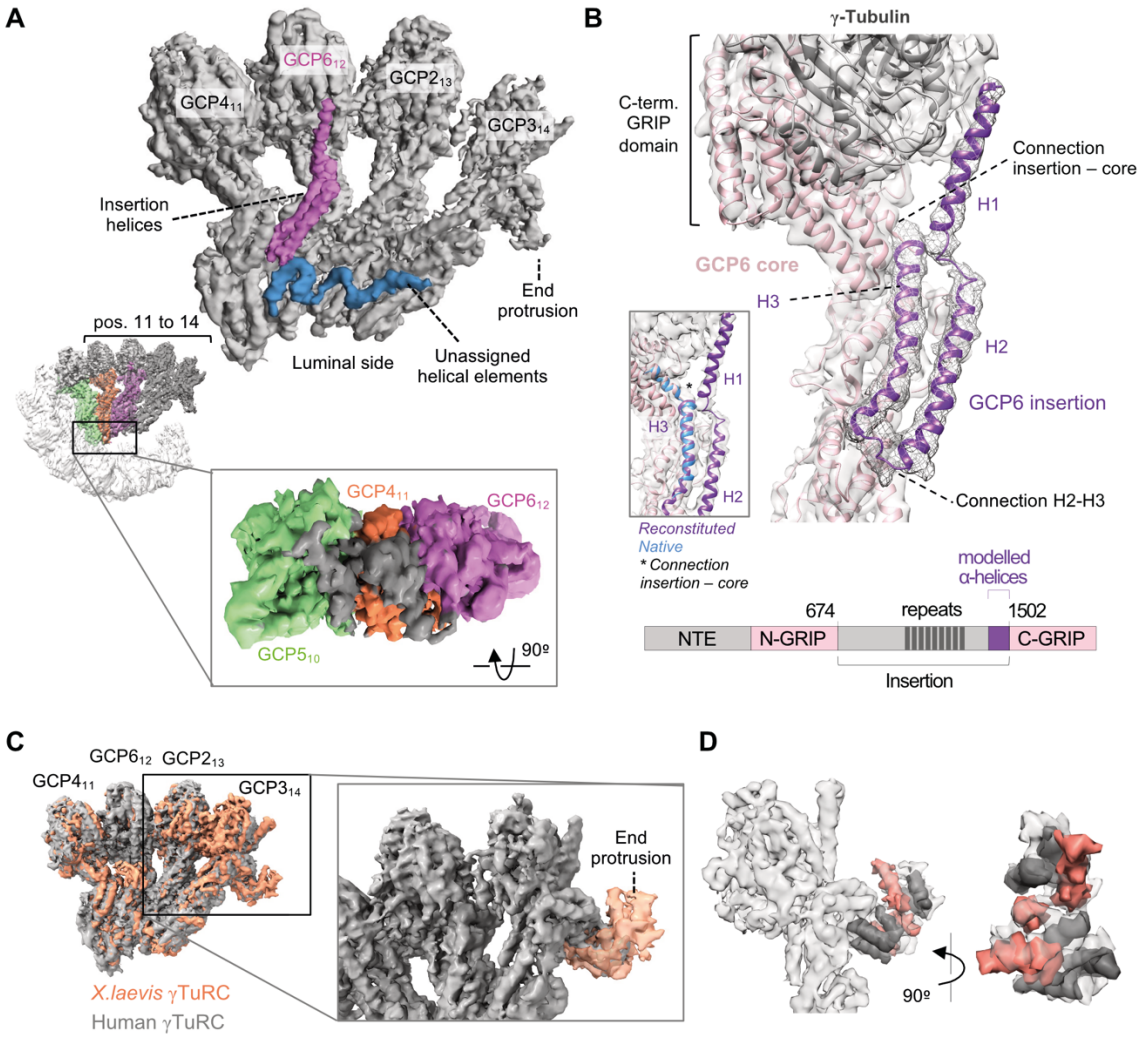

Figure 29: Additional structural elements near the seam of the γTuRC cone. (A) Top: Cryo-EM densities for helical elements on the luminal side of γTuRC. Helices assigned to GCP6 are shown in purple, and unassigned helices are shown in blue. Bottom: Unassigned helical densities (gray) contact GCPs at positions 10, 11, and 12. (B) Three long GCP6 helices (purple), named H1 to H3 as indicated, were identified as part of the large insertion between the N- and C-terminal GRIP domains. H3 was already modeled in native γTuRC (blue) and connects to the C-terminal GRIP domain of GPC6. The bottom schematic indicates the location of the modeled helices within the long GCP6 insertion. (C) Superposition of the regions displaying the end protrusion in recombinant human γTuRC (gray) and native γTuRC from *X. laevis* (orange). (D) Fitting of a MZT1:3NTE unit (MZT1 helices in red and 3NTE helices in dark gray) to the end protrusion of *X. laevis* γTuRC. Data contributed by Marina Serna.

γTuRC due to the lack of corresponding density. We obtained densities with sufficient resolution to identify three long alpha-helices on the luminal surface of GCP6 that belong to the C-terminal end of the insertion (**Figure 29A,B**). The most C-terminal helix H3 (residues Met_{1484} to Glu_{1510}) is connected to the C-terminal GRIP domain of GCP6 and was also found in the structure of human native γTuRC (**Figure 29B**, inset). Our structure showed a clear continuity between H3 and two new helices, enabling atomic modelling from Glu_{1415} to Ser_{1475} (**Figure 29B**, helices H1 and H2). The N-terminal end of H1 reaches up to γ-tubulin and is positioned very close to the surface of γ-tubulin that is in contact with α-tubulin during nucleation.

Lastly, a novel element we termed 'end protrusion' was identified that was also observed in native γTuRC but was left unassigned. A very recent study proposed it to be a MZT:NTE-like module (229). The density extends laterally from the C-terminal half of $GCP3_{14}$ and is not present in GCP3s at other positions (**Figure 29A**). The flexibility at position 14 likely hindered obtaining sufficient resolution for atomic modeling, however, the corresponding density is relatively well defined in native γTuRC from *Xenopus laevis* (**Figure 29C**) (235). Closer examination revealed notable similarity with the helical MZT1:NTE units described above for the luminal bridge (**Figure 29D**). Since the single copy of MZT1:6NTE in γTuRC is part of the luminal bridge, the end protrusion should correspond to MZT1:3NTE or MZT1:5NTE. Given that we found MZT1:3NTE to be cross-linked to the luminal side and almost exclusively to luminal GCP2 surfaces (**Figure 26**) and our analysis so far failed to identify MZT1:5NTE units, we suggest that the end protrusion may be formed by the single MZT1:5NTE unit present in γTuRC.

4.14 MZT:NTE units are dispensable for γTuSC assembly

The reconstitution and characterization of human γTuSC (chapter 4.3) highlighted an important interdependency between MZT1 and MZT2, and the NTE of GCP3 and GCP2, respectively. Solubilization of the NTEs by MZTs led to γTuSC assembly where MZT:NTE form structural units with defined flexibility. The structural analysis of γTuRC (chapter 4.6 to 4.10) revealed that one MZT1:3NTE unit and one MZT1:6NTE unit are used to stabilize the higher order γTuRC structure as part of the luminal bridge. While additional MZT1:NTE units are very likely present, they may have preserved their spatial mobility after incorporation into γTuRC, making them undetectable in the Cryo-EM map.

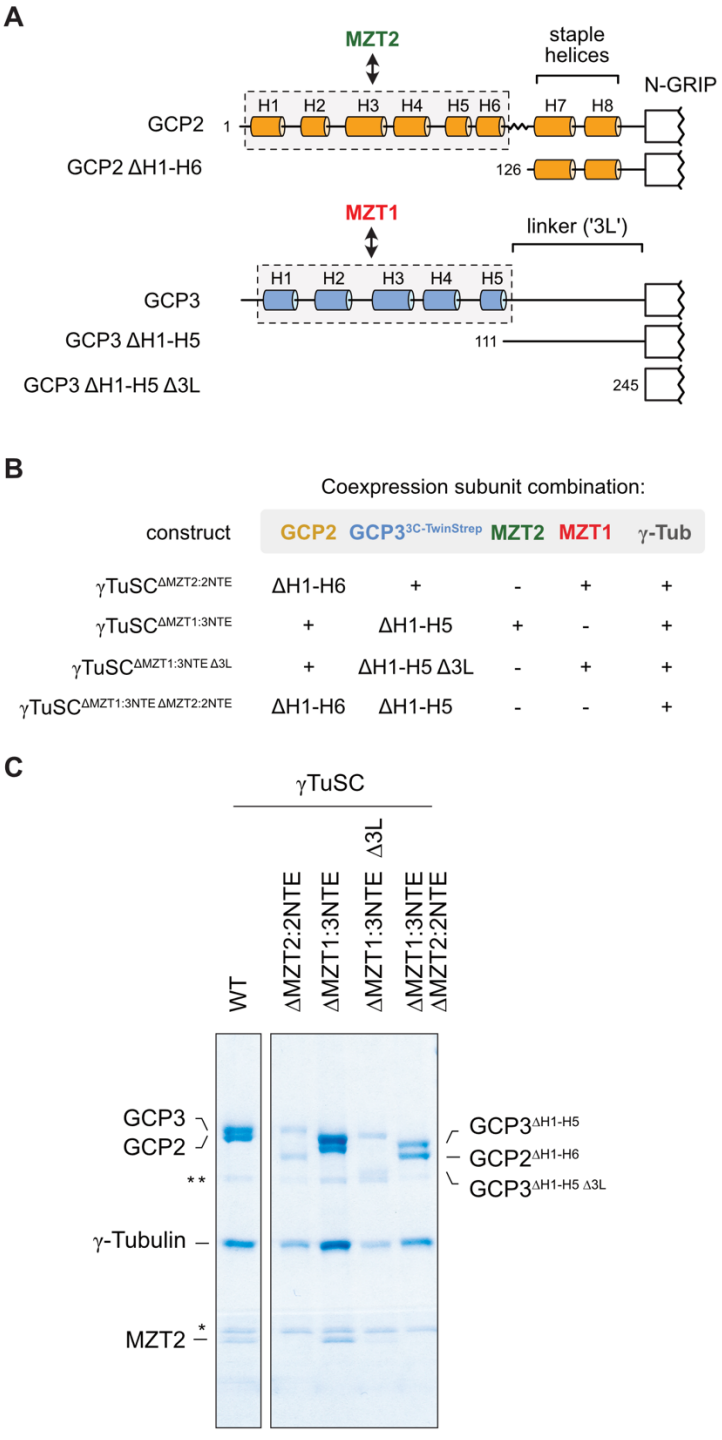

Figure 30: Reconstitution of γTuSC mutants lacking MZT:NTE units.(A) Secondary structure representation of GCP2- and GCP3-NTEs. An N-terminal truncation of GCP2 H1-H6 deletes the MZT2 binding region while preserving the staple. N-terminal truncation of GCP3 H1-H5 deletes the MZT1 binding region, and additional truncation of a linker (3L) deletes the whole GCP3 NTE until the N-GRIP domain. (B) Overview of subunit combination of mutant γTuSC constructs. GCP2 and GCP3 were included as described in (A), '+' indicates full-length sequence, '-' indicates subunits omitted in coexpression constructs. (C) Subunit combinations from (B) were coexpressed, affinity-purified, and analyzed by SDS–PAGE. Asterisk indicates contaminating 3C protease (25 kDa) used for elution. Double asterisk indicates unknown protein that copurifies when 500 mM NaCl is present in purification buffers.

Likewise, no defined MZT2:2NTE structure could be identified, which may resemble MZT1:NTE units and display similar mobility. Together, these data suggest that the main function of MZT:NTEs may be to "prime" γTuSCs for a specific role in γTuRC. If so, MZT1:3NTE and MZT2:2NTE may be dispensable for γTuSC assembly. To test this, I constructed baculoviruses to express γTuSC mutants lacking the MZT-binding region of either GCP2 or GCP3 and lacking coexpression of MZT2 (γTuSC$^{\Delta MZT2:2NTE}$) or MZT1 (γTuSC$^{\Delta MZT1:3NTE}$), respectively. SDS-PAGE analysis showed successful purification of γTuSC$^{\Delta MZT2:2NTE}$ and γTuSC$^{\Delta MZT1:3NTE}$ with a subunit stoichiometry that was similar to normal γTuSC, indicating that truncating the GCP NTEs is sufficient to bypass the requirement of MZT1 or MZT2 in γTuSC reconstitution (**Figure 30**). In the case of GCP3, the entire NTE (residues 1-244) could be removed and mutant γTuSC could still be purified. Furthermore, a combined deletion of GCP2$_{1-125}$ and GCP3$_{1-110}$ bypassed the requirement for both MZT1 and MZT2, yielding γTuSC$^{\Delta MZT2:2NTE,\ \Delta MZT1:3NTE}$. Together, these data indicate that MZT:NTE units are dispensable for γTuSC assembly.

4.15 MZT2:2NTE is dispensable for RUVBL-mediated γTuRC assembly

I sought to further test the hypothesis that the MZT2:2NTE unit may have a regulatory role in γTuRC rather than participating in γTuRC assembly. After additional refinement of the native γTuRC structure, a very recent study was able to identify a structure corresponding to MZT2:2NTE (229). In line with our previous observations, MZT2:2NTE was found to consist of an intercalated bundle of α-helices in analogy to MZT1:NTEs. Moreover, MZT2:2NTE was bound to a dimer of γTuNA, the nucleation-activating fragment of CDK5RAP2, that the authors used to purify the native complex (**Figure 31A**, position 12-14). This observation is in line with a proposed regulatory role and argues against a role of MZT2:2NTE in γTuRC assembly. Consistent with this, purified γTuSC$^{\Delta MZT2:2NTE}$ still interacted with RUVBL (**Figure 31B**). This is in agreement with the fact that CL-MS of γTuSC-RUVBL failed to detect crosslinks detected between MZT2:2NTE and RUVBL (**Figure 19**). Of note, the relative amounts of bound RUVBL appear to be higher for γTuSC$^{\Delta MZT2:2NTE}$ compared to normal WT γTuSC (**Figure 31B**). To test whether γTuSC$^{\Delta MZT2:2NTE}$ can integrate into γTuRC as observed for normal γTuSC, I attempted to reconstitute γTuRC devoid of MZT2:2NTE by combining γTuSC$^{\Delta MZT2:2NTE}$ expression with GCP4, GCP6$^{3C\text{-}TwinStrep}$ and GCP5$^{mBFP\text{-}BAP\text{-}TEV\text{-}ALFA}$ ('GCP5^{BBA}').

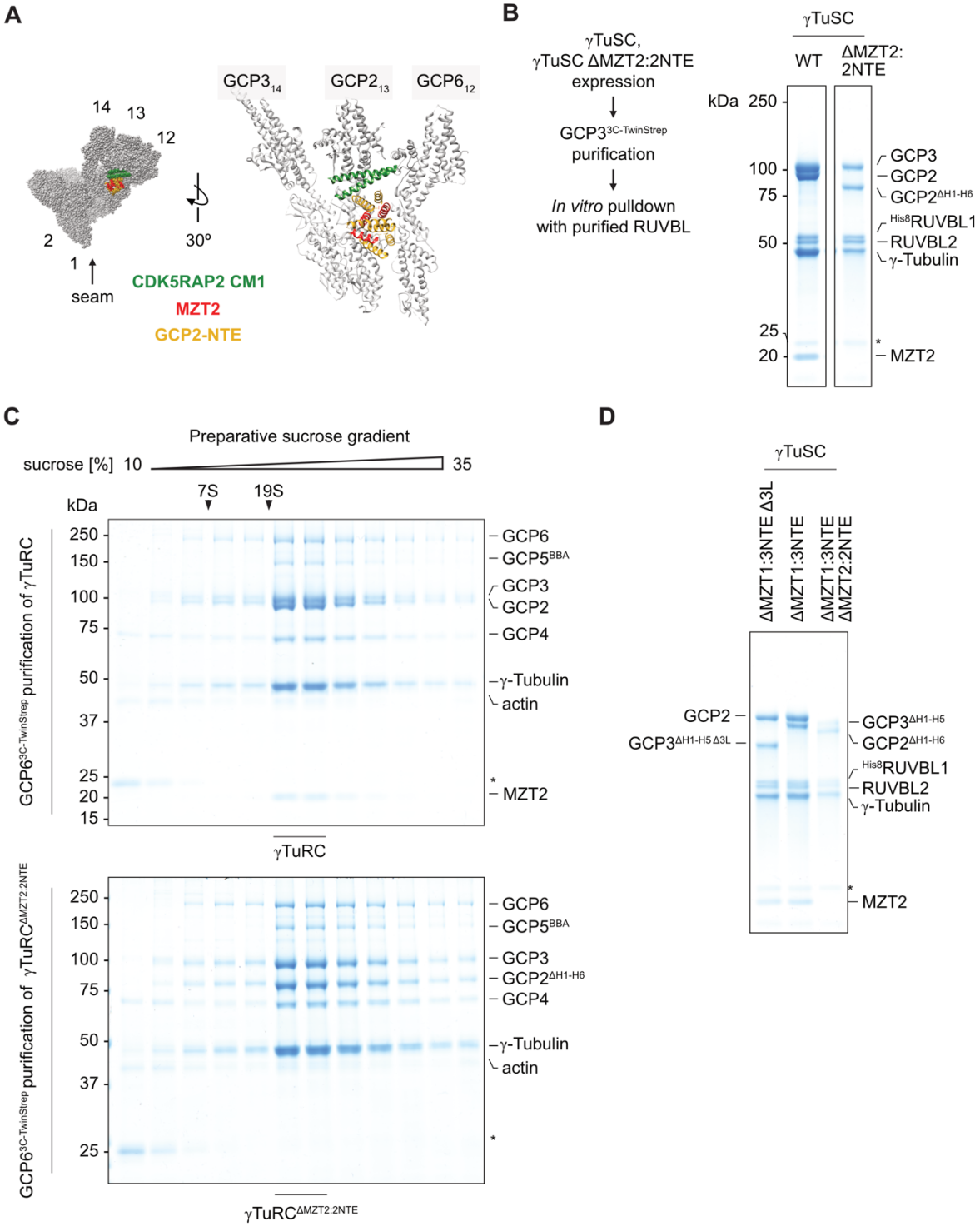

Figure 31: MZT2:2NTE are not required for γTuSC and γTuRC assembly. (A) Side-view of native γTuRC (PDB 6V6S) aligned with γ-TuNA (green) and MZT2:2NTE (red and gold) bound at position 12-14 (PDB 6X0V) close to the seam. (B) Purified, immobilized γTuSC and γTuSC$^{\Delta MZT2:2NTE}$ were incubated with recombinant RUVBL1-RUVBL2 before elution and analysis by SDS-PAGE. (C) Affinity purified γTuRC and γTuRC$^{\Delta MZT2:2NTE}$ were fractionated by sucrose gradient centrifugation and analyzed by SDS-PAGE. Asterisks denote contaminants as in Figure 13A. (D) Indicated γTuSC mutants were tested for ^{His8}RUVBL1-RUVBL2 binding as in (B).

Indeed, a sucrose gradient fractionation of the affinity purified sample revealed large complexes in the same fractions of similar subunit stoichiometry as normal γTuRC, fractions of similar subunit stoichiometry as normal γTuRC (**Figure 31C**)., indicating successful reconstitution of γTuRC$^{\Delta MZT2:2NTE}$. This shows that MZT2:2NTE units are dispensable for RUVBL-mediated γTuRC assembly.

CL-MS analysis of γTuSC-RUVBL suggested that RUVBL may not bind to regions involving the GCP3-NTE that contains the MZT1:3NTE unit (**Figure 19**). This result predicts that mutant γTuSCs lacking GCP3-NTE and/or the MZT1:3NTE unit should retain the ability to bind RUVBL. To test this, I purified the remaining γTuSC mutants (**Figure *30***) and tested their ability to bind purified RUVBL using the same assay as for normal γTuSC and γTuSC$^{\Delta MZT2:2NTE}$ (**Figure 31B**). Analysis by SDS-PAGE showed that, as expected, γTuSC$^{\Delta MZT1:3NTE}$, γTuSC$^{\Delta MZT1:3NTE\ \Delta 3L}$, and γTuSC$^{\Delta MZT1:3NTE\ \Delta MZT2:2NTE}$ retained their ability to bind purified RUVBL *in vitro* (**Figure 31D**). Together, these results suggest that during γTuRC assembly, RUVBL binds to γTuSC does neither require the entire GCP3-NTE including the ΔMZT1:3NTE unit, nor the part of the GCP2-NTE that contains ΔMZT2:2NTE unit.

5. Discussion

5.1 A recombinant system to study human γ-tubulin complexes

In this thesis, I present the first reconstitution and purification of human γTuRC using baculovirus-mediated coexpression in insect cells. Building the γTuRC structure required eight recombinant proteins: γ-tubulin, GCP2, GCP3, GCP4, GCP5, GCP6, MZT1, and MZT2 (**Figure 32**). In addition, an actin-like protein was incorporated nonrecombinantly, provided by the expression host. Importantly, these nine proteins did not readily assemble into γTuRC but required coexpression of the RUVBL assemblase composed of RUVBL1 and RUVBL2. RUVBL was not part of the final γTuRC structure but catalyzed the productive assembly of its subunits. This result may explain why reconstitution has not been achieved previously despite the identification of all required subunits many years ago. Having defined the minimal set of components to build the γTuRC core structure, we can now exclude NME7 and LGALS3BP, proteins previously found to be associated (122, 126, 160) to play a structural role in γTuRC, thus allowing their function to be dissected as regulatory components.

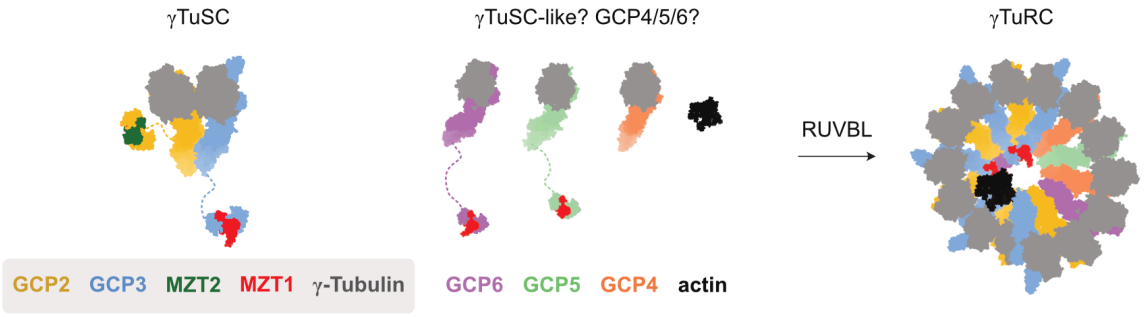

Figure 32: Subunits of the γTuRC core structure. Human γTuRC consists of nine essential components: γ-Tubulin, GCP2, GCP3, GCP4, GCP5, GCP6, MZT1, MZT2, and actin. The assembly into γTuRC requires the RUVBL assemblase. Subunits are color-coded as shown, unresolved parts of the GCP NTEs are shown as dashed lines.

A very recent study reported that additional coexpression of NEDD1 together with the core subunits used in my study allows γTuRC reconstitution in a recombinant insect cell system (238). However, comparison with the structure of native γTuRC revealed the presence of additional densities in NEDD1-containing, reconstituted γTuRC indicating that it does not fully match the native γTuRC structure. One past study had reported γTuRC integrity

defects upon NEDD1 depletion (128), while multiple others have found the opposite (110, 127, 150). Moreover, NEDD1 is not always found in purifications of native γTuRC (133). NEDD1 may thus be only weakly associated with γTuRC. While NEDD1 binding may contribute to γTuRC stability, it seems unlikely that NEDD1 is an essential part of the γTuRC core structure. Another very recent study reported a method to express and purify a recombinant γTuRC-like complex without coexpression of MZT2 (239). My work showed that γTuSC subunits hardly interact without coexpression of MZT2 and are largely insoluble, resulting in low yields during purification. In line with possible low yield, the authors only present Western Blot data verifying the presence of some γTuRC subunits in a large complex. Whether potential GCP2 NTE stabilizing proteins were present in the sample that could compensate for the lack of MZT2, was not tested. Thus, while alternative paths to assemble γTuRC in recombinant expression systems may exist, my work demonstrates that RUVBL mediated γTuRC assembly *in vitro* occurs with superior efficiency and yield, produces γTuRC that closely resembles native γTuRC, and provides evidence that RUVBL mediated γTuRC assembly also occurs in human cells. Moreover, it is the only work to date that can provide an explanation for the requirement of all core subunits to form the minimal γTuRC core structure. Having defined the minimal components of the core structure now allows functional dissection of γTuRC elements. Using the recombinant system, I show that truncation of the MZT2:2NTE unit that is part of the NTE of GCP2, still allows assembly of γTuRC, suggesting that this element may exclusively serve regulatory roles such as facilitating interaction with γTuRC adapters (229).

Besides γTuRC, I also report the reconstitution of human γTuSC. In contrast to reconstitutions of yeast and fruit fly γTuSCs, the human complex required coexpression of MZT1 and MZT2. This work demonstrates, for the first time, that vertebrate proteins can assemble stable γTuSC. Thus, in analogy to the situation found in less complex eukaryotes, γTuSC and γTuRC may coexist in vertebrates. In addition, γTuSC-like complexes composed of GCPs 4, GCP5, GCP6 and γ-tubulin may also exist. While their molecular composition remains to be defined, rather than MZT proteins, unassigned features that connect GCP5, GCP4, and GCP6 in reconstituted γTuRC (**Figure 29A**) and that were also observed in native γTuRC, may stabilize interactions between these GCPs (236). The recombinant expression system that I have described here now also provides means,

by omission of γTuSC subunits, for reconstitution and characterization of GCP5-, GCP4-, and GCP6-containing γ-tubulin complexes, including a recently described GCP5-GCP4-GCP6 complex (130).

5.2 RUVBL is a γTuRC assembly factor

The requirement for RUVBL in γTuRC assembly was observed not only in the reconstitution system but also in human cells, where it may serve as a regulatory mechanism. Consistent with previous studies, RUVBL-depleted cells displayed severe mitotic spindle defects (185, 231). Rather unexpectedly, I observed that RUVBL-depleted cells display centriole duplication defects. While this may result from impaired γTuRC integrity (113), γTuRC was not completely disrupted as determined by sucrose gradient analysis. Thus, additional RUVBL substrates could be involved that explain this phenotype. RUVBL depletion interfered specifically with the incorporation of γTuSC and MZT2. Apart from providing essential structural support to GCP2-NTE, the cellular roles of MZT2 are poorly understood. Moreover, RUVBL-depletion led to a reduction in overall levels of GCP6 and GCP5. The functional consequences of these RUVBL-dependent alterations in γTuRC composition remain to be determined.

A well-characterized role of RUVBL is to promote assembly of protein complexes such as RNA polymerases and PIKKs. Here, RUVBL forms part of the R2TP complex, which serves as a platform that brings client proteins together with the HSP90 chaperone (201, 202, 240, 241). However, in other cases, RUVBL also promotes protein complex assembly in the absence of R2TP and HSP90, but how this is achieved is still mysterious. The here presented *in vitro* reconstitution system is an ideal model for tackling this issue. Some RUVBL copurified with reconstituted γTuRC but was not a stoichiometric component as in nucleosome remodelers (197, 198). Instead, RUVBL interacted with subcomplexes such as γTuSC but was itself not required for γTuSC assembly. Using purified mutant γTuSC, I showed that the MZT2:2NTE unit is not required for the interaction between γTuSC and RUVBL. Consistent with this, the RUVBL assemblase is able to integrate $\gamma TuSC^{\Delta MZT2:2NTE}$ into γTuRC. Additionally, RUVBL still interacted with γTuSC mutants that lacked the MZT1:3NTE unit or the entire NTE of GCP3. Consistent with RUVBL binding to the GCP core fold, CL-MS analysis of γTuSC-RUVBL found RUVBL residues crosslinked to the GCP GRIP domains, but not to the GCP2/3 NTE or MZT proteins. Furthermore, my

CL-MS analysis suggested potential ways how the interaction between γTuSC and RUVBL may occur (**Figure 19**). First, the analysis pointed towards an interaction mode that may involve the RUVBL2 DII domain bears similarity to how RUVBL engages with other substrates such as INO80, SRCAP or DHX34 (197, 198, 208). Second, GCP2/3 residues of the GCP core fold crosslinked to the RUVBL2 in a manner that likely requires prior replacement of the RUVBL2 N-terminal tail as and nucleotide release from RUVBL2, as these parts otherwise participate in stabilizing the nucleotide-bound form of RUVBL (189, 206). Similar conformational changes in RUVBL2 have recently been observed upon interaction with DHX34, another RUVBL substrate in the nonsense-mediated mRNA decay pathway, where RUVBL2 has empty nucleotide pockets (208). While the functional implications of this RUVBL conformation remained mysterious, the authors speculated that the 'empty-pocket' form of RUVBL2 may render the RUVBL-substrate complex an interaction hub ready to interact with other required factors, which the authors did not include in the study. Detailed biochemical and structural analysis of the γTuSC-RUVBL complex is needed to understand whether RUVBL may similarly render γTuSC competent to interact with additional γTuRC components.

Along this line, it is tempting to hypothesize that RUVBL has a role in allowing γTuSC and γTuSC-like protomers to assemble into the higher-order γTuRC structure. Liu *et al.* (235) proposed that GCP4, GCP5, and GCP6 may form a platform, onto which multiple γTuSC assemble. Consistent with such a model, depletion of RUVBL in cells impaired incorporation of γTuSC into γTuRC. RUVBL also binds GCP4, GCP5 and GCP6 in cells and thus may facilitate the various interconnections among GCPs that stabilize their lateral association. Lateral association mediated by RUVBL may also confer overall stability to GCPs since RUVBL-depleted cells had lower levels of soluble GCP5 and GCP6.

We have found that the N-terminus of GCP6 and MZT1 form a MZT1:6NTE unit as part of the luminal bridge. While our resolution was not sufficient to build molecular models for the electron densities that seem to connect MZT1:6NTE with the actin-like protein in the luminal bridge, recent work has reached sufficiently high resolution to identify a small helix at the very N-terminus of the GCP6 NTE that contacts the actin-like protein (229). This GCP6 helix contacts actin in the barbed-end groove, a common interaction mode of actin-monomer binding proteins that impedes actin polymerization (242). As we currently lack detailed knowledge about the assembly mechanism, an open question is at what stage

of γTuRC assembly the luminal bridge is built. Interestingly, very recent cryo-EM structures of CCT (23) could trap an actin-CCT intermediate that additionally contained PhLP2B, a known regulator of actin and tubulin folding (24). Here, PhLP2B interacts with actin inside CCT via a small helix in a manner that is highly similar to the interaction mode of GCP6 with actin. This raises the possibility that complex formation between actin and GCP6 is aided by CCT. While a GCP6-actin complex could be formed first before interaction with other γTuRC subcomplexes, CCT may additionally provide means of coupling it to other chaperone machineries such as R2TP (243). On the other hand, examples from other multiprotein complexes show that RUVBL can coordinate the quaternary structure formation of actin or actin-related proteins with binding partners (197, 198), that are known to not require CCT. Further arguing against a CCT-actin-GCP6 intermediate, I did not observe copurification of protein impurities that could correspond to CCT after the GCP6-affinity purification step during isolation of recombinant γTuRC (**Figure 21A** and **Figure 31C**, CCT subunits should range between ~50-65 kDa), which is observed in affinity-purifications of known CCT substrates such as γ-tubulin (122).

The evidence obtained in this work together with previous finding allows formulation of a speculative γTuRC assembly mechanism (**Figure 33**). Building on previously proposed models (130, 235), subcomplexes consisting of GCP4/GCP5/GCP6/MZT1 and perhaps actin may assemble first, but may be unstable in the absence of RUVBL. In the presence of RUVBL, these complexes are stabilized and the actin-bound MZT1:6NTE is presented in a conformation that is compatible with binding of γTuSCs via the GCP6 'belt', a part of the GCP6-NTE that extends out of the MZT1:GCP6 units and makes contacts with the luminal surfaces of γTuSC subunits in position 3-6 (229). γTuSC gets recruited through RUVBL, coordinating the assembly of the luminal bridge, followed by γTuSC oligomerization. After luminal bridge formation, critical quaternary structure arrangements have been made, causing the resulting GCP4/5/6-γTuSC intermediate to be more stable. RUVBL may still stay bound and help again in recruitment of the two remaining, more weakly associated γTuSCs. RUVBL bound to the γTuRC seam may represent a late stage intermediate before RUVBL is eventually released from fully assembled γTuRC. Further dissection of the interactions of RUVBL and γTuRC subunits *in vitro*, in combination with structural studies, should allow unraveling the mode of action of the RUVBL assemblase. Rather than coexpressing all components as in this thesis, one may also attempt reconstitution of γTuRC with separately purified RUVBL and γTuRC subcomplexes.

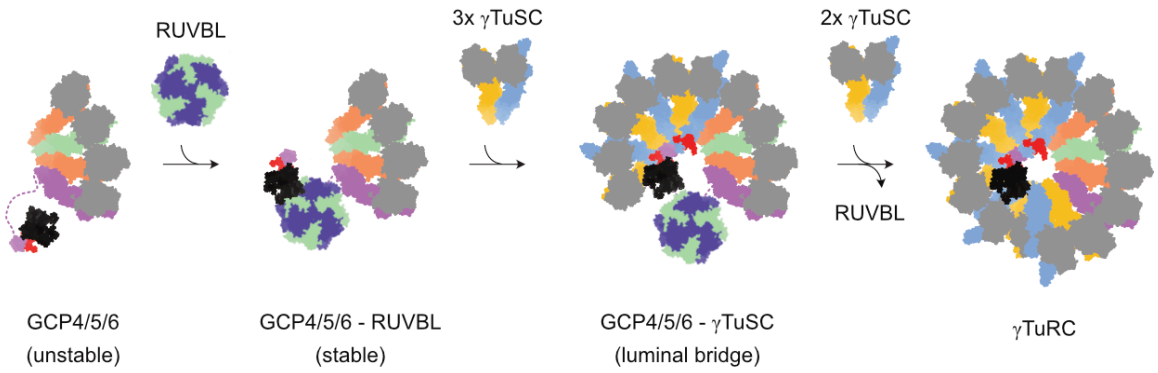

Figure 33: Hypothetical RUVBL-mediated γTuRC assembly mechanism. RUVBL may mediate stepwise assembly of γTuRC by coordinating interactions between γTuSCs and potential γTuSC-like subcomplexes. Color-codes as in Figure 32: γ-Tubulin (gray), GCP2 (yellow), GCP3 (blue), GCP4 (orange), GCP5 (green), GCP6 (violet), MZT1 (red), MZT2 (not shown), actin (black).

5.3 MZT proteins are part of the γTuRC core structure

The GCP-NTEs and MZT1 and MZT2 play central roles in γTuRC assembly. MZT1 forms structurally similar but distinct units with the NTEs of GCP3, GCP5, and GCP6, whereas MZT2 forms a unit with the NTE of GCP2. One MZT1:3NTE and one MZT1:6NTE form the luminal bridge, suggesting that distinct units can be used in a combinatorial fashion. This conclusion was also reached after further refinement of the native human γTuRC cryo-EM structure and X-ray crystallography of recombinant MZT1:6NTE (236) and of MZT1:3NTE and MZT1:5NTE (230).

The intercalated configuration of helices belonging to two different polypeptides in MZT:NTE units may be crucial for the biogenesis and stability of the involved proteins. In agreement with this, the severe experimental limitations faced in past structural studies of separately purified MZT1 and GCP3 NTE may have been due to the unstable nature of both proteins kept in isolation. Indeed, the majority of MZT1 residues found by Cukier *et al.* (142) to undergo changes in their chemical environment upon GCP3 NTE binding, we now find to participate in the formation of the helical bundle structure of MZT1:3NTE. The instability of the uncomplexed NTEs of the GCPs likely explains why production of soluble, recombinant γTuSC strongly depended on coexpression with both MZT1 and MZT2. Similar observations were previously made for recombinant expression of GCP2, GCP3, γ-tubulin and MZT1 in fission yeast (140). Similarly, biochemical reconstitution of potential γTuSC-like complexes containing GCP5 and GCP6 will very likely depend on

coexpression of MZT1 as well. MZT proteins and their corresponding GCP binding partner also showed coregulation of their expression levels in their native cellular environment and not merely in a heterologous expression system, indicating that complex formation is also important under physiological conditions and thus closely monitored and regulated.

One intriguing feature of the MZT proteins is their small size. Similarly small proteins, sometimes referred to as microproteins, have been described to perform regulatory functions in processes such as transcription or cell cycle progression (244). Large scale approaches have identified a range of such microproteins in animals including humans that seem to regulate vital cellular functions, with a tendency of microproteins forming complexes with larger proteins (244, 245). During protein biosynthesis, GCP NTEs emerge first from the ribosome exit channel, so one could speculate about a co-translational regulatory mechanism involving MZT protein binding to the emerging NTE. Only recently, similar cotranslational mechanisms have been uncovered that control cellular tubulin levels (246, 247). Alternatively, additional regulators such as HCA66 may be involved in stabilizing γTuRC assembly intermediates in the absence of either one binding partner (248). Thus, apart from their strong biochemical interdependency *in vitro*, regulation of MZT protein binding to GCP NTEs could provide cells with additional means to control γTuRC assembly, perhaps even in response to certain stimuli such as nutrient availability. Assuming that all GCP NTEs are bound to MZT proteins, production of a single ~2.3 mDa γTuRC made from 41 polypeptides comes at high energetic costs. Adding to the burden of translation, γ-tubulins must be folded by CCT in an ATP-consuming process, and assembly of the γTuRC core structure requires RUVBL, which may additionally require ATP. Thus, mechanisms to assemble γTuRCs only when and where they are needed may become important under low nutrient conditions.

Our CL-MS with recombinant γTuSC suggested that MZT1:3NTE and MZT2:2NTE, despite displaying some mobility, were restricted to the inside and outside of the γTuRC cone, respectively. Previous CL-MS analysis of purified γTuRC using a different cross-linker is also consistent with the presence of MZT1:3NTE and MZT2:2NTE units and with MZT2 occupying the outer surface of the γTuRC cone (237). We obtained structural evidence that MZT:NTEs stabilize γTuRC. As part of the luminal bridge, MZT1:3NTE and MZT1:6NTE connect nonadjacent GCPs. As also proposed by another study, one MZT1:NTEs likely forms the end protrusion (229). On the basis of our and previous data,

we propose that the end protrusion is formed by a single MZT1:5NTE, but further analysis is needed for a firm assignment. Despite the presence of multiple GCP3 copies, additional MZT1:3NTEs were not observed. No clear densiometric measurements could be obtained to determine how many MZT copies are present in recombinant γTuRC (**Figure 21A**). However, the recombinant system provides a tool to modify MZT proteins for determining their precise copy number in γTuRC. This could be achieved, for example, by engineering MZT subunits in recombinant γTuRC for quantitative Western-Blotting or quantitative stain-free SDS-PAGE (249, 250). Given that coexpression of MZT1 strongly increased γTuSC solubility it can be argued that the remaining GCP3 NTEs are also in a complex with MZT1 molecules rather than free. As indicated by CL-MS analysis of γTuSC, MZT:NTEs display spatial mobility, a property that is likely retained by MZT:NTEs that do not participate in the luminal bridge or the end protrusion. Flexible elements readily escape high-resolution structure determination by cryo-EM (251), which could be the reason why we did not observe additional electron densities corresponding the remaining MZT1:3NTEs. Furthermore, my mutational analysis of γTuSC highlights that MZT:NTE units prime γTuSC for γTuRC-restricted functions as their combined removal did not seem to affect the γTuSC core structure. Further biochemical and structural analysis is needed to substantiate these findings.

The lateral association of the end protrusion with $GCP3_{14}$ may indicate a specific function at the seam of the γTuRC cone. Analysis of purified human γTuSC showed that γTuSCs have some propensity to oligomerize via lateral association (**Figure 13B,C**). Past studies with purified budding yeast complexes have shown similar oligomerization but only upon interaction with fragments of the γTuSC adapter Spc110, leading to formation of helical γTuSC-spirals (95, 96). While these studies failed to identify the factor limiting γTuSC oligomerization once a γTuRC has formed, the end protrusion in vertebrate γTuRC likely inhibits binding of an additional γTuSC to the C-GRIP interface of $GCP3_{14}$. Further down in the γTuRC lumen at this position, the actin-like protein may render the N-GRIP interface of $GCP3_{14}$ sterically inaccessible. In contrast, our structure did not resolve elements that would prevent further addition of γTuSC at $GCP2_1$. One possibility would be that a mobile MZT2:2NTE unit at the outside of the γTuRC cone in position 1 would inhibit lateral association of an additional γTuSC. However, recombinant mutant $\gamma TuRC^{\Delta MZT2:2NTE}$ showed a very similar subunit stoichiometry to normal γTuRC, which makes it unlikely that MZT2:2NTE is sufficient to impede another γTuSC from binding at the lateral $GCP2_1$

interface. While further structural analysis of γTuRC$^{\Delta MZT2:2NTE}$ is required to verify this, the current interpretation of the data is that one MZT1:NTE unit at position 14 may serve to limit addition of γTuSCs once the γTuRC core structure is built, whereas MZT2:2NTEs are likely not involved.

Although not resolved in our structure, MZT:NTEs that do not participate in the γTuRC core structure could mediate additional interactions within γTuRC or with other factors. Binding of adapter proteins to γTuRC such as NEDD1 and CDK5RAP2 has been shown to require MZT1 in cells (113, 135). Having unequivocally identified MZT1 as part of the γTuRC core structure, MZT1 function can no longer be interpreted by means of being a purely regulatory subunit that mediates the interaction of γTuRC adapters to the γTuRC core. On the other hand, by forming part of the luminal bridge and likely the end protrusion, MZT1 participates in formation of structural features that seem γTuRC specific, and thus are unlikely to be found in γTuRC subcomplexes. Thus, these two structural features that are limited to the higher-order γTuRC structure could allow γTuRC binding factors, such as NEDD1 and CDK5RAP2, distinguish between fully assembled γTuRC and its subcomplexes. In agreement with this, cryo-EM analysis of native human γTuRC showed electron density at the seam of γTuRC termed 'plug' (236). but no molecular model was built. Future work with purified recombinant γTuRC and γTuRC adapters will help us to understand the biochemical and structural basis of γTuRC recruitment to MTOCs and stimulation of its nucleation activity.

The CL-MS data showed engagement of MZT2:2NTE modules on the outside of the γTuRC cone near the staple elements. While we were unable to find MZT2:2NTE modules in the cryo-EM map, we could assign a region of the GCP2 NTE that is adjacent to the MZT2 binding site to the staple elements. Apart from stabilizing the intra-γTuSC interface, each staple with its adjacent MZT2:2NTE unit would be suited for interactions with other, potentially regulatory factors. Consistent with this speculation, a MZT2:2NTE unit was proposed to interact with a short CDK5RAP2 CM1 peptide at the outside surface of GCP2$_{13}$ (229).

5.4 The core structure of the microtubule nucleator γTuRC

Using cryo-EM analysis, we found that reconstituted γTuRC resembles native γTuRC isolated from human or frog cell extract. As native γTuRC, it has nucleation activity but

displays an asymmetric structure that deviates from the circular geometry of a microtubule end. The open asymmetric core structure explains the relatively low nucleation activity of γTuRC *in vitro* (98, 126, 237) that has puzzled the field since its discovery. On the other hand, this feature represents an elegant mechanism to prevent uncontrolled microtubule nucleation from preassembled γTuRCs that are present in the cytoplasm of vertebrate cells. As a result, assuming a templated nucleation model, major conformational changes may be required to stimulate γTuRC nucleation activity (134, 145, 235–237).

Apart from MZT1:NTE and MZT2:2NTE modules, we identified additional, likely stabilizing features. The first, a luminal helix-hairpin element, runs across the N-terminal GRIP domains of $GCP2_3$, $GCP3_4$, $GCP2_5$, and $GCP3_6$ and is additionally linked with MZT1:6NTE of the luminal bridge, suggesting that it may be part of the GCP6-NTE (data not shown), which was found to be the case in a recent study with higher resolution (GCP6 'belt' (229)). Apart from its interconnecting function, it has an interesting sterical implication. Following the GCP6 NTE from N- to C-terminus, electron density corresponding to the C-terminal end of the GCP6 belt points into the direction of the seam but is absent in the region of the actin-like protein. About 170 residues remain unresolved before the GCP6 NTE connects to the GCP6 core fold. Liu *et al.* (235) suggested an assembly model where the GCP6 NTE extends down the γTuRC luminal face over GCP4/GCP5 to reach the luminal bridge. An alternative model is that the unresolved GCP6 NTE residues continue to follow the direction into which the last resolved C-terminal residues of the GCP6 belt point towards, i.e. towards the γTuRC seam. The unresolved part of the GCP6 NTE may thereby contribute to the zig-zag element (**Figure 29A**) before connecting to the N-GRIP domain. Liu *et al.* (235) additionally claimed that the GCP6 insertion domain is necessary for γTuRC assembly. This has recently been questioned as GCP6 mutant lacking large parts of the insertion domain still promotes γTuRC assembly in human cells and rescues spindle defects associated with γTuRC integrity defects (130). The recombinant system now allows testing whether a γTuRC with truncated GCP6 can still assemble.

As mentioned above, an additional element connects the N-terminal GRIP domains of the adjacent $GCP5_{10}$, $GCP4_{11}$, and $GCP6_{12}$ at their bases, which could explain the stability of a GCP4/GCP5/GCP6 subcomplex observed after salt-mediated dissociation of γTuRC (9). A third, newly identified helical zig-zag element runs along the inner N-terminal surfaces

of GCP6$_{12}$, GCP2$_{13}$, and GCP3$_{14}$. This element could also be part of the GCP6-NTE or of the large GCP6 insertion, preceding the three C-terminal helices that we have assigned to this region. Alternatively, it may be formed by the NTE of GCP5. If the end protrusion is built by a MTZ1:5NTE unit as discussed above, then these zig-zag helices may connect it with the GCP5 N-GRIP domain.

Last, the remaining pair GCP2$_1$/GCP3$_2$ is engaged with the luminal actin-like protein, which, in turn, is in contact with the luminal bridge. Apart from stabilizing the γTuRC core structure, it remains an open question if the actin-like protein has additional roles when γTuRC nucleates microtubules. In all cryo-EM analyses including ours, the local resolution of the actin-like protein is comparably low compared to the surrounding elements of the luminal bridge or N-GRIP domains of γTuSCs. This argues for a more flexible binding of the actin-like protein, which may indicate that this portion of γTuRC could undergo conformational changes during nucleation. Addition of DNAseI to γTuRCs has been shown to inhibit microtubule nucleation (235). DNAseI binds actin at the pointed end (252), which in γTuRC localizes to where the actin-like protein is engaged with GCP3 and γ-tubulin in position 2. DNAseI treatment therefore may interfere with the stabilizing function of the luminal bridge. In this scenario, rather than being a direct effect on nucleation, the activity loss upon DNAseI addition may be caused by partial γTuRC disassembly. Thus, other experimental designs, such as including mutant actin in the coexpression system or reconstituting γTuRC from individual purified subcomponents, are needed to explore the function of actin.

The extensive interconnections between GCPs suggest that γTuRC assembly and stability may not primarily depend on lateral interactions between GRIP domains but also on hitherto underappreciated interactions of less conserved GCP regions and accessory proteins. Consistently, recombinant γTuSC had a propensity to self-associate but formed γTuRC-like rings only in the presence of cross-linker. The staples at the intra-γTuSC interfaces are unlikely to affect ring formation directly but may do so indirectly, by ensuring γTuSC integrity.

5.5 Implications for γTuRC-mediated microtubule nucleation

To establish a perfect microtubule template, the imperfectly aligned γ-tubulin molecules in γTuRC must undergo conformational changes to resemble a microtubule in cross-section. To achieve this, relatively small motions would be required in the symmetrical part of the γTuRC ring from positions 1 to 8. In contrast, the changes required in the asymmetrical part from positions 9 to 14 are substantial (235). In the specific case of GCP4 and GCP6, the angle between N-GRIP and C-GRIP domains known as 'kink' would need to be straightened. Compatible with this idea, comparison of the GCP4 structure in native γTuRC to the GCP4 structure determined by X-ray crystallography showed that GCP4 can exist both in a straight and kinked state, suggesting that the GCP core fold is inherently flexible and competent to undergo the required conformational changes (236). Phosphorylation has been suggested as a mechanism to induce changes in the kink angle, but direct experimental evidence is missing (96). Kink angle straightening could also contribute to increasing the helical pitch to match the microtubule lattice.

The seam of the microtubule lattice is a known driver of microtubule instability. Very recent work has provided direct evidence that the seam becomes less stable upon tubulin GTP hydrolysis (253). Specifically, the heterotypic α-β-tubulin lateral interaction at the seam seems to be destabilized after GTP hydrolysis. Thus, one hypothesis could be that γTuRC stabilizes tubulin interactions at the seam in order to promote nucleation. To do so, γTuRC could perhaps transiently inhibit tubulin GTP hydrolysis after recruitment, which would be the opposite of what is currently proposed to happen after γ-tubulin binds to α/β-tubulin heterodimers. This mechanism would be similar to microtubule growth from GMPCPP-stabilized seeds that adapt a GTP-like tubulin state (30, 33, 254). A requirement for promoting lattice-like contacts to stabilize tubulin interactions at the seam would underline the importance of γTuRCs to adopt a different conformation in the GCP4/GCP5/GCP6-part in order to grow a stable microtubule. Microtubules with capped γTuRC-capped minus-ends have been generated *in vitro* and imaged by EM (98, 239), but the low resolution did not allow any conclusion about the conformation of the GCP4/GCP5/GCP6-part.

Assuming additional factors can induce γTuRC conformational changes – how may these changes be brought about? An obvious possibility is that γTuRC activators such as

CDK5RAP2 can directly induce the required conformational changes. A short fragment of the CDK5RAP2 CM1 motif, that was used to purify native γTuRC, has recently been observed to be bound on the outside of the γTuRC cone. Here, two copies of the CDK5RAP2 CM1 peptide form a coiled coil dimer that is sandwiched between the $GCP2_{13}$ C-GRIP domain and a MZT2:2NTE unit, likely contributed by $GCP2_{13}$ (229) Surprisingly however, γTuRC bound to the 'activator' is found in an 'inactive' conformation that does not fit the microtubule symmetry. Thus, while some portion of a CDK5RAP2 dimer may bind at this position, this observation alone cannot explain the observed activation of microtubule nucleation by the CM1 domain in cells and in some cases also *in vitro* (113, 126, 135, 160). Other positions in γTuRC likely also have MZT2:2NTEs, so it remains possible that binding of multiple CDK5RAP2 dimers is required to change the conformation of γTuRC. If multiple copies of CDK5RAP2 can simultaneously bind γTuRC, it remains to be understood why the CDK5RAP2 CM1 dimer was only observed at position 13, and not at other positions. As this position is the only one in the γTuRC cone where GCP2 is adjacent to GCP6, one possibility is that unknown GCP6-associated features contribute to CM1 binding. Another clue comes from recent refinement of the budding yeast Spc110-γTuSC-spiral structure, that to date most closely resembles a microtubule in cross-section. Specifically, a previously unidentified Spc110 helix was found to additionally interact with GCP2 at the very same position that is bound by CDK5RAP2 CM1 in human γTuRC (255). Moreover, a short Spc110 coil protrudes out of this helix and makes contacts with the neighboring γTuSC, likely stabilizing a more closed γTuRC conformation. Corresponding regions CDK5RAP2 that have not been identified yet, could similarly stabilize a more closed conformation in vertebrate γTuRC. Having reconstituted a mutant γTuRC that lacks MZT2:NTE units provides a useful tool for structure-function studies to dissect the contributions of different CDK5RAP2 domains to a potential structural change in γTuRC.

Alternatively, such conformational changes may be brought about passively once a microtubule has formed on γTuRC (145). In this case, nucleation activity may not be stimulated by a conformational change in γTuRC but at the level of the nascent microtubule, by stabilizing factors or by the local availability of α/β-tubulin heterodimers. XMAP215 from *X. leavis* (CKAP5 in humans) has been suggested as a factor that can couple microtubule polymerase activity to the nucleation surface of γTuRC (134). Indeed,

XMAP215 was shown to directly bind γ-tubulin via a region at its C-terminus that is distinct from its tubulin binding TOG domains (134). However, if XMAP215 also binds γ-tubulin as part of γTuRC and whether the interaction also occurs in cells remains to be tested. One clue of how the XMAP215 family of microtubule polymerases are recruited by other factors comes from a study of the budding yeast XMAP215 family member Stu2. Zahm *et al.* (256) determined the structure of a highly conserved C-terminal helix in Stu2 bound to its kinetochore binding partners by X-ray crystallography. Interestingly, the Stu2 helix is embedded in coiled-coil structures formed by the other binding partners. Coiled-coils are also commonly found in centrosomal proteins, and indeed the same Stu2 domain is known to bind to Spc72 to regulate microtubule properties at Spc72-bound γ-tubulin complexes (163). Structurally somewhat similar to the Stu2 recruitment site, the coiled-coil formed by CM1 peptides localizes close to the nucleation surface, where tubulin-heterodimers are added during nucleation. Investigation of how XMAP215/CKAP5 may interact with γTuRC will be needed to understand the mechanistic details of their interplay during nucleation. Assuming a passive conformational change in γTuRC following tubulin addition promoted by such a nucleation helper, nucleation activity may also be modulated by tubulin isotypes that have been shown to differ in their polymerization behavior (39). This hypothesis could be tested in dynamic TIRF-based nucleation assays with reconstituted γTuRC, the nucleation helper (for example CKAP5) and testing different recombinantly produced tubulin isotypes.

What are the consequences of growing microtubules from γTuRC rather than without a template nucleator? Microtubules can be grown *in vitro* from purified tubulin including from microtubule seeds that are stabilized by small molecule tubulin binding agents. For many years it has been known that microtubules grown this way are highly flexible in protofilament number and can display lattice defects such as multiple seams or varying tubulin conformations (257, 258), an effect that can also be induced by addition of MAPs (43). In contrast, cells most commonly assemble 13 protofilament microtubules that display less defects (25, 258, 259). Nucleation of microtubules from γTuRC may directly contribute to these observations but direct experimental testing has been so far been difficult, in part due to low yields and challenging purifications of native γTuRC (160, 237). The methodological advance to produce γTuRC in high quantities with simplified purification procedures now lowers the barrier to biochemical bottom-up approaches

aiming to understand the interplay of nucleators and MAPs in influencing protofilament number, lattice symmetry, and plus-end dynamics. Such questions could be for addressed by for example nucleating microtubules from purified γTuRC and testing the effect of MAPs in functional *in vitro* assays, combined with structural biology approaches that are able to capture intermediate states of dynamic processes, such as cryo-EM.

The lack of recombinant γTuRC has hampered progress in understanding the nucleation mechanism for decades. Our current knowledge is derived almost entirely from studies of recombinant yeast γTuSC and *in vitro*–generated γTuSC oligomers with limited resemblance to γTuRC. Using RUVBL-mediated assembly, we have been able to overcome this limitation. Using recombinant γTuRC and γTuRC mutants in recently established single-molecule, total internal reflection fluorescence microscopy–based nucleation assays (237, 238) now pave the way for exciting new discoveries in the near future. This will not only include revealing the mechanism of γTuRC-mediated microtubule nucleation but also how disease-associated mutations in γTuRC components may affect microtubule nucleation (260–263)

6. Conclusions

The findings obtained during my doctorate support the following main conclusions:

- *H. sapiens* γTuRC can be reconstituted from a limited set of recombinant proteins using baculovirus-mediated coexpression in insect cells.
- The core subunits of *H. sapiens* γTuRC are γ-tubulin, GCP2, GCP3, GCP4, GCP5, GCP6, MZT1, MZT2 and actin.
- RUVBL is a γTuRC assembly factor in human cells and in the heterologous coexpression system.
- *H. sapiens* γTuSC is built from γ-tubulin, GCP2, GCP3, MZT1, MZT2.
- In human cells, γTuSC likely coexists with γTuRC.
- RUVBL interacts with γTuRC subcomplexes but is not part of fully assembled γTuRC.
- Recombinant purified γTuRC has microtubule nucleation activity.
- Recombinant purified γTuRC resembles native γTuRC as determined by its cryo-EM structure at ~4.0 Å resolution.
- MZT1 proteins and parts of the GCP3- and GCP6-NTE form structural units that can stabilize the higher-order γTuRC structure as part of the luminal bridge.
- Cryo-EM identifies staple elements in the GCP2-NTE that likely contribute to γTuSC integrity.
- Mutational analysis suggests that MZT1:3NTE and MZT2:2NTE units are dispensable for assembly of the γTuSC core structure.
- MZT2:2NTE units are dispensable for RUVBL-mediated assembly of the γTuRC core structure.

7. References

1. S. Forth, T. M. Kapoor, The mechanics of microtubule networks in cell division. *J Cell Biol* **216**, 1525–1531 (2017).

2. S. Meunier, I. Vernos, Microtubule assembly during mitosis – from distinct origins to distinct functions? *J Cell Sci* **125**, 2805–2814 (2012).

3. J. P. Caviston, E. L. F. Holzbaur, Microtubule motors at the intersection of trafficking and transport. *Trends Cell Biol* **16**, 530–537 (2006).

4. J. L. Ross, The impacts of molecular motor traffic jams. *Proc National Acad Sci* **109**, 5911–5912 (2012).

5. A. Sakakibara, R. Ando, T. Sapir, T. Tanaka, Microtubule dynamics in neuronal morphogenesis. *Open Biol* **3**, 130061 (2013).

6. J. Mathur, M. Hülskamp, Microtubules and Microfilaments in Cell Morphogenesis in Higher Plants. *Curr Biol* **12**, R669–R676 (2002).

7. L. Bonetta, Microtubules shape the cell. *J Cell Biology* **169**, 553–553 (2005).

8. B. P. Bouchet, A. Akhmanova, A. Ewald, Microtubules in 3D cell motility. *J Cell Sci* **130**, 39–50 (2017).

9. S. Etienne-Manneville, Microtubules in Cell Migration. *Cell Dev Biology* **29**, 471–499 (2012).

10. S. C. Goetz, K. V. Anderson, The primary cilium: a signalling centre during vertebrate development. *Nat Rev Genet* **11**, 331–344 (2010).

11. C. Dumontet, M. A. Jordan, Microtubule-binding agents: a dynamic field of cancer therapeutics. *Nat Rev Drug Discov* **9**, 790–803 (2010).

12. L. Pellegrini, A. Wetzel, S. Grannó, G. Heaton, K. Harvey, Back to the tubule: microtubule dynamics in Parkinson's disease. *Cell Mol Life Sci* **74**, 409–434 (2017).

13. J. N. Sleigh, A. M. Rossor, A. D. Fellows, A. P. Tosolini, G. Schiavo, Axonal transport and neurological disease. *Nat Rev Neurol* **15**, 691–703 (2019).

14. M. Lasser, J. Tiber, L. A. Lowery, The Role of the Microtubule Cytoskeleton in Neurodevelopmental Disorders. *Front Cell Neurosci* **12**, 165 (2018).

15. R. S. Schwartz, F. Hildebrandt, T. Benzing, N. Katsanis, Ciliopathies. *New Engl J Medicine* **364**, 1533–1543 (2011).

16. M. Lovera, J. Lüders, The ciliary impact of nonciliary gene mutations. *Trends Cell Biol* (2021) https:/doi.org/10.1016/j.tcb.2021.06.001.

17. M. A. Jordan, L. Wilson, Microtubules as a target for anticancer drugs. *Nat Rev Cancer* **4**, 253–265 (2004).

18. A. L. Risinger, F. J. Giles, S. L. Mooberry, Microtubule dynamics as a target in oncology. *Cancer Treat Rev* **35**, 255–261 (2009).

19. S. Florian, T. J. Mitchison, The Mitotic Spindle, Methods and Protocols. *Methods Mol Biology* **1413**, 403–421 (2016).

20. E. L. Schwartz, Antivascular Actions of Microtubule-Binding Drugs. *Clin Cancer Res* **15**, 2594–2601 (2009).

21. D. Bates, A. Eastman, Microtubule destabilising agents: far more than just antimitotic anticancer drugs. *Brit J Clin Pharmaco* **83**, 255–268 (2017).

22. S. A. Lewis, G. Tian, I. E. Vainberg, N. J. Cowan, Chaperonin-mediated folding of actin and tubulin. *J Cell Biology* **132**, 1–4 (1996).

23. J. J. Kelly, *et al.*, Snapshots of actin and tubulin folding inside the TRiC chaperonin. *Biorxiv*, 2021.03.26.436673 (2021).

24. E. Nogales, S. G. Wolf, K. H. Downing, Structure of the αβ tubulin dimer by electron crystallography. *Nature* **391**, 199–203 (1998).

25. L. Evans, T. Mitchison, M. Kirschner, Influence of the centrosome on the structure of nucleated microtubules. *J Cell Biology* **100**, 1185–1191 (1985).

26. E. Nogales, Structural Insights into Microtubule Function. *Annu Rev Bioph Biom* **30**, 397–420 (2001).

27. T. Mitchison, Localization of an exchangeable GTP binding site at the plus end of microtubules. *Science* **261**, 1044–1047 (1993).

28. J. Fan, A. D. Griffiths, A. Lockhart, R. A. Cross, L. A. Amos, Microtubule Minus Ends can be Labelled with a Phage Display Antibody Specific to Alpha-Tubulin. *J Mol Biol* **259**, 325–330 (1996).

29. T. Mitchison, M. Kirschner, Dynamic instability of microtubule growth. *Nature* **312**, 237–242 (1984).

30. A. A. Hyman, S. Salser, D. N. Drechsel, N. Unwin, T. J. Mitchison, Role of GTP hydrolysis in microtubule dynamics: information from a slowly hydrolyzable analogue, GMPCPP. *Mol Biol Cell* **3**, 1155–1167 (1992).

31. J. Roostalu, *et al.*, The speed of GTP hydrolysis determines GTP cap size and controls microtubule stability. *Elife* **9**, e51992 (2020).

32. A. Nawrotek, M. Knossow, B. Gigant, The Determinants That Govern Microtubule Assembly from the Atomic Structure of GTP-Tubulin. *J Mol Biol* **412**, 35–42 (2011).

33. G. M. Alushin, *et al.*, High-Resolution Microtubule Structures Reveal the Structural Transitions in αβ-Tubulin upon GTP Hydrolysis. *Cell* **157**, 1117–1129 (2014).

34. R. A. Walker, *et al.*, Dynamic instability of individual microtubules analyzed by video light microscopy: rate constants and transition frequencies. *J Cell Biology* **107**, 1437–1448 (1988).

35. M. Caplow, R. L. Ruhlen, J. Shanks, The free energy for hydrolysis of a microtubule-bound nucleotide triphosphate is near zero: all of the free energy for hydrolysis is stored in the microtubule lattice. *J Cell Biology* **127**, 779–788 (1994).

36. M. Knossow, V. Campanacci, L. A. Khodja, B. Gigant, The mechanism of tubulin assembly into microtubules: insights from structural studies. *Iscience* **23**, 101511 (2020).

37. C. Janke, M. M. Magiera, The tubulin code and its role in controlling microtubule properties and functions. *Nat Rev Mol Cell Bio* **21**, 307–326 (2020).

38. A. Roll-Mecak, The Tubulin Code in Microtubule Dynamics and Information Encoding. *Dev Cell* **54**, 7–20 (2020).

39. A. Vemu, *et al.*, Structure and Dynamics of Single-isoform Recombinant Neuronal Human Tubulin. *The Journal of biological chemistry* **291**, 12907–12915 (2016).

40. A. Roll-Mecak, How cells exploit tubulin diversity to build functional cellular microtubule mosaics. *Curr Opin Cell Biol* **56**, 102–108 (2019).

41. J. Chen, *et al.*, α-tubulin tail modifications regulate microtubule stability through selective effector recruitment, not changes in intrinsic polymer dynamics. *Dev Cell* (2021) https:/doi.org/10.1016/j.devcel.2021.05.005.

42. E. Prezel, *et al.*, Tau can switch microtubule network organizations: from random networks to dynamic and stable bundles. *Mol Biol Cell* **29**, 154–165 (2018).

43. A. des Georges, *et al.*, Mal3, the Schizosaccharomyces pombe homolog of EB1, changes the microtubule lattice. *Nat Struct Mol Biol* **15**, 1102–1108 (2008).

44. A. Akhmanova, M. O. Steinmetz, Control of microtubule organization and dynamics: two ends in the limelight. *Nat Rev Mol Cell Bio* **16**, 711–726 (2015).

45. J. Al-Bassam, F. Chang, Regulation of microtubule dynamics by TOG-domain proteins XMAP215/Dis1 and CLASP. *Trends Cell Biol* **21**, 604–614 (2011).

46. X. Su, R. Ohi, D. Pellman, Move in for the kill: motile microtubule regulators. *Trends Cell Biol* **22**, 567–575 (2012).

47. A. Roll-Mecak, F. J. McNally, Microtubule-severing enzymes. *Curr Opin Cell Biol* **22**, 96–103 (2010).

48. A. Vemu, *et al.*, Severing enzymes amplify microtubule arrays through lattice GTP-tubulin incorporation. *Science (New York, N.Y.)* **361**, eaau1504 (2018).

49. J. Roostalu, N. I. Cade, T. Surrey, Complementary activities of TPX2 and chTOG constitute an efficient importin-regulated microtubule nucleation module. *Nature cell biology* **17**, 1422–1434 (2015).

50. M. Wieczorek, S. Bechstedt, S. Chaaban, G. J. Brouhard, Microtubule-associated proteins control the kinetics of microtubule nucleation. *Nat Cell Biol* **17**, 907–916 (2015).

51. R. Zhang, J. Roostalu, T. Surrey, E. Nogales, Structural insight into TPX2-stimulated microtubule assembly. *Elife* **6**, e30959 (2017).

52. K. Jiang, *et al.*, Microtubule Minus-End Stabilization by Polymerization-Driven CAMSAP Deposition. *Dev Cell* **28**, 295–309 (2014).

53. K. Jiang, *et al.*, Microtubule minus-end regulation at spindle poles by an ASPM–katanin complex. *Nat Cell Biol* **19**, 480–492 (2017).

54. R. D. Vale, The Molecular Motor Toolbox for Intracellular Transport. *Cell* **112**, 467–480 (2003).

55. G. Bhabha, G. T. Johnson, C. M. Schroeder, R. D. Vale, How Dynein Moves Along Microtubules. *Trends Biochem Sci* **41**, 94–105 (2016).

56. P. Bieling, I. A. Telley, T. Surrey, A Minimal Midzone Protein Module Controls Formation and Length of Antiparallel Microtubule Overlaps. *Cell* **142**, 420–432 (2010).

57. Z. Lansky, *et al.*, Diffusible Crosslinkers Generate Directed Forces in Microtubule Networks. *Cell* **160**, 1159–1168 (2015).

58. C. Mollinari, *et al.*, PRC1 is a microtubule binding and bundling protein essential to maintain the mitotic spindle midzone. *J Cell Biology* **157**, 1175–1186 (2002).

59. J. Luders, T. Stearns, Microtubule-organizing centres: a re-evaluation. *Nature reviews. Molecular cell biology* **8**, 161–167 (2007).

60. N. Teixido-Travesa, J. Roig, J. Luders, The where, when and how of microtubule nucleation - one ring to rule them all. *Journal of cell science* **125**, 4445–4456 (2012).

61. A. Akhmanova, M. O. Steinmetz, Microtubule minus-end regulation at a glance. *Journal of cell science* **132** (2019).

62. E. A. Nigg, A. J. Holland, Once and only once: mechanisms of centriole duplication and their deregulation in disease. *Nature reviews. Molecular cell biology* **139**, 663 (2018).

63. R. Habedanck, Y.-D. Stierhof, C. J. Wilkinson, E. A. Nigg, The Polo kinase Plk4 functions in centriole duplication. *Nat Cell Biol* **7**, 1140–1146 (2005).

64. Y. L. Wong, *et al.*, Reversible centriole depletion with an inhibitor of Polo-like kinase 4. *Science* **348**, 1155–1160 (2015).

65. R. Basto, *et al.*, Flies without Centrioles. *Cell* **125**, 1375–1386 (2006).

66. J.-H. Sir, *et al.*, Loss of centrioles causes chromosomal instability in vertebrate somatic cells. *J Cell Biology* **203**, 747–756 (2013).

67. A. Pimenta-Marques, M. Bettencourt-Dias, Pericentriolar material. *Curr Biol* **30**, R687–R689 (2020).

68. J. B. Woodruff, O. Wueseke, A. A. Hyman, Pericentriolar material structure and dynamics. *Philosophical Transactions Royal Soc B Biological Sci* **369**, 20130459 (2014).

69. M. Bauer, F. Cubizolles, A. Schmidt, E. A. Nigg, Quantitative analysis of human centrosome architecture by targeted proteomics and fluorescence imaging. *Embo J* **35**, 2152–2166 (2016).

70. S. Lawo, M. Hasegan, G. D. Gupta, L. Pelletier, Subdiffraction imaging of centrosomes reveals higher-order organizational features of pericentriolar material. *Nat Cell Biol* **14**, 1148–1158 (2012).

71. J. Paz, J. Lüders, Microtubule-Organizing Centers: Towards a Minimal Parts List. *Trends Cell Biol* **28**, 176–187 (2018).

72. C. E. Oakley, B. R. Oakley, Identification of γ-tubulin, a new member of the tubulin superfamily encoded by mipA gene of Aspergillus nidulans. *Nature* **338**, 662–664 (1989).

73. M. A. Martin, S. A. Osmani, B. R. Oakley, The role of gamma-tubulin in mitotic spindle formation and cell cycle progression in Aspergillus nidulans. *J Cell Sci* **110**, 623–633 (1997).

74. T. Horio, *et al.*, The fission yeast gamma-tubulin is essential for mitosis and is localized at microtubule organizing centers. *J Cell Sci* **99**, 693–700 (1991).

75. S. G. Sobel, M. Snyder, A highly divergent gamma-tubulin gene is essential for cell growth and proper microtubule organization in Saccharomyces cerevisiae. *J Cell Biology* **131**, 1775–1788 (1995).

76. Y. Zheng, M. K. Jung, B. R. Oakley, γ-Tubulin is present in Drosophila melanogaster and homo sapiens and is associated with the centrosome. *Cell* **65**, 817–823 (1991).

77. H. C. Joshi, M. J. Palacios, L. McNamara, D. W. Cleveland, γ-Tubulin is a centrosomal protein required for cell cycle-dependent microtubule nucleation. *Nature* **356**, 80–83 (1992).

78. T. Horio, B. R. Oakley, Human gamma-tubulin functions in fission yeast. *J Cell Biology* **126**, 1465–1473 (1994).

79. M. Félix, C. Antony, M. Wright, B. Maro, Centrosome assembly in vitro: role of gamma-tubulin recruitment in Xenopus sperm aster formation. *J Cell Biology* **124**, 19–31 (1994).

80. T. Stearns, M. Kirschner, In vitro reconstitution of centrosome assembly and function: The central role of γ-tubulin. *Cell* **76**, 623–637 (1994).

81. D. Job, O. Valiron, B. Oakley, Microtubule nucleation. *Curr Opin Cell Biol* **15**, 111–117 (2003).

82. A. Khodjakov, C. L. Rieder, The Sudden Recruitment of γ-Tubulin to the Centrosome at the Onset of Mitosis and Its Dynamic Exchange Throughout the Cell Cycle, Do Not Require Microtubules. *J Cell Biol* **146**, 585–596 (1999).

83. M. Piehl, U. S. Tulu, P. Wadsworth, L. Cassimeris, Centrosome maturation: Measurement of microtubule nucleation throughout the cell cycle by using GFP-tagged EB1. *P Natl Acad Sci Usa* **101**, 1584–1588 (2004).

84. T. Hart, *et al.*, High-Resolution CRISPR Screens Reveal Fitness Genes and Genotype-Specific Cancer Liabilities. *Cell* **163**, 1515–1526 (2015).

85. V. A. Blomen, *et al.*, Gene essentiality and synthetic lethality in haploid human cells. *Science* **350**, 1092–1096 (2015).

86. T. Wang, *et al.*, Identification and characterization of essential genes in the human genome. *Science* **350**, 1096–1101 (2015).

87. A. Yilmaz, M. Peretz, A. Aharony, I. Sagi, N. Benvenisty, Defining essential genes for human pluripotent stem cells by CRISPR–Cas9 screening in haploid cells. *Nat Cell Biol* **20**, 610–619 (2018).

88. C. E. Sunkel, R. Gomes, P. Sampaio, J. Perdigão, C. González, Gamma-tubulin is required for the structure and function of the microtubule organizing centre in Drosophila neuroblasts. *Embo J* **14**, 28–36 (1995).

89. A. Spang, S. Geissler, K. Grein, E. Schiebel, gamma-Tubulin-like Tub4p of Saccharomyces cerevisiae is associated with the spindle pole body substructures that organize microtubules and is required for mitotic spindle formation. *J Cell Biology* **134**, 429–441 (1996).

90. F. J. Ahmad, H. C. Joshi, V. E. Centonze, P. W. Baas, Inhibition of microtubule nucleation at the neuronal centrosome compromises axon growth. *Neuron* **12**, 271–280 (1994).

91. B. R. Oakley, γ-Tubulin. *Current Topics in Developmental Biology* **49**, 27–54 (1999).

92. L. G. Marschall, R. L. Jeng, J. Mulholland, T. Stearns, Analysis of Tub4p, a yeast gamma-tubulin-like protein: implications for microtubule-organizing center function. *J Cell Biology* **134**, 443–454 (1996).

93. H. Aldaz, L. M. Rice, T. Stearns, D. A. Agard, Insights into microtubule nucleation from the crystal structure of human gamma-tubulin. *Nature* **435**, 523–527 (2005).

94. H. P. Erickson, γ-tubulin nucleation: template or protofilament? *Nat Cell Biol* **2**, E93–E95 (2000).

95. J. M. Kollman, J. K. Polka, A. Zelter, T. N. Davis, D. A. Agard, Microtubule nucleating gamma-TuSC assembles structures with 13-fold microtubule-like symmetry. *Nature* **466**, 879–882 (2010).

96. J. M. Kollman, *et al.*, Ring closure activates yeast γTuRC for species-specific microtubule nucleation. *Nature structural & molecular biology* **22**, 132–137 (2015).

97. M. Moritz, M. B. Braunfeld, J. W. Sedat, B. Alberts, D. A. Agard, Microtubule nucleation by gamma-tubulin-containing rings in the centrosome. *Nature* **378**, 638–640 (1995).
98. Y. Zheng, M. L. Wong, B. Alberts, T. Mitchison, Nucleation of microtubule assembly by a gamma-tubulin-containing ring complex. *Nature* **378**, 578–583 (1995).

99. M. Moritz, Y. Zheng, B. M. Alberts, K. Oegema, Recruitment of the γ-Tubulin Ring Complex to Drosophila Salt-stripped Centrosome Scaffolds. *J Cell Biology* **142**, 775–786 (1998).

100. S. M. Murphy, L. Urbani, T. Stearns, The Mammalian γ-Tubulin Complex Contains Homologues of the Yeast Spindle Pole Body Components Spc97p and Spc98p. *J Cell Biol* **141**, 663–674 (1998).

101. S. M. Murphy, *et al.*, GCP5 and GCP6: Two New Members of the Human γ-Tubulin Complex. *Mol Biol Cell* **12**, 3340–3352 (2001).

102. K. Oegema, *et al.*, Characterization of Two Related Drosophila γ-tubulin Complexes that Differ in Their Ability to Nucleate Microtubules. *J Cell Biology* **144**, 721–733 (1999).

103. M. Moritz, M. B. Braunfeld, V. Guenebaut, J. Heuser, D. A. Agard, Structure of the gamma-tubulin ring complex: a template for microtubule nucleation. *Nature cell biology* **2**, 365–370 (2000).

104. C. Wiese, Y. Zheng, A new function for the gamma-tubulin ring complex as a microtubule minus-end cap. *Nature cell biology* **2**, 358–364 (2000).

105. A. Anders, K. E. Sawin, Microtubule stabilization in vivo by nucleation-incompetent gamma-tubulin complex. *Journal of cell science* **124**, 1207–1213 (2011).

106. A. Bouissou, *et al.*, {gamma}-Tubulin ring complexes regulate microtubule plus end dynamics. *The Journal of cell biology* **187**, 327–334 (2009).

107. M.-H. Remy, A. Merdes, L. Gregory-Pauron, Assembly of gamma-tubulin ring complexes: implications for cell biology and disease. *Progress in molecular biology and translational science* **117**, 511–530 (2013).

108. N. Izumi, K. Fumoto, S. Izumi, A. Kikuchi, GSK-3beta regulates proper mitotic spindle formation in cooperation with a component of the gamma-tubulin ring complex, GCP5. *The Journal of biological chemistry* **283**, 12981–12991 (2008).

109. F. Schnorrer, S. Luschnig, I. Koch, C. Nüsslein-Volhard, γ-Tubulin37C and γ-tubulin ring complex protein 75 Are Essential for bicoid RNA Localization during Drosophila Oogenesis. *Dev Cell* **3**, 685–696 (2002).

110. C. Vérollet, *et al.*, Drosophila melanogaster γ-TuRC is dispensable for targeting γ-tubulin to the centrosome and microtubule nucleation. *J Cell Biology* **172**, 517–528 (2006).

111. N. Vogt, I. Koch, H. Schwarz, F. Schnorrer, C. Nusslein-Volhard, The gammaTuRC components Grip75 and Grip128 have an essential microtubule-anchoring function in the Drosophila germline. *Development (Cambridge, England)* **133**, 3963–3972 (2006).

112. L. Zhang, T. J. Keating, A. Wilde, G. G. Borisy, Y. Zheng, The Role of Xgrip210 in γ-Tubulin Ring Complex Assembly and Centrosome Recruitment. *J Cell Biology* **151**, 1525–1536 (2000).

113. R. R. Cota, *et al.*, MZT1 regulates microtubule nucleation by linking gammaTuRC assembly to adapter-mediated targeting and activation. *Journal of cell science* **130**, 406–419 (2017).

114. M. Knop, G. Pereira, S. Geissler, K. Grein, E. Schiebel, The spindle pole body component Spc97p interacts with the γ-tubulin of Saccharomyces cerevisiae and functions in microtubule organization and spindle pole body duplication. *Embo J* **16**, 1550–1564 (1997).

115. L. Vardy, T. Toda, The fission yeast γ-tubulin complex is required in G1 phase and is a component of the spindle assembly checkpoint. *Embo J* **19**, 6098–6111 (2000).

116. A. Anders, P. C. C. Lourenço, K. E. Sawin, Noncore components of the fission yeast gamma-tubulin complex. *Molecular biology of the cell* **17**, 5075–5093 (2006).

117. Y. Xiong, B. R. Oakley, In vivo analysis of the functions of γ-tubulin-complex proteins. *J Cell Sci* **122**, 4218–4227 (2009).

118. A. Fujita, L. Vardy, M. A. Garcia, T. Toda, A Fourth Component of the Fission Yeast γ-Tubulin Complex, Alp16, Is Required for Cytoplasmic Microtubule Integrity and Becomes Indispensable When γ-Tubulin Function Is Compromised. *Mol Biol Cell* **13**, 2360–2373 (2002).

119. S. Venkatram, *et al.*, Identification and Characterization of Two Novel Proteins Affecting Fission Yeast γ-tubulin Complex Function. *Mol Biol Cell* **15**, 2287–2301 (2004).

120. A. Dammermann, *et al.*, Centriole Assembly Requires Both Centriolar and Pericentriolar Material Proteins. *Dev Cell* **7**, 815–829 (2004).

121. N. Schweizer, J. Lüders, From tip to toe – dressing centrioles in γTuRC. *J Cell Sci* **134** (2021).

122. N. Teixido-Travesa, *et al.*, The gammaTuRC revisited: a comparative analysis of interphase and mitotic human gammaTuRC redefines the set of core components and identifies the novel subunit GCP8. *Molecular biology of the cell* **21**, 3963–3972 (2010).

123. V. Guillet, *et al.*, Crystal structure of gamma-tubulin complex protein GCP4 provides insight into microtubule nucleation. *Nature structural & molecular biology* **18**, 915–919 (2011).

124. D. B. N. Vinh, J. W. Kern, W. O. Hancock, J. Howard, T. N. Davis, Reconstitution and characterization of budding yeast gamma-tubulin complex. *Molecular biology of the cell* **13**, 1144–1157 (2002).

125. R. N. Gunawardane, *et al.*, Characterization and Reconstitution of Drosophila γ-Tubulin Ring Complex Subunits. *J Cell Biology* **151**, 1513–1524 (2000).
126. Y.-K. Choi, P. Liu, S. K. Sze, C. Dai, R. Z. Qi, CDK5RAP2 stimulates microtubule nucleation by the gamma-tubulin ring complex. *The Journal of cell biology* **191**, 1089–1095 (2010).

127. J. Luders, U. K. Patel, T. Stearns, GCP-WD is a gamma-tubulin targeting factor required for centrosomal and chromatin-mediated microtubule nucleation. *Nature cell biology* **8**, 137–147 (2006).

128. L. Haren, *et al.*, NEDD1-dependent recruitment of the gamma-tubulin ring complex to the centrosome is necessary for centriole duplication and spindle assembly. *The Journal of cell biology* **172**, 505–515 (2006).

129. D. Farache, *et al.*, Functional Analysis of gamma-Tubulin Complex Proteins Indicates Specific Lateral Association via Their N-terminal Domains. *The Journal of biological chemistry* **291**, 23112–23125 (2016).

130. L. Haren, D. Farache, L. Emorine, A. Merdes, A stable sub-complex between GCP4, GCP5 and GCP6 promotes the assembly of γ-tubulin ring complexes. *J Cell Sci* **133**, jcs244368 (2020).

131. M. Batzenschlager, *et al.*, The GIP gamma-tubulin complex-associated proteins are involved in nuclear architecture in Arabidopsis thaliana. *Front Plant Sci* **4**, 480 (2013).

132. N. Janski, E. Herzog, A. Schmit, Identification of a novel small Arabidopsis protein interacting with gamma-tubulin complex protein 3. *Cell Biol Int* **32**, 546–548 (2008).

133. J. R. A. Hutchins, *et al.*, Systematic analysis of human protein complexes identifies chromosome segregation proteins. *Science (New York, N.Y.)* **328**, 593–599 (2010).

134. A. Thawani, R. S. Kadzik, S. Petry, XMAP215 is a microtubule nucleation factor that functions synergistically with the γ-tubulin ring complex. *Nature cell biology* **20**, 575–585 (2018).

135. T.-C. Lin, *et al.*, MOZART1 and gamma-tubulin complex receptors are both required to turn gamma-TuSC into an active microtubule nucleation template. *The Journal of cell biology* **215**, 823–840 (2016).

136. D. K. Dhani, *et al.*, Mzt1/Tam4, a fission yeast MOZART1 homologue, is an essential component of the gamma-tubulin complex and directly interacts with GCP3(Alp6). *Molecular biology of the cell* **24**, 3337–3349 (2013).

137. H. Masuda, R. Mori, M. Yukawa, T. Toda, Fission yeast MOZART1/Mzt1 is an essential γ-tubulin complex component required for complex recruitment to the microtubule organizing center, but not its assembly. *Mol Biol Cell* **24**, 2894–2906 (2013).

138. M. Nakamura, *et al.*, Arabidopsis GCP3-interacting protein 1/MOZART 1 is an integral component of the gamma-tubulin-containing microtubule nucleating complex. *The Plant journal : for cell and molecular biology* **71**, 216–225 (2012).

139. M. D. Sallee, J. C. Zonka, T. D. Skokan, B. C. Raftrey, J. L. Feldman, Tissue-specific degradation of essential centrosome components reveals distinct microtubule populations at microtubule organizing centers. *Plos Biol* **16**, e2005189 (2018).

140. S. L. Leong, *et al.*, Reconstitution of Microtubule Nucleation In Vitro Reveals Novel Roles for Mzt1. *Current biology : CB* **29**, 2199-2207.e10 (2019).

141. C. A. Tovey, *et al.*, γ-TuRC Heterogeneity Revealed by Analysis of Mozart1. *Curr Biol* **28**, 2314-2323.e6 (2018).

142. C. D. Cukier, *et al.*, NMR secondary structure and interactions of recombinant human MOZART1 protein, a component of the gamma-tubulin complex. *Protein science : a publication of the Protein Society* **26**, 2240–2248 (2017).

143. A. Bilitou, J. Watson, A. Gartner, S. Ohnuma, The NM23 family in development. *Mol Cell Biochem* **329**, 17–33 (2009).

144. P. Liu, Y.-K. Choi, R. Z. Qi, NME7 is a functional component of the γ-tubulin ring complex. *Molecular biology of the cell* **25**, 2017–2025 (2014).

145. A. Thawani, *et al.*, The transition state and regulation of γ-TuRC-mediated microtubule nucleation revealed by single molecule microscopy. *Elife* **9**, e54253 (2020).

146. A. Grassadonia, *et al.*, 90K (Mac-2 BP) and galectins in tumor progression and metastasis. *Glycoconjugate J* **19**, 551–556 (2002).

147. M.-L. Fogeron, *et al.*, LGALS3BP regulates centriole biogenesis and centrosome hypertrophy in cancer cells. *Nature communications* **4**, 1531 (2013).

148. H. Bouguenina, *et al.*, EB1-binding-myomegalin protein complex promotes centrosomal microtubules functions. *Proceedings of the National Academy of Sciences of the United States of America* **114**, E10687–E10696 (2017).

149. T. Lin, A. Neuner, E. Schiebel, Targeting of gamma-tubulin complexes to microtubule organizing centers: conservation and divergence. *Trends in cell biology* **25**, 296–307 (2015).

150. L. Liu, C. Wiese, Xenopus NEDD1 is required for microtubule organization in Xenopus egg extracts. *Journal of cell science* **121**, 578–589 (2008).

151. W. Ma, C. Baumann, M. M. Viveiros, NEDD1 is crucial for meiotic spindle stability and accurate chromosome segregation in mammalian oocytes. *Dev Biol* **339**, 439–450 (2010).

152. J. A. Manning, S. Shalini, J. M. Risk, C. L. Day, S. Kumar, A Direct Interaction with NEDD1 Regulates γ-Tubulin Recruitment to the Centrosome. *Plos One* **5**, e9618 (2010).

153. S. Lawo, *et al.*, HAUS, the 8-Subunit Human Augmin Complex, Regulates Centrosome and Spindle Integrity. *Curr Biol* **19**, 816–826 (2009).

154. R. Uehara, *et al.*, The augmin complex plays a critical role in spindle microtubule generation for mitotic progression and cytokinesis in human cells. *Proceedings of the National Academy of Sciences of the United States of America* **106**, 6998–7003 (2009).

155. H. Zhu, J. A. Coppinger, C.-Y. Jang, J. R. Yates, G. Fang, FAM29A promotes microtubule amplification via recruitment of the NEDD1–γ-tubulin complex to the mitotic spindle. *J Cell Biology* **183**, 835–848 (2008).

156. H. Zhu, K. Fang, G. Fang, FAM29A, a target of Plk1 regulation, controls the partitioning of NEDD1 between the mitotic spindle and the centrosomes. *Journal of cell science* **122**, 2750–2759 (2009).

157. A. Muroyama, L. Seldin, T. Lechler, Divergent regulation of functionally distinct γ-tubulin complexes during differentiation. *The Journal of cell biology* **213**, 679–692 (2016).

158. R. N. Gunawardane, O. C. Martin, Y. Zheng, Characterization of a new gammaTuRC subunit with WD repeats. *Molecular biology of the cell* **14**, 1017–1026 (2003).

159. L. Truebestein, T. A. Leonard, Coiled-coils: The long and short of it. *Bioessays* **38**, 903–916 (2016).

160. Y.-K. Choi, R. Z. Qi, Assaying microtubule nucleation by the γ-tubulin ring complex. *Methods in enzymology* **540**, 119–130 (2014).

161. M. Takahashi, A. Yamagiwa, T. Nishimura, H. Mukai, Y. Ono, Centrosomal proteins CG-NAP and kendrin provide microtubule nucleation sites by anchoring gamma-tubulin ring complex. *Molecular biology of the cell* **13**, 3235–3245 (2002).

162. W. C. Zimmerman, J. Sillibourne, J. Rosa, S. J. Doxsey, Mitosis-specific Anchoring of γ Tubulin Complexes by Pericentrin Controls Spindle Organization and Mitotic Entry. *Mol Biol Cell* **15**, 3642–3657 (2004).

163. T. Usui, H. Maekawa, G. Pereira, E. Schiebel, The XMAP215 homologue Stu2 at yeast spindle pole bodies regulates microtubule dynamics and anchorage. *Embo J* **22**, 4779–4793 (2003).

164. E. M. Lynch, L. M. Groocock, W. E. Borek, K. E. Sawin, Activation of the γ-Tubulin Complex by the Mto1/2 Complex. *Curr Biol* **24**, 896–903 (2014).

165. H. C. Thakur, *et al.*, Architecture of the Mto1/2 microtubule nucleation complex. *Biorxiv*, 754457 (2019).

166. F. U. Hartl, A. Bracher, M. Hayer-Hartl, Molecular chaperones in protein folding and proteostasis. *Nature* **475**, 324–332 (2011).

167. R. A. Laskey, B. M. Honda, A. D. Mills, J. T. Finch, Nucleosomes are assembled by an acidic protein which binds histones and transfers them to DNA. *Nature* **275**, 416–420 (1978).

168. O. G. Berg, P. H. von Hippel, Diffusion-Controlled Macromolecular Interactions. *Annu Rev Biophys Bio* **14**, 131–158 (1985).

169. R. J. Ellis, A. P. Minton, Protein aggregation in crowded environments. *Biol Chem* **387**, 485–497 (2006).

170. R. J. Ellis, Macromolecular crowding: obvious but underappreciated. *Trends Biochem Sci* **26**, 597–604 (2001).

171. S. B. Zimmerman, A. P. Minton, Macromolecular Crowding: Biochemical, Biophysical, and Physiological Consequences. *Annu Rev Bioph Biom* **22**, 27–65 (1993).

172. H. Zhou, Protein folding and binding in confined spaces and in crowded solutions. *J Mol Recognit* **17**, 368–375 (2004).

173. A. Chari, U. Fischer, Cellular strategies for the assembly of molecular machines. *Trends Biochem Sci* **35**, 676–683 (2010).

174. R. J. Ellis, Assembly chaperones: a perspective. *Philosophical Transactions Royal Soc B Biological Sci* **368**, 20110398 (2013).

175. F. U. Hartl, M. Hayer-Hartl, Molecular Chaperones in the Cytosol: from Nascent Chain to Folded Protein. *Science* **295**, 1852–1858 (2002).

176. D. Balchin, M. Hayer-Hartl, F. U. Hartl, In vivo aspects of protein folding and quality control. *Science* **353**, aac4354 (2016).

177. Y. E. Kim, M. S. Hipp, A. Bracher, M. Hayer-Hartl, F. U. Hartl, Molecular Chaperone Functions in Protein Folding and Proteostasis. *Annu Rev Biochem* **82**, 323–355 (2013).

178. A. Borgia, *et al.*, Transient misfolding dominates multidomain protein folding. *Nat Commun* **6**, 8861 (2015).

179. D. B. Vinh, D. G. Drubin, A yeast TCP-1-like protein is required for actin function in vivo. *Proc National Acad Sci* **91**, 9116–9120 (1994).

180. M. B. Yaffe, *et al.*, TCP1 complex is a molecular chaperone in tubulin biogenesis. *Nature* **358**, 245–248 (1992).

181. R. Melki, I. Vainberg, R. Chow, N. Cowan, Chaperonin-mediated folding of vertebrate actin-related protein and gamma-tubulin. *J Cell Biology* **122**, 1301–1310 (1993).

182. T. Lopez, K. Dalton, J. Frydman, The Mechanism and Function of Group II Chaperonins. *J Mol Biol* **427**, 2919–2930 (2015).

183. D. Gestaut, *et al.*, The Chaperonin TRiC/CCT Associates with Prefoldin through a Conserved Electrostatic Interface Essential for Cellular Proteostasis. *Cell* **177**, 751-765.e15 (2019).

184. W. Gartner, *et al.*, The ATP-dependent helicase RUVBL1/TIP49a associates with tubulin during mitosis. *Cell Motil Cytoskel* **56**, 79–93 (2003).

185. D. Ducat, S.-I. Kawaguchi, H. Liu, J. R. 3rd Yates, Y. Zheng, Regulation of microtubule assembly and organization in mitosis by the AAA+ ATPase Pontin. *Molecular biology of the cell* **19**, 3097–3110 (2008).

186. W. A. Houry, E. Bertrand, B. Coulombe, The PAQosome, an R2TP-Based Chaperone for Quaternary Structure Formation. *Trends Biochem Sci* **43**, 4–9 (2018).

187. M. I. Dauden, A. López-Perrote, O. Llorca, RUVBL1–RUVBL2 AAA-ATPase: a versatile scaffold for multiple complexes and functions. *Curr Opin Struc Biol* **67**, 78–85 (2021).

188. P. M. Matias, S. Gorynia, P. Donner, M. A. Carrondo, Crystal Structure of the Human AAA+ Protein RuvBL1*. *J Biol Chem* **281**, 38918–38929 (2006).

189. S. T. N. Silva, *et al.*, X-ray structure of full-length human RuvB-Like 2 – mechanistic insights into coupling between ATP binding and mechanical action. *Sci Rep-uk* **8**, 13726 (2018).

190. N. Silva-Martin, *et al.*, The Combination of X-Ray Crystallography and Cryo-Electron Microscopy Provides Insight into the Overall Architecture of the Dodecameric Rvb1/Rvb2 Complex. *Plos One* **11**, e0146457 (2016).

191. E. Torreira, *et al.*, Architecture of the Pontin/Reptin Complex, Essential in the Assembly of Several Macromolecular Complexes. *Structure* **16**, 1511–1520 (2008).

192. C. A. Ewens, *et al.*, Architecture and Nucleotide-Dependent Conformational Changes of the Rvb1-Rvb2 AAA+ Complex Revealed by Cryoelectron Microscopy. *Structure* **24**, 657–666 (2016).

193. N. Izumi, *et al.*, AAA+ Proteins RUVBL1 and RUVBL2 Coordinate PIKK Activity and Function in Nonsense-Mediated mRNA Decay. *Sci Signal* **3**, ra27–ra27 (2010).

194. A. Magalska, *et al.*, RuvB-like ATPases Function in Chromatin Decondensation at the End of Mitosis. *Dev Cell* **31**, 305–318 (2014).

195. S. Gorynia, *et al.*, Structural and functional insights into a dodecameric molecular machine – The RuvBL1/RuvBL2 complex. *J Struct Biol* **176**, 279–291 (2011).

196. K. Lakomek, G. Stoehr, A. Tosi, M. Schmailzl, K.-P. Hopfner, Structural Basis for Dodecameric Assembly States and Conformational Plasticity of the Full-Length AAA+ ATPases Rvb1·Rvb2. *Structure* **23**, 483–495 (2015).

197. O. Willhoft, *et al.*, Structure and dynamics of the yeast SWR1-nucleosome complex. *Science* **362**, eaat7716 (2018).

198. S. Eustermann, *et al.*, Structural basis for ATP-dependent chromatin remodelling by the INO80 complex. *Nature* **556**, 386–390 (2018).

199. C. Y. Zhou, *et al.*, Regulation of Rvb1/Rvb2 by a Domain within the INO80 Chromatin Remodeling Complex Implicates the Yeast Rvbs as Protein Assembly Chaperones. *Cell Reports* **19**, 2033–2044 (2017).

200. O. Willhoft, D. B. Wigley, INO80 and SWR1 complexes: the non-identical twins of chromatin remodelling. *Curr Opin Struc Biol* **61**, 50–58 (2020).

201. F. Martino, *et al.*, RPAP3 provides a flexible scaffold for coupling HSP90 to the human R2TP co-chaperone complex. *Nat Commun* **9**, 1501 (2018).

202. H. Muñoz-Hernández, *et al.*, Prefoldins: the new chaperones. *Adv Exp Med Biol* **1106**, 73–83 (2018).

203. J. Lynham, W. A. Houry, Prefoldins: the new chaperones. *Adv Exp Med Biol* **1106**, 37–72 (2018).

204. J. Cuéllar, *et al.*, Structural and functional analysis of the role of the chaperonin CCT in mTOR complex assembly. *Nat Commun* **10**, 2865 (2019).

205. S. G. Kim, *et al.*, Metabolic Stress Controls mTORC1 Lysosomal Localization and Dimerization by Regulating the TTT-RUVBL1/2 Complex. *Mol Cell* **49**, 172–185 (2013).

206. H. Muñoz-Hernández, *et al.*, Structural mechanism for regulation of the AAA-ATPases RUVBL1-RUVBL2 in the R2TP co-chaperone revealed by cryo-EM. *Science advances* **5**, eaaw1616 (2019).

207. T. V. Seraphim, *et al.*, Assembly principles of the human R2TP chaperone complex reveal the presence of R2T and R2P complexes. *Structure* (2021) https:/doi.org/10.1016/j.str.2021.08.002.

208. A. López-Perrote, *et al.*, Regulation of RUVBL1-RUVBL2 AAA-ATPases by the nonsense-mediated mRNA decay factor DHX34, as evidenced by Cryo-EM. *Elife* **9**, e63042 (2020).

209. M. Taipale, *et al.*, Quantitative Analysis of Hsp90-Client Interactions Reveals Principles of Substrate Recognition. *Cell* **150**, 987–1001 (2012).

210. F. Weissmann, *et al.*, biGBac enables rapid gene assembly for the expression of large multisubunit protein complexes. *P Natl Acad Sci Usa* **113**, E2564-9 (2016).

211. F. Weissmann, J.-M. Peters, Expressing Multi-subunit Complexes Using biGBac. *Methods in molecular biology (Clifton, N.J.)* **1764**, 329–343 (2018).

212. N. J. Watkins, *et al.*, Assembly and Maturation of the U3 snoRNP in the Nucleoplasm in a Large Dynamic Multiprotein Complex. *Mol Cell* **16**, 789–798 (2004).

213. J. Scholz, S. Suppmann, A new single-step protocol for rapid baculovirus-driven protein production in insect cells. *Bmc Biotechnol* **17**, 83 (2017).

214. A. López-Perrote, H. Muñoz-Hernández, D. Gil, O. Llorca, Conformational transitions regulate the exposure of a DNA-binding domain in the RuvBL1-RuvBL2 complex. *Nucleic Acids Res* **40**, 11086–99 (2012).

215. C. Iacobucci, *et al.*, A cross-linking/mass spectrometry workflow based on MS-cleavable cross-linkers and the MeroX software for studying protein structures and protein-protein interactions. *Nat Protoc* **13**, 2864–2889 (2018).

216. M. L. Mendes, *et al.*, An integrated workflow for crosslinking mass spectrometry. *Mol Syst Biol* **15**, e8994 (2019).

217. C. W. Combe, L. Fischer, J. Rappsilber, xiNET: Cross-link Network Maps With Residue Resolution*. *Mol Cell Proteomics* **14**, 1137–1147 (2015).

218. R. B. Vallee, [10] Reversible assembly purification of microtubules without assemly-promoting agents and further purification of tubulijn, microtubule-associated proteins, and MAP fragments. *Methods Enzymol* **134**, 89–104 (1986).

219. J. Zivanov, *et al.*, New tools for automated high-resolution cryo-EM structure determination in RELION-3. *Elife* **7**, e42166 (2018).

220. A. Punjani, J. L. Rubinstein, D. J. Fleet, M. A. Brubaker, cryoSPARC: algorithms for rapid unsupervised cryo-EM structure determination. *Nat Methods* **14**, 290–296 (2017).

221. E. F. Pettersen, *et al.*, UCSF Chimera—A visualization system for exploratory research and analysis. *J Comput Chem* **25**, 1605–1612 (2004).

222. S. Q. Zheng, *et al.*, MotionCor2: anisotropic correction of beam-induced motion for improved cryo-electron microscopy. *Nat Methods* **14**, 331–332 (2017).

223. K. Zhang, Gctf: Real-time CTF determination and correction. *J Struct Biol* **193**, 1–12 (2016).

224. J. Yang, Y. Zhang, I-TASSER server: new development for protein structure and function predictions. *Nucleic Acids Res* **43**, W174–W181 (2015).

225. P. Emsley, B. Lohkamp, W. G. Scott, K. Cowtan, Features and development of Coot. *Acta Crystallogr Sect D Biological Crystallogr* **66**, 486–501 (2010).

226. P. D. Adams, *et al.*, PHENIX: a comprehensive Python-based system for macromolecular structure solution. *Acta Crystallogr Sect D Biological Crystallogr* **66**, 213–221 (2010).

227. G. N. Murshudov, *et al.*, REFMAC5 for the refinement of macromolecular crystal structures. *Acta Crystallogr Sect D Biological Crystallogr* **67**, 355–367 (2011).

228. A. Drozdetskiy, C. Cole, J. Procter, G. J. Barton, JPred4: a protein secondary structure prediction server. *Nucleic Acids Res* **43**, W389–W394 (2015).

229. M. Wieczorek, T.-L. Huang, L. Urnavicius, K.-C. Hsia, T. M. Kapoor, MZT Proteins Form Multi-Faceted Structural Modules in the γ-Tubulin Ring Complex. *Cell Reports* **31**, 107791 (2020).

230. T.-L. Huang, H.-J. Wang, Y.-C. Chang, S.-W. Wang, K.-C. Hsia, Promiscuous Binding of Microprotein Mozart1 to γ-Tubulin Complex Mediates Specific Subcellular Targeting to Control Microtubule Array Formation. *Cell Reports* **31**, 107836 (2020).

231. C. Gentili, *et al.*, Chromosome Missegregation Associated with RUVBL1 Deficiency. *Plos One* **10**, e0133576 (2015).
232. R. Bahtz, *et al.*, GCP6 is a substrate of Plk4 and required for centriole duplication. *Journal of cell science* **125**, 486–496 (2012).

233. J. M. Kollman, *et al.*, The Structure of the γ-Tubulin Small Complex: Implications of Its Architecture and Flexibility for Microtubule Nucleation. *Molecular biology of the cell* **19**, 207–215 (2008).

234. M. Q. Müller, F. Dreiocker, C. H. Ihling, M. Schäfer, A. Sinz, Cleavable cross-linker for protein structure analysis: reliable identification of cross-linking products by tandem MS. *Anal Chem* **82**, 6958–68 (2010).

235. P. Liu, *et al.*, Insights into the assembly and activation of the microtubule nucleator γ-TuRC. *Nature*, 1–8 (2019).

236. M. Wieczorek, *et al.*, Asymmetric Molecular Architecture of the Human γ-Tubulin Ring Complex. *Cell* (2019) https:/doi.org/10.1016/j.cell.2019.12.007.

237. T. Consolati, *et al.*, Microtubule Nucleation Properties of Single Human γTuRCs Explained by Their Cryo-EM Structure. *Dev Cell* (2020) https:/doi.org/10.1016/j.devcel.2020.04.019.

238. M. Wieczorek, *et al.*, Biochemical reconstitutions reveal principles of human γ-TuRC assembly and function. *J Cell Biol* **220** (2021).

239. M. Würtz, *et al.*, Reconstitution of the recombinant human γ-tubulin ring complex. *Open Biol* **11**, 200325 (2021).

240. C. Maurizy, *et al.*, The RPAP3-Cterminal domain identifies R2TP-like quaternary chaperones. *Nat Commun* **9**, 2093 (2018).

241. C. F. Rodríguez, O. Llorca, RPAP3 C-Terminal Domain: A Conserved Domain for the Assembly of R2TP Co-Chaperone Complexes. *Cells* **9**, 1139 (2020).

242. T. D. Pollard, Actin and Actin-Binding Proteins. *Csh Perspect Biol* **8**, a018226 (2016).

243. B. Coulombe, *et al.*, The PAQosome, a novel molecular chaperoning machine for assembly of human protein complexes and networks. *Faseb J* **34**, 1–1 (2020).

244. J.-P. Couso, P. Patraquim, Classification and function of small open reading frames. *Nat Rev Mol Cell Bio* **18**, 575–589 (2017).

245. J. Chen, *et al.*, Pervasive functional translation of noncanonical human open reading frames. *Science* **367**, 1140–1146 (2020).

246. I. Gasic, S. A. Boswell, T. J. Mitchison, Tubulin mRNA stability is sensitive to change in microtubule dynamics caused by multiple physiological and toxic cues. *Plos Biol* **17**, e3000225 (2019).

247. Z. Lin, *et al.*, TTC5 mediates autoregulation of tubulin via mRNA degradation. *Sci New York N Y* **367**, 100–104 (2019).

248. X. Fant, N. Gnadt, L. Haren, A. Merdes, Stability of the small gamma-tubulin complex requires HCA66, a protein of the centrosome and the nucleolus. *Journal of cell science* **122**, 1134–1144 (2009).

249. C. L. Ladner, J. Yang, R. J. Turner, R. A. Edwards, Visible fluorescent detection of proteins in polyacrylamide gels without staining. *Anal Biochem* **326**, 13–20 (2004).

250. W. Holzmüller, U. Kulozik, Protein quantification by means of a stain-free SDS-PAGE technology without the need for analytical standards: Verification and validation of the method. *J Food Compos Anal* **48**, 128–134 (2016).

251. M. A. Cianfrocco, E. H. Kellogg, What Could Go Wrong? A Practical Guide to Single-Particle Cryo-EM: From Biochemistry to Atomic Models. *J Chem Inf Model* (2020) https:/doi.org/10.1021/acs.jcim.9b01178.

252. W. Kabsch, H. G. Mannherz, D. Suck, E. F. Pai, K. C. Holmes, Atomic structure of the actin: DNase I complex. *Nature* **347**, 37–44 (1990).

253. B. J. LaFrance, *et al.*, Structural transitions in the GTP cap visualized by cryo-EM of catalytically inactive microtubules. *Biorxiv*, 2021.08.13.456308 (2021).

254. A. A. Hyman, D. Chrétien, I. Arnal, R. H. Wade, Structural changes accompanying GTP hydrolysis in microtubules: information from a slowly hydrolyzable analogue guanylyl-(alpha,beta)-methylene-diphosphonate. *J Cell Biology* **128**, 117–125 (1995).

255. A. F. Brilot, *et al.*, CM1-driven assembly and activation of yeast γ-tubulin small complex underlies microtubule nucleation. *Elife* **10**, e65168 (2021).

256. J. A. Zahm, M. G. Stewart, J. S. Carrier, S. C. Harrison, M. P. Miller, Structural basis of Stu2 recruitment to yeast kinetochores. *Elife* **10**, e65389 (2021).

257. G. E. Debs, M. Cha, X. Liu, A. R. Huehn, C. V. Sindelar, Dynamic and asymmetric fluctuations in the microtubule wall captured by high-resolution cryoelectron microscopy. *Proc National Acad Sci* **117**, 16976–16984 (2020).

258. C. Guyomar, *et al.*, Structural heterogeneity of the microtubule lattice. *bioRxiv* (2021) https:/doi.org/10.1101/2021.07.14.452321.

259. H. E. Foster, C. V. Santos, A. P. Carter, A cryo-ET study of microtubules in axons. *Biorxiv*, 2021.03.29.437471 (2021).

260. S. Gungor, *et al.*, Autosomal recessive variants in TUBGCP2 alter the γ-tubulin ring complex leading to neurodevelopmental disease. *Iscience*, 101948 (2020).

261. T. Mitani, *et al.*, Bi-allelic Pathogenic Variants in TUBGCP2 Cause Microcephaly and Lissencephaly Spectrum Disorders. *Am J Hum Genet* (2019) https:/doi.org/10.1016/j.ajhg.2019.09.017.

262. X. Xu, D. Shang, H. Cheng, D. J. Klionsky, R. Zhou, Gene essentiality of Tubgcp4: dosage effect and autophagy regulation in retinal photoreceptors. *Autophagy* **15**, 1834–1837 (2019).

263. S. Kolbjer, D. A. Martin, M. Pettersson, M. Dahlin, B.-M. Anderlid, Lissencephaly in an epilepsy cohort: Molecular, radiological and clinical aspects. *Eur J Paediatr Neuro* **30**, 71–81 (2021).

Parts of this work have been published in the following publication:

F. Zimmermann, M. Serna, A. Ezquerra, R. Fernandez-Leiro, O. Llorca, J. Luders, Assembly of the asymmetric human γ-tubulin ring complex by RUVBL1-RUVBL2 AAA ATPase. *Sci. Adv.* 6, eabe0894 (2020).